

ABSTRACT

AHMED, SHOAIB. Flow and Heat Transfer in an Industrial Swirl Stabilized Can Combustor - Development and Testing of Cooling Concepts (Under the direction of Dr. Srinath V. Ekkad).

While the gas turbine research community is pursuing higher efficiency by increasing the higher combustor and turbine inlet temperatures, a simultaneous effort to reduce the NO_x emission level also needs to be considered. In recent times, there has been a significant push towards developing lean premixed combustion technologies to address this objective. The most promising approach to reduce pollutant emission is through swirl stabilized lean premixed combustion. A considerable amount of air is routed into the combustion chamber through the swirler to reduce NO_x emissions in lean combustion applications, reducing the amount of air available for cooling the combustor liner. Simultaneously, there is a constant requirement to raise the combustor and turbine sections' temperature to increase overall turbine efficiency. As a result, combustor liners in modern gas turbines are subjected to very high temperatures and high thermal gradients that severely impact their structural integrity. To this end, the development of optimized combustor liner cooling technologies is crucial to increasing modern combustor components' life cycles.

A principal method used to manage the high heat loads on the combustor liners is film cooling. Film cooling refers to the injection of coolant onto a surface through holes to form an insulating layer between hot freestream air and the surface. Discrete film cooling often leads to a free film cooling layer over the liner and excessive coolant flow, which causes the coolant jet to overshoot and weakens its effectiveness. Effusion cooling, also known as full coverage film cooling, overcomes these issues by having successive rows of film cooling holes interacting and forming a continuous protective film along the wall. The main objective of this study is to

investigate flow and heat transfer in an industrial swirl stabilized can combustor with a focus on testing and development of cooling concepts under reacting and non-reacting conditions. This study can be broadly divided into three parts. In the first part, a novel three-dimensional heat conduction model was developed to account for lateral heat conduction effects in infrared thermography and liquid crystal thermography experiments. The second part deals with the comparison of the flow field, and heat transfer on combustor liner wall generated by a low emission, low-NOX lean premixed, industrial fuel swirl nozzle. The third part deals with the experimental investigation of effusion-cooled liners under-reacting and non - reacting conditions. The data obtained aims to aid designers of gas turbine components and develop and validate numerical codes for the accurate prediction of heat transfer performance of such components.

© Copyright 2021 by Shoaib Ahmed

All Rights Reserved

Flow and Heat transfer in an Industrial Swirl Stabilized Can Combustor – Development and
Testing of Cooling Concepts

by
Shoaib Ahmed

A dissertation submitted to the Graduate Faculty of
North Carolina State University
in partial fulfillment of the
requirements for the degree of
Doctor of Philosophy

Mechanical Engineering

Raleigh, North Carolina
2021

APPROVED BY:

Dr. Srinath Ekkad
Committee Chair

Dr. Tarek Echehki

Dr. Alexei Saveliev

Dr. Pramod Subbareddy

DEDICATION*To my Family*

BIOGRAPHY

Shoaib grew up in the city of Abu Dhabi, UAE. He moved to India to complete his B.Tech in Mechanical Engineering from the College of Engineering, Trivandrum. After his undergrad, Shoaib moved to the United States of America to pursue a Ph.D. in the Mechanical and Aerospace Engineering Department at NCSU to enhance his experience in heat transfer and fluid dynamics. He worked under Dr. Srinath Ekkad from 2017 to 2021 on thermal management and heat transfer problems for gas turbine applications. Over the four years at NC State, he has gained a lot of experience solving fundamental heat transfer problems, carrying out experimental heat transfer investigations, and conducting numerical simulations. The work completed during this time has been presented in this Ph.D. dissertation document.

ACKNOWLEDGMENTS

First and foremost, I would like to thank my advisor, Dr. Srinath Ekkad, for believing in me and allowing me to do a Ph.D. under his guidance. Thank you for all your guidance and support and for nurturing me throughout my North Carolina State University journey.

To all my colleagues and friends from Thermal Energy Research and Management Lab (ThERML), this dissertation would not have been possible without the input and help from all of you.

And finally, I would like to thank my committee members, Dr. Tarek Echehki, Dr. Alexie Saveliev, Dr. Pramod Subbareddy, and Dr. Jason Patrick, for agreeing to serve on the committee and taking the time to review my work. Your guidance and efforts are greatly appreciated.

TABLE OF CONTENTS

LIST OF TABLES	x
LIST OF FIGURES	xi
INTRODUCTION.....	1
Chapter 1: Three-Dimensional Transient Heat Conduction Equation Solution For Accurate Determination Of Heat Transfer Coefficient.....	5
1.1. ABSTRACT.....	5
1.2. INTRODUCTION.....	6
1.3. Experimental Setup	9
1.3.1. Experimental Setup for IRT Experiment	10
1.3.2. Experimental Setup for LCT Experiment	11
1.4. DESCRIPTION OF TEST CONFIGURATIONS	12
1.4.1. Test Configurations for IRT Experiment	12
1.4.2. Test Configurations for LCT Experiment	12
1.5. ONE-DIMENSIONAL TRANSIENT HEAT CONDUCTION EQUATION SOLUTION METHODOLOGY.....	13
1.5.1. One-Dimensional semi-infinite heat conduction model.....	13
1.5.2. Heat transfer coefficient determination for IRT experiment.....	15
1.5.3. Heat transfer coefficient determination from LCT experiment	16
1.6. THREE-DIMENSIONAL HEAT CONDUCTION MODEL.....	17

1.6.1. Three-dimensional heat conduction model	20
1.6.2. Boundary conditions	23
1.6.3. Heat transfer coefficient determination methodology: 3D conduction modeling...	25
1.7. RESULTS AND DISCUSSION	26
1.7.1. Demonstration study	26
1.7.2. Heat transfer coefficient calculations through different models (1D and 3D conduction) for IRT experiment.....	30
1.7.3. Heat transfer coefficient calculations through different models (1D and 3D conduction) for LCT experiment	33
1.8. CONCLUSIONS	38
NOMENCLATURE.....	39
REFERENCES.....	41
 Chapter 2: Heat Transfer In An Industrial Low Nox Swirl Stabilized Can Combustor:	
Assessment Of Hybrid Rans-Les Methods	47
2.1. ABSTRACT	47
2.2. INTRODUCTION.....	48
2.3. DESCRIPTION OF EXPERIMENTAL SETUP	52
2.3.1. Experimental Setup for PIV Experiments	54
2.3.2. Experimental Setup for Heat Transfer Experiments	55
2.4. NUMERICAL METHODOLOGY AND SETUP	56

2.4.1. Numerical Setup.....	56
2.4.2. Methodology	57
2.4.3. Inlet Flow Profiles	59
2.4.4. Boundary Conditions.....	59
2.4.5. Turbulence Modelling	59
2.4.6. Grid Generation.....	61
2.5. RESULTS AND DISCUSSION	64
2.5.1. Time averaged results.....	64
2.6. CONCLUSIONS	69
NOMENCLATURE.....	70
REFERENCES.....	71

Chapter 3: Overall Cooling Effectiveness of Effusion Cooled Can Combustor Liner

under Reacting and Non-Reacting Conditions	76
3.1. ABSTRACT	76
3.2. INTRODUCTION	77
3.3. EXPERIMENTAL SETUP	81
3.3.1. Effusion Configurations	85
3.4. EXPERIMENTAL PROCEDURE AND DATA REDUCTION.....	86
3.4.1. Infrared (IR) Thermography.....	86
3.4.2. Data reduction	89

3.4.3. Operating conditions	90
3.5.UNCERTAINTY	93
3.6.RESULTS AND DISCUSSION	93
3.6.1. Flow field in the combustor	93
3.6.2. Experimental Overall Cooling Effectiveness – Non-Reacting Flow	96
3.6.3. Overall Cooling Effectiveness - Reacting flow.....	100
3.7.CONCLUSIONS.....	105
NOMENCLATURE.....	106
REFERENCES.....	108
 Chapter 4: Effect of Spanwise Hole to Hole Spacing on Overall Cooling Effectiveness of Effusion Cooled Combustor Liners for a Swirl Stabilized Can Combustor	 113
4.1. ABSTRACT	113
4.2. INTRODUCTION.....	114
4.3. EXPERIMENTAL SETUP	117
4.3.1. Effusion Configurations	120
4.4. EXPERIMENTAL METHODOLOGY	122
4.4.1. Infrared (IR) Thermography.....	122
4.4.2. Data reduction	125
4.4.3. Operating conditions	125
4.5. UNCERTAINTY.....	127

4.6. RESULTS AND DISCUSSION	127
4.6.1. Flow within the combustor	127
4.6.2. Overall Cooling Effectiveness	131
4.7. CONCLUSIONS.....	135
NOMENCLATURE.....	137
REFERENCES.....	139
FUTURE RECOMMENDATION	143

LIST OF TABLES

Table 1.1: Parameters used in initial study	27
Table 1.2: Grid Independence study	27
Table 1.3: Grid Independence study	30
Table 1.4: Grid Independence study	33
Table 3.1: Operating conditions of combustor rig for non - reacting conditions	92
Table 3.2: Operating conditions of combustor rig for reacting conditions	92

LIST OF FIGURES

Figure 1.1 Schematic of (a) IRT experimental Setup for single jet experiment (b) LCT setup	9
Figure 1.2 Schematic of jet plate for IRT experiment	12
Figure 1.3 Schematic of jet plate and region of interest on the target plate for LCT experiment.....	13
Figure 1.4 Variation of hue with wall temperature	16
Figure 1.5 Flowchart of heat transfer calculation methodology in 3D conduction modelling	24
Figure 1.6 Comparison of final temperature for grid independence study	28
Figure 1.7 Comparison of radially varying Nusselt Number.....	29
Figure 1.8 Grid Independence study	31
Figure 1.9 Detailed Nusselt Number Comparison for (a) 1D Model (b) 3D Model.....	31
Figure 1.10 Comparison of radial variation of Nusselt Number with Hollworth and Gero [1.32].....	32
Figure 1.11 Grid Independence study	33
Figure 1.12 Detailed Nusselt Number distribution	35
Figure 1.13 Spanwise-averaged Nusselt Number	36
Figure 1.14 Row-wise Averaged Nusselt Number	37
Figure 1.15 Comparison of Area Averaged Nusselt number for 1D and 3D Model with Florschuetz et al. [1.40]	38
Figure 2.1 Swirl flow in a can combustor	49
Figure 2.2 Experimental facility	52
Figure 2.3 Schematic of the test section	53
Figure 2.4 Schematic of the swirler used	53

Figure 2.5 PIV Planes	54
Figure 2.6 Infrared Thermography (IR) Setup	55
Figure 2.7 Domain Details	57
Figure 2.8 Normalized velocity profiles and turbulent kinetic energy	58
Figure 2.9 Computational mesh used in study	62
Figure 2.10 Velocity Contours on Plane A superimposed with velocity streamlines.....	63
Figure 2.11 Radially averaged non-dimensionalized (a) Axial Velocity (b) Radial Velocity (c) Tangential Velocity	65
Figure 2.12 Time dependent velocity contour on Plane A	67
Figure 2.13 Time dependent velocity contour on Plane A	67
Figure 2.14 Time dependent velocity contour on Plane A	68
Figure 2.15 Heat Transfer Coefficient	68
Figure 3.1 Combustor rig test setup	82
Figure 3.2 Schematic of the Test Section	83
Figure 3.3 Schematic of the fuel nozzle.....	83
Figure 3.4 (a) Staggered and (b) Inline Configurations	85
Figure 3.5 Geometric details of the test section.....	85
Figure 3.6 IR Methodology.....	87
Figure 3.7 Schematic of ROI with the location of calibration thermocouples	88
Figure 3.8 Calibration curve for the reacting case	89
Figure 3.9 Flow features within a can combustor	94
Figure 3.10 Mean velocity of flow at (a) Non-reacting conditions [3.27] and (b) reacting conditions at 0.65 equivalence ratio without cooling holes [3.29]	95

Figure 3.11 Overall Cooling Effectiveness Contour at non-reacting conditions for (a) Inline Configuration (b) Staggered Configuration.....	97
Figure 3.12 Spanwise averaged cooling effectiveness contour at non-reacting conditions for (a) Inline configuration (b) Staggered Configuration.....	98
Figure 3.13 Area averaged cooling effectiveness under non-reacting conditions	99
Figure 3.14 Overall Cooling Effectiveness Contour at reacting conditions for (a) Staggered Configuration (b) Inline Configuration	102
Figure 3.15 Spanwise averaged cooling effectiveness at reacting conditions for (a) Inline configuration (b) Staggered configuration	103
Figure 3.16 Area averaged cooling effectiveness under reacting conditions	103
Figure 4.1 Combustor rig test setup	118
Figure 4.2 Schematic of the test section	118
Figure 4.3 Schematic of the fuel nozzle.....	119
Figure 4.4 Geometric details of test section.....	120
Figure 4.5 Schematic of the liners investigated in this study (a) $r/d = 10$ (b) $r/d = 8$ (c) $r/d = 10$	122
Figure 4.6 IR Methodology.....	123
Figure 4.7 Calibration curve	124
Figure 4.8 Flow features within a can combustor	128
Figure 4.9 Mean velocity of reacting flow at 0.65 equivalence ratio from Park et al. [4.23]....	129
Figure 4.10 Overall Cooling Effectiveness Contour at different nominal coolant flow rates for a spanwise hole-to-hole spacing (r/d) of 10	129

Figure 4.11 Overall Cooling Effectiveness Contour at different nominal coolant flow rates

for a spanwise hole-to-hole spacing (r/d) of 8 130

Figure 4.12 Overall Cooling Effectiveness Contour at different nominal coolant flow rates

for a spanwise hole-to-hole spacing (r/d) of 6 130

Figure 4.13 Spanwise averaged cooling effectiveness for (a) $r/d=10$ (b) $r/d=8$ (c) $r/d=10$ 131

Figure 4.14 Effect of nominal cooling flowrate ratio on area averaged overall

cooling effectiveness 133

Figure 4.15 Effect of pressure drop across the liner on area averaged overall cooling

effectiveness 134

INTRODUCTION

The gas turbine research community continuously pursues higher cycle efficiency designs by increasing the combustor firing temperatures and developing thermally resistant turbine vane and blade materials. Simultaneously, an effort to reduce the emission levels of high temperature-driven thermal NOX also needs to be addressed. Lean premixed combustion has been found to be an optimum solution to address both of these concerns. However, premixed combustion uses a significant amount of air for premixing and limits the amount of air available for liner cooling. Hence, it becomes crucial to develop optimized liner cooling technologies. These studies were explored using laboratory-scale experiments as well as numerical approaches for both non-reacting and reacting flows. These results obtained in this study aims to aid designers of gas turbine components and the development and validation of numerical codes for accurate prediction of heat transfer performance of such elements.

The first chapter of this dissertation deals with the accurate quantification of the local heat transfer coefficient for the design and development of heat exchangers for high heat flux dissipation applications. Liquid crystal and infrared thermography are typically employed to measure precise surface temperatures, where local heat transfer coefficient (HTC) values are calculated by using suitable conduction models. The assumption of one-dimensional heat conduction often leads to significant errors in HTC determination. This chapter presents a procedure for the solution of a three-dimensional transient conduction equation using the alternating direction implicit (ADI) method and an error minimization routine to find accurate heat transfer coefficients at a relatively lower computational cost. Representative cases of a single jet and an array jet impingement under maximum crossflow conditions have been considered here for infrared thermography and liquid crystal thermography, respectively. Results indicate that the

globally averaged HTC obtained using the 3D model was consistently higher than the conventional 1D model by 7-14%, with deviation levels reaching as high as 20% near the stagnation region.

In the second chapter, the unsteady isothermal fluid dynamics and related heat transfer on liner walls generated by a low emission, low-NOX lean premixed, industrial fuel swirl nozzle designed by Solar Turbines Incorporated have been numerically investigated. This study compares the performance of the Reynolds Averaged Navier Stokes (RANS) approach, and Hybrid Reynolds Averaged Navier Stokes – Large Eddy Simulation (RANS-LES) in computing the flow field and heat transfer generated by an industrial swirler within a can combustor. The RANS Model and three different hybrid RANS-LES models, Scale Adaptive Simulations (SAS), Detached Eddy Simulations (DES), and Wall Modeled Large Eddy Simulation models, were compared in this study. The hybrid RANS-LES models provided good agreement with the Particle Image Velocimetry (PIV) experimental measurements regarding the opening angle, impingement location, and internal recirculation zone size compared to the RANS Model. The liner wall heat transfer assessment confirms the Hybrid RANS-LES models' overall accuracy, which showed good agreement with the experimental PIV and heat transfer results. The WMLES model performed the best compared to the other hybrid RANS-LES models and represents a starting point for further investigations that consider the presence of effusion cooling.

In the third chapter, the findings from an experimental study on the characterization of the overall cooling effectiveness of an effusion-cooled liner wall, which was representative of a can combustor under heated flow (non-reacting) and lean-combustion (reacting) conditions, has been presented. The model can-combustor was equipped with an industrial swirler, which subjected the liner walls to engine representative flow and combustion conditions. Two different effusion cooling liners with an inline and staggered effusion holes have been studied. Non-dimensionalized

streamwise hole-to-hole spacing (z/d) and spanwise hole-to-hole spacing (r/d) of 10 were used for both the effusion liners. Infrared Thermography (IRT) was used to measure the liner outer surface temperature, and detailed overall effectiveness values were determined under steady-state conditions. It was observed that overall cooling effectiveness trends were different under reacting and non-reacting conditions. The cooling effectiveness for the non-reacting experiments exhibited a decreasing trend, and no consistent location of minimum cooling effectiveness was observed for the range of blowing ratios investigated in this study. For the reacting cases, the cooling effectiveness first follows a decreasing trend, reaches a distinct minimum, and then increases until the combustor's end. Under non-reacting conditions, the staggered configuration was 9-25% more effective than inline configuration, and under-reacting conditions, the staggered configuration was 4-8% more effective than inline configuration. From this study, it is clear that the coolant-flame interaction for the reacting experiments impacted the liner cooling effectiveness and led to different overall cooling effectiveness distribution on the liner as compared to the non-reacting experiments.

In the final chapter, experimental results are presented for effusion cooling configurations for a realistic swirl-driven can combustor under reacting (flame) conditions. Experimental results are presented for three different effusion cooling liners with spanwise spacings of $r/d = 6, 8$, and 10 , and a streamwise spacing of $z/d = 10$ was tested for four coolant-to-main airflow ratios. The experiments were carried out at a constant main flow Reynolds number (based on combustor diameter) of $12,500$ at a total equivalence ratio of 0.65 . Infrared Thermography (IRT) was used to measure the liner outer surface temperature, and detailed overall effectiveness values were determined under steady-state conditions. The results indicate that decreasing the spanwise hole-to-hole spacing (r/d) from 10 to 8 increased the overall cooling effectiveness by $2-5\%$. It was found

that reducing the spanwise hole-to-hole spacing further to $r/d = 6$ does not affect the cooling effectiveness, implying an optimum spanwise hole-to-hole spacing. Also, the minimum liner cooling effectiveness on the liner wall was found to be downstream of the impingement location, which is not observed in existing literature for experiments done under non-reacting conditions

CHAPTER 1

THREE-DIMENSIONAL TRANSIENT HEAT CONDUCTION EQUATION SOLUTION FOR ACCURATE DETERMINATION OF HEAT TRANSFER COEFFICIENT

1.1. ABSTRACT

Accurate quantification of local heat transfer coefficient is imperative for design and development of heat exchangers for high heat flux dissipation applications. Liquid crystal and infrared thermography are typically employed to measure detailed surface temperatures, where local heat transfer coefficient (HTC) values are calculated by employing suitable conduction models, e.g. one-dimensional semi-infinite conduction model, on test surface with low thermal conductivity and low thermal diffusivity. The assumption of one-dimensional heat conduction, often times lead to significant errors in HTC determination and this error depends on the true HTC, nature of wall temperature evolution with time and the local HTC gradient. Prior studies have identified this problem and quantified the associated errors in HTC determination for some representative cooling concepts, by accounting for lateral heat diffusion. In this paper, we have presented a procedure for solution of three-dimensional transient conduction equation using alternating direction implicit (ADI) method and an error minimization routine to find accurate heat transfer coefficients at relatively lower computational cost. Representative cases of a single jet and an array jet impingement under maximum crossflow condition has been considered here, for infrared thermography and liquid crystal thermography respectively. Results indicate that the globally averaged HTC obtained using the 3D model was consistently higher than the conventional 1D model by 7-14%, with deviation levels reaching as high as 20% near the stagnation region. Proposed methodology was computationally efficient and is recommended for studies aimed towards local HTC determination.

1.2. INTRODUCTION

Forced convection is typically used in cooling applications which require high heat dissipation rates, e.g. in gas turbine blade leading edge etc. Typically, a single phase fluid (usually air) is routed through cooling passages which are equipped with heat transfer enhancement agents, e.g. turbulence promoters, swirl cooling, combination cooling techniques jet impingement etc. [1.1-1.8]. To quantify the thermal hydraulic performance (THP) of these cooling concepts, the enhancement in Nusselt number with reference to a baseline cooling geometry (typically smooth duct) is used in conjunction with net increment in pumping power. The aim of the cooling designer is to develop concepts, which have high gain in heat transfer at a relatively lower penalty on pumping power requirement. Hence, accurate quantification of local heat transfer coefficients is important to rank the cooling designs based on their respective THPs.

Local heat transfer coefficients are typically determined using advanced thermal diagnostic techniques such as liquid crystal thermography (LCT) and Infrared thermography (IRT), which provide detailed surface temperature measurement of the surface, which is subjected to forced convection type boundary condition. Techniques involving LCT depend on relationship between color content of a pixel to a known wall temperature. Initially the LCT was used for local wall temperature measurements under steady-state constant surface heat flux type boundary condition for HTC determination [1.9]. Another method of heat transfer coefficient determination using LCT was to use transient one-dimensional semi-infinite conduction model by employing a solid with low thermal conductivity and low thermal diffusivity such that the heat diffusion in two other directions can be ignored compared to the heat diffusion into the thickness of the solid. This is a widely used technique and has been in circulation since 1980s [1.10, 1.11]. LCT based measurement techniques gained more prominence in early 1990 when researchers demonstrated

that the Hue-based calibration technique provides robust local temperature values, which were not very sensitive to external factors, such as lighting, camera viewing angle etc. that effect the color to temperature mapping [1.12]. In later years, Ekkad and Han published a series of papers on employment of LCT in both two and three-temperature problems [1.13, 1.14]. A two-temperature problem essentially involved local wall and bulk fluid temperature measurement for flows in confined ducts, where the wall temperature was measured using liquid crystals and fluid temperature was measured by thermocouples. Similarly, three-temperature problem simulating film-cooling problems in gas turbine blades was also studied for local heat transfer coefficient and adiabatic film cooling effectiveness determination [1.15]. LCT proved to be effective in the determination of local heat transfer coefficient and film cooling effectiveness.

Similarly, infrared thermography is also a popular technique now, and is used frequently to measure detailed surface temperature. Carlomagno and Cardone [1.16] carried out a detailed review on the application of infrared thermography for heat transfer measurements. Ekkad et al. [1.17] proposed a transient infrared method for simultaneously measuring the heat transfer coefficient and film cooling effectiveness. The transient Infrared thermography technique has been used in many other three-temperature problem studies [1.18,1.19].

In all above studies, a 1D semi-infinite conduction model was used, and this underlying assumption that heat essentially gets diffused only into the thickness of the solid, on some occasions results in significant deviation from true heat transfer coefficient (which should include the contribution of lateral conduction). There have been relatively fewer studies on this subject matter and some of them are listed below. Ling et al. [1.20] quantified the difference in heat transfer coefficient and film cooling effectiveness calculated using the 1D and 3D conduction model for a single-hole film cooling configuration. Lin and Wang [1.21] developed an inverse 3D

conduction scheme to calculate the heat transfer coefficient from a transient liquid crystal experiment. The authors reported deviation of 15-20% between the 1D and the 3D conduction models. Riley et al. [1.22] conducted liquid crystal experiments to calculate the heat transfer coefficient on engine representative geometries using a 3D conduction model. The study effectively concluded that the 1D based methods were unable to provide accurate spatial measurements over geometries with high thermal stresses. Nirmalan et al. [1.23] also developed a method for quantification of heat transfer coefficient using an infrared thermography technique, where HTC calculated from 3D model was reported to be 10-30% higher than that calculated by the 1D model. Brack et al. [1.24] also developed a mathematical approach to consider the lateral conduction effects in the evaluation process of transient heat transfer measurements using LCT. Above studies have identified the issues associated with 1D conduction model and presented the deviation of heat transfer coefficient calculated by 3D for representative test configurations, also highlighting that modeling 3D conduction is computationally expensive.

In the present study, the effect of 3D conduction on the calculation of heat transfer coefficient for a popular cooling concept known as jet impingement [1.25, 1.26] is considered, to showcase the contribution of laterally diffused heat on calculated heat transfer coefficient values. This paper presents a methodology for HTC calculation by implicit solution of three-dimensional heat diffusion equation using Alternating direction implicit (ADI) method. Two representative cases have been presented: (a) single jet impingement onto quartz material where temperature was recorded by an infrared camera, (b) array jet impingement onto ABS material where temperature was measured using liquid crystal thermography. These cases have been chosen to demonstrate the applicability of the proposed methodology for the two most common advanced thermal diagnostic techniques used for local surface temperature measurement. Further, two different solid

materials have been used and the HTC calculated by solving heat diffusion equation in three dimensions is presented and compared with established correlations.

1.3. EXPERIMENTAL SETUP

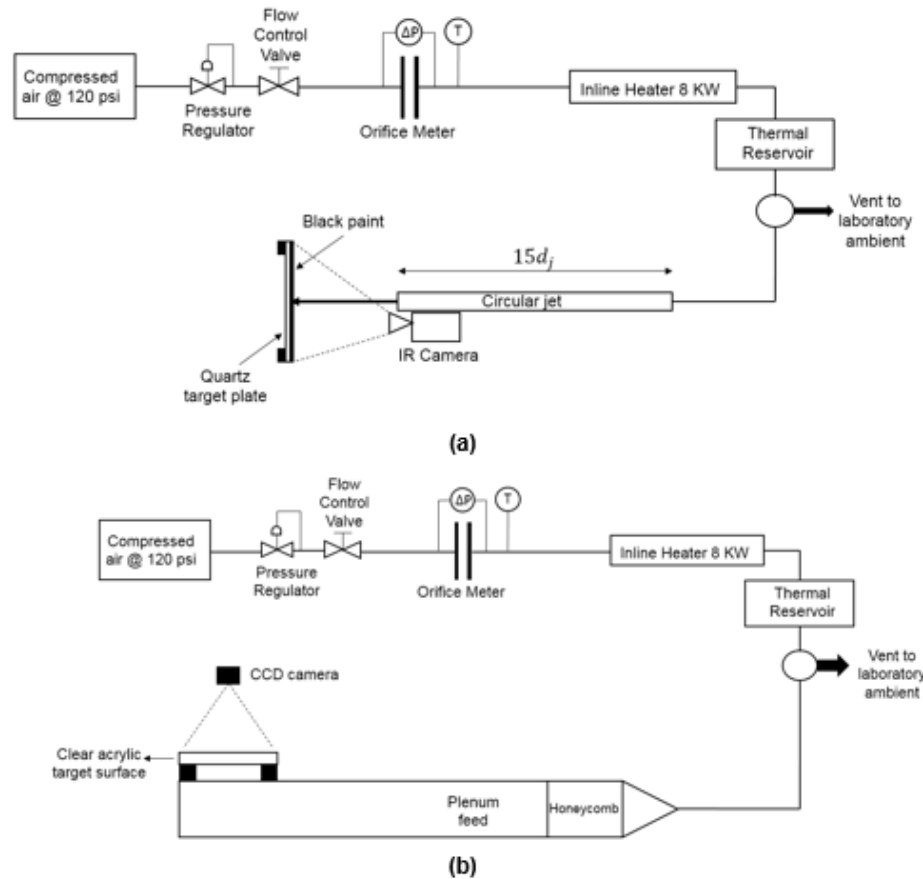


Figure 1.1 Schematic of (a) IRT experimental Setup for single jet experiment (b) LCT setup

1.3.1. Experimental Setup for IRT Experiment

Schematic of the IRT experimental setup is shown in Fig. 1.1a. An active line of compressed air was used to continuously feed a buffer tank, which was maintained at a uniform pressure, to ensure constant supply pressure during the transient experiment. Downstream of the buffer tank, a pressure regulator was installed to adjust the pressure required to pump certain mass flow rate through the test section. Further, a ball valve was installed to fine tune the airflow rate. The air flow rate was metered using an orifice meter (ORIPAC 5300) installed approximately 35 times the pipe diameter downstream of the valve. Sufficiently long entry length was provided upstream of the flow metering section to ensure hydrodynamically developed flow entrance. At the orifice meter, the differential pressure (Dwyer 475-2 FM), flow inlet pressure (Dwyer DPGA-04) and the temperature (via. a fast response thin thermocouple) of the air was measured. Above measurements were used in conjunction for mass flow rate determination through an in-house computer program. For transient heat transfer experiments, a heated reservoir was created prior to the start of the experiment. To this end, an 8 KW inline heater was installed and was used to heat up the reservoir to a suitable temperature prior to the actual heat transfer experiment. The heated air exiting the thermal reservoir was continuously vented into the laboratory ambient, until the desired reservoir temperature was reached. The transient experiment was initiated by switching a three-way valve, which opened the main air-line air towards the heat transfer test section.

The IR experiments were carried out for single jet impingement. The jet was made out of a long straight duct ($15d_j$) to allow proper flow development. The target plate was painted black with Rust Oleum® black paint to ensure high emissivity of the surface where temperature measurements were intended. FLIR SC600 infrared (IR) camera was used to record the temperature of the target plate. The camera was placed such that it nearly aligned with the jet and

hence was nearly orthogonal to the target surface where temperature was to be recorded. Prior studies have indicated the sensitivity of IR camera sensor orientation with respect to the target surface and recommended that the two should be aligned nearly orthogonal, to avoid errors in temperature measurements [1.28]. The temperature output by IR was also calibrated with thermocouple pasted onto the target surface to characterize the emissivity of the black surface.

1.3.2. Experimental Setup for LCT Experiment

Schematic of the LCT experimental setup is shown in Fig. 1b. The experimental setup for the LCT experiment was the same as IRT experiment up to the thermal reservoir and the three-way valve. In this part of the study, we have used liquid crystal that was designed to change color when the temperature of the solid onto which the liquid crystal was sprayed varied between 36-38°C. For high quality transient liquid crystal experiments, it is recommended that the normalized wall temperature $\theta(t) = (T_w(t) - T_i)/(T_m(t) - T_i)$ vary between 0.3 and 0.7 for most part of the transient run [1.28]. Since array jet impingement cooling is known to have sharp heat transfer coefficient gradients, maintaining the above-mentioned wall and fluid temperature evolution was challenging. However, with a judicious choice of mainstream temperature evolution with time and the LC color change band, one can closely follow the recommendations for low uncertainties in calculated heat transfer coefficient.

The concept of the LCT experimental setup was similar to that of IRT, except for the difference in their respective heat transfer test sections. In the LCT setup, after the three-way valve the flow was directed into a plenum feed. Honeycomb structures were used in the plenum feed to straighten the flow. After the plenum feed, the flow was directed through the jet plate and onto the target plate. More details on the setup can be found in [1.29].

1.4. DESCRIPTION OF TEST CONFIGURATIONS

1.4.1. Test Configurations for IRT Experiment

The IRT experiment heat transfer test section comprised of a nozzle and target surface made of fused quartz. The quartz plate had dimensions $0.1524\text{m} \times 0.1524\text{m} \times 0.006\text{m}$. The nozzle diameter was 0.02286 m and the jet-to-target spacing ($\frac{z}{d_j}$) was 5. The entire target plate surface was used as the domain for the heat transfer calculation using the 1D and the 3D models. The projection of the jet onto the target surface is shown in Fig. 1.2.

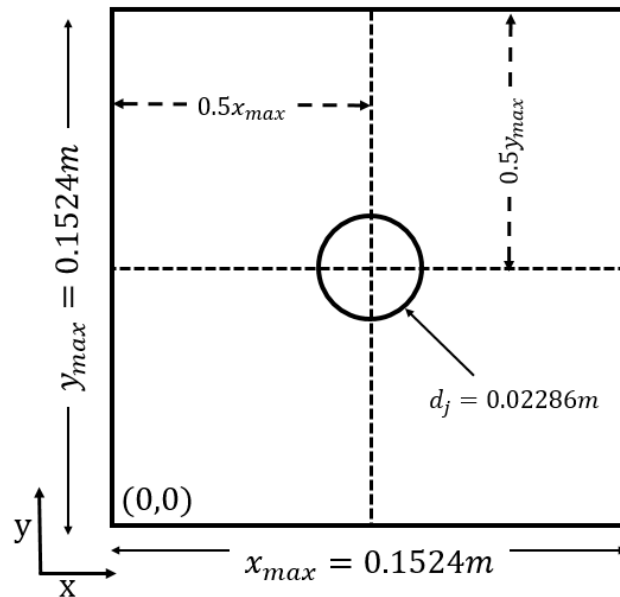


Figure 1.2 Schematic of jet plate for IRT experiment

1.4.2. Test Configurations for LCT Experiment

The LCT test configuration was array jet impingement onto a target surface made out of clear acrylic. The jet plate featured an array of 10×5 nozzles, where the nozzle length-to-diameter ratio

(L/d) was 4. The normalized streamwise (x/d) and spanwise jet-to-jet (y/d) spacing was 6. The jet-to-target (z/d) plate spacing was 2 and the jet diameter jet was 3.175 mm. The spacer which ensures the distance between the jet plate and target was placed such that it yields to the maximum crossflow condition. Figure 1.3 shows the direction of crossflow and the region of interest (ROI) where local heat transfer coefficients were calculated. The ROI was chosen such that adiabatic boundary condition along the side walls could be ensured, and more details pertaining to this has been provided in later sections.

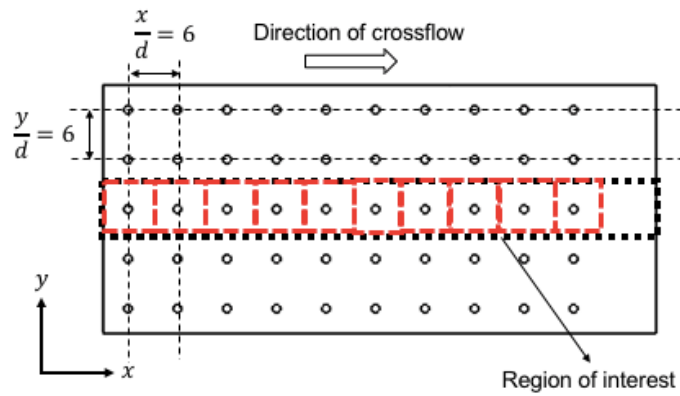


Figure 1.3 Schematic of jet plate and region of interest on the target plate for LCT experiment

1.5. ONE-DIMENSIONAL TRANSIENT HEAT CONDUCTION EQUATION SOLUTION METHODOLOGY

1.5.1. One-Dimensional semi-infinite heat conduction model

The local heat transfer coefficient over the target surface coated with liquid crystals was obtained using 1-D semi-infinite conduction model. One-dimensional transient heat diffusion equation is given as,

$$\frac{\partial T(z, t)}{\partial t} = \alpha \frac{\partial^2 T(z, t)}{\partial z^2} \quad (Eq. 1.1)$$

The two boundary conditions in space (z) and one initial condition (time) are given as,

$$-k \frac{\partial T(0, t)}{\partial z} = h(T_m - T_{z=0}(t)) \quad (Eq. 1.2)$$

$$T(z \rightarrow \infty, t) = T_i \quad (Eq. 1.3)$$

$$T(z, 0) = T_i \text{ at } t = 0 \quad (Eq. 1.4)$$

Equation 1.1 when solved with initial and boundary conditions listed in Eqns. 1.2-1.4 yield the following analytical solution,

$$\frac{T_w(t) - T_i}{T_m - T_i} = 1 - \exp\left(\frac{h^2 t}{\rho c k_s}\right) \operatorname{erfc}\left(h \sqrt{\frac{t}{\rho c k_s}}\right) \quad (Eq. 1.5)$$

Note that the mainstream temperature was assumed constant in the above equation. In our experiments, the air temperature varied with time. Hence above Eq. 1.5 is further modified using Duhamel's superposition principle and is given as,

$$T_w = T_i + \left(\sum_{i=1}^{i=n_{\max}} (T_{m,i} - T_{m,i-1}) \right) \left[1 - \exp\left(\frac{h^2(t - t_i)}{\rho c k_s}\right) \operatorname{erfc}\left(h \sqrt{\frac{t - t_i}{\rho c k_s}}\right) \right] \quad (\text{Eq. 1.6})$$

For more details, the reader is referred to [1.30, 1.31]

1.5.2. Heat transfer coefficient determination for IRT experiment

For the IR experiment, the determination of the heat transfer coefficient was straightforward as the complete time variation of the temperature of the target surface was available. Eq. 1.6 consists of three unknowns, the time (t), wall temperature (T_w) and heat transfer coefficient (h). The mainstream temperature (T_m) was measured just prior to the jet exit plane by a fast-response thin thermocouple. A set value of time (20 seconds) was used and the corresponding IR reading of wall temperature at that time instance was used as T_w , which was exclusive for each pixel since they were associated with different heat transfer coefficients. Now as the only unknown in Eq. 1.6 was the heat transfer coefficient (h), and an iterative error minimization method (bisection method) was carried out to calculate the heat transfer coefficient for each pixel. Deduced heat transfer coefficient was then converted to the following non-dimensional form,

$$Nu = \frac{h(x, y) d_j}{k_f} \quad (\text{Eq. 1.7})$$

where, d_j , is the jet diameter and k_f , is the thermal conductivity of the fluid.

1.5.3. Heat transfer coefficient determination from LCT experiment

The HTC determination procedure in LCT experiment was slightly different from the IRT experiment, since the two experiments differ from the temperature output type. While IRT provides continuous and detailed wall temperature measurements from the initial temperature (T_i), LCT provides the wall temperature information only when the temperature of the solid lies in between the selected color play band of liquid crystals (further away from T_i). Above limitation imposes constraints on the HTC determination procedure. Hence in LCT, a particular wall temperature is used as a reference and the corresponding time taken to reach that wall temperature is determined through elaborate image processing codes. Prior to that, in LCT experiments, a relationship between LC color change and the corresponding wall temperature is established through an in-situ calibration. In present study, a hue-based calibration technique was used and a sample calibration curve is shown in the following figure. More details about the calibration procedure and the HTC determination methodology using 1D semi-infinite conduction modeling can be found in [1.32 - 1.35].

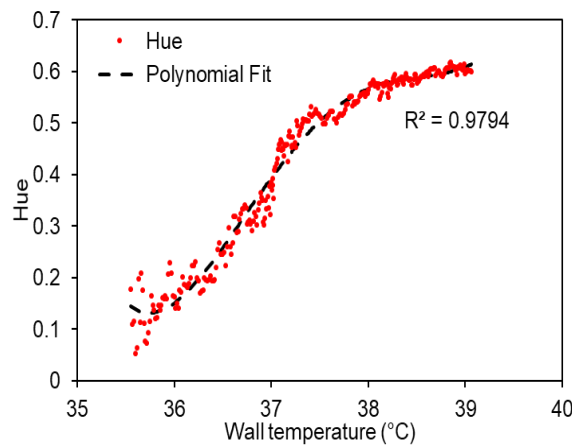


Figure 1.4 Variation of hue with wall temperature

For this study, the reference value of hue was taken as 0.5 and the corresponding wall temperature was 37.5°C. As in the IRT experiment, the plenum temperature, measured as an average of two different thermocouple measurements in the plenum, was used as the mainstream temperature. The initial temperature T_i was calculated by averaging the surface thermocouple measurements before the start of the experiment.

An in-house MATLAB code was used to determine the time at which a particular pixel reached the reference hue value. This operation was performed for all pixels in the domain of interest and a time matrix t_{exp} to reach the particular wall reference temperature was obtained. A similar error minimization process as mentioned in the previous section was carried out to calculate the heat transfer coefficient.

1.6. THREE-DIMENSIONAL TRANSIENT HEAT CONDUCTION EQUATION SOLUTION METHODOLOGY

1.6.1. Three-dimensional heat conduction model

The three-dimensional heat conduction without internal heat generation is given as,

$$\frac{\partial T(x, y, z, t)}{\partial t} = \alpha \left[\frac{\partial^2 T(x, y, z, t)}{\partial x^2} + \frac{\partial^2 T(x, y, z, t)}{\partial y^2} + \frac{\partial^2 T(x, y, z, t)}{\partial z^2} \right] \quad (Eq. 1.8)$$

Eq. 8 was solved using finite difference method (FDM). Using the central finite-difference discretization scheme, the first order and the second-order partial derivatives are given as,

$$\frac{\partial T}{\partial x} \approx \frac{T_{i+1,j,k}^n - T_{i-1,j,k}^n}{2\Delta x} \quad (Eq. 1.9)$$

$$\frac{\partial^2 T}{\partial x^2} = \frac{\partial}{\partial x} \left(\frac{\partial T}{\partial x} \right) \approx \frac{T_{i+1,j,k}^n + T_{i-1,j,k}^n - 2T_{i,j,k}^n}{(\Delta x)^2} \quad (Eq. 1.10)$$

where $T_{i,j,k}^n$ represents the temperature of the discrete point (x, y, z) at the time instant t . A similar discretization process is used for the y and z directions.

The three-dimensional heat equation is commonly discretized in the following time marching methods.

Explicit Method:

$$\frac{T^{n+1} - T^n}{\Delta t} = \alpha \left[\frac{\delta_x^2(T^n)}{\Delta x^2} + \frac{\delta_y^2(T^n)}{\Delta y^2} + \frac{\delta_z^2(T^n)}{\Delta z^2} \right] \quad (Eq. 1.11)$$

The explicit method has second order accuracy in space and first order accuracy in time. The explicit method is only conditionally stable and the stability criteria is given as,

$$\alpha \Delta t \left(\frac{1}{(\Delta x)^2} + \frac{1}{(\Delta y)^2} + \frac{1}{(\Delta z)^2} \right) \leq \frac{1}{2} \quad (Eq. 1.12)$$

Implicit Method:

$$\frac{T^{n+1} - T^n}{\Delta t} = \alpha \left[\frac{\delta_x^2(T^{n+1})}{\Delta x^2} + \frac{\delta_y^2(T^{n+1})}{\Delta y^2} + \frac{\delta_z^2(T^{n+1})}{\Delta z^2} \right] \quad (Eq. 1.13)$$

The implicit method is unconditionally stable and has second order accuracy in space and first order accuracy in time.

Crank-Nicolson Method:

The Crank-Nicolson method takes an average of the implicit and explicit methods.

$$\frac{T^{n+1} - T^n}{\Delta t} = \alpha \left[\frac{\delta_x^2(T^{n+1} + T^n)}{2\Delta x^2} + \frac{\delta_y^2(T^{n+1} + T^n)}{2\Delta y^2} + \frac{\delta_z^2(T^{n+1} + T^n)}{2\Delta z^2} \right] \quad (Eq. 1.14)$$

where, $\delta_x^2 T^n = T_{i+1,j,k}^n + T_{i-1,j,k}^n - 2T_{i,j,k}^n$.

The Crank-Nicolson method has the highest accuracy, as it is second order in both space and time and is unconditionally stable. For a 3D grid with N grid points, the Implicit Method and the Crank-Nicolson method requires a sparse N × N coefficient matrix which needs to be inverted at every time-step to solve for the temperature at every grid point. This makes the Implicit and Crank-Nicolson methods computationally expensive for 3D grids.

1.6.2. Three-dimensional heat conduction model

The alternating direction implicit methods are a variation of the Crank-Nicolson method for solving PDEs in two and three dimensions. The common ADI methods have been developed by Peaceman-Rachford [1.36] and Douglas-Gun [1.37]. ADI methods are very efficient as they reduce complex 2D and 3D PDEs to the problem of solving tridiagonal linear systems along the coordinate system. Peaceman-Rachford approach is only conditionally stable for 3-D problems. In this study, the Douglas-Gunn approach is used, which is unconditionally stable.

The ADI method for a three-dimensional problem splits one time step into three different sub-time steps of equal size. In the first sub-time-step, the implicit scheme was used for one dimension and the explicit scheme was used for the other two directions. Then for the next sub time steps, the direction was switched in a sequential manner, where the updated solutions of the previous sub-time-step was used. This process was continued by alternating the direction of implicit and explicit formulation. For a three-dimensional problem containing N interior nodes in each direction, the ADI method reduces the system of N^3 simultaneous equations to $3N$ equations for each time step, thus resulting in significant reduction of computational cost and time. Thus for the problems discussed in this study the ADI method is more apt and efficient as compared to the conventional methods such as the Gauss-Sidel Method.

The finite difference form of Eq. 1.8 is written in the discretized Crank-Nicolson form as,

$$\frac{T^{n+1} - T^n}{\Delta t} = \alpha \left[\frac{\delta_x^2(T^{n+1} + T^n)}{2\Delta x^2} + \frac{\delta_y^2(T^{n+1} + T^n)}{2\Delta y^2} + \frac{\delta_z^2(T^{n+1} + T^n)}{2\Delta z^2} \right] \quad (Eq. 1.15)$$

The Douglas-Gunn ADI method splits the above step into three different time steps as follows. For the first sub time-step, employing the implicit scheme in x-direction and the explicit scheme in the y- and z-directions, Eq. 1.14 is written as,

$$\frac{T^{n+\frac{1}{3}} - T^n}{\Delta t} = \alpha \left[\frac{\delta_x^2 \left(T^{n+\frac{1}{3}} + T^n \right)}{2\Delta x^2} + \frac{\delta_y^2(T^n)}{\Delta y^2} + \frac{\delta_z^2(T^n)}{\Delta z^2} \right] \quad (Eq. 1.16)$$

Simplifying the above equation yields,

$$T^{n+\frac{1}{3}} - T^n = \frac{r_x \delta_x^2}{2} \left(T^{n+\frac{1}{3}} + T^n \right) + r_y \delta_y^2 T^n + r_z \delta_z^2 T^n \quad (I) \quad (Eq. 1.17)$$

Similarly, the equations for the next two sub time-steps are of the form,

$$T^{n+\frac{2}{3}} - T^n = \frac{r_x \delta_x^2}{2} \left(T^{n+\frac{1}{3}} + T^n \right) + r_y \delta_y^2 \left(T^{n+\frac{2}{3}} + T^n \right) + r_z \delta_z^2 T^n \quad (II) \quad (Eq. 1.18)$$

$$T^{n+\frac{2}{3}} - T^n = \frac{r_x \delta_x^2}{2} \left(T^{n+\frac{1}{3}} + T^n \right) + r_y \delta_y^2 \left(T^{n+\frac{2}{3}} + T^n \right) + r_z \delta_z^2 (T^{n+1} + T^n) \quad (III) \quad (Eq. 1.19)$$

where,

$$r_x = \frac{\alpha \Delta t}{\Delta x^2}, r_y = \frac{\alpha \Delta t}{\Delta y^2} \text{ and } r_z = \frac{\alpha \Delta t}{\Delta z^2}$$

Grouping all the unknowns onto one side of the equation, the above equations are simplified as,

$$\begin{aligned} & -r_x T_{i-1,j,k}^{n+\frac{1}{3}} + 2(1+r_x)T_{i,j,k}^{n+\frac{1}{3}} - r_x T_{i+1,j,k}^{n+\frac{1}{3}} \\ & = r_x T_{i-1,j,k}^n + 2r_y T_{i,j-1,k}^n + 2r_z T_{i,j,k-1}^n + r_x T_{i+1,j,k}^n + 2r_y T_{i,j+1,k}^n + 2r_z T_{i,j,k+1}^n \\ & + 2(1-r_x-2r_y-2r_z)T_{i,j,k}^n \quad (Eq. 1.20) \end{aligned}$$

$$\begin{aligned} & -r_y T_{i,j-1,k}^{n+\frac{2}{3}} + 2(1+r_y)T_{i,j,k}^{n+\frac{2}{3}} - r_y T_{i,j+1,k}^{n+\frac{2}{3}} \\ & = r_x T_{i-1,j,k}^n + 2r_y T_{i,j-1,k}^n + 2r_z T_{i,j,k-1}^n + r_x T_{i+1,j,k}^n + 2r_y T_{i,j+1,k}^n + 2r_z T_{i,j,k+1}^n \\ & + 2(1-r_x-2r_y-2r_z)T_{i,j,k}^n \\ & + \left(r_x T_{i-1,j,k}^{n+\frac{1}{3}} - 2r_x T_{i,j,k}^{n+\frac{1}{3}} + r_x T_{i+1,j,k}^{n+\frac{1}{3}} \right) \quad (Eq. 1.21) \end{aligned}$$

$$\begin{aligned} & -r_z T_{i,j,k+1}^{n+1} + 2(1+r_z)T_{i,j,k}^{n+1} - r_z T_{i,j,k+1}^{n+1} \\ & = r_x T_{i-1,j,k}^n + 2r_y T_{i,j-1,k}^n + 2r_z T_{i,j,k-1}^n + r_x T_{i+1,j,k}^n + 2r_y T_{i,j+1,k}^n + 2r_z T_{i,j,k+1}^n \\ & + 2(1-r_x-2r_y-2r_z)T_{i,j,k}^n + r_x T_{i-1,j,k}^{n+\frac{1}{3}} - 2r_x T_{i,j,k}^{n+\frac{1}{3}} + r_x T_{i+1,j,k}^{n+\frac{1}{3}} + r_y T_{i,j-1,k}^{n+\frac{2}{3}} \\ & - 2r_y T_{i,j,k}^{n+\frac{2}{3}} + r_y T_{i,j+1,k}^{n+\frac{2}{3}} \quad (Eq. 1.22) \end{aligned}$$

Each of these equations above have three unknown variables. These three unknowns for each direction form a tridiagonal matrix. The tridiagonal matrix was solved by using the Thomas algorithm subjected to the boundary conditions as discussed in the next section.

1.6.3. Boundary conditions

The transient 3D heat conduction equation requires six boundary conditions in space and one initial condition in time. The heat conduction equation was solved with the following boundary conditions and initial conditions for the chosen ROI ($x_{max} \times y_{max}$).

$$T(x, y, z, 0) = T_i \quad (Eq. 1.23)$$

$$-k \frac{\partial T(x, y, 0, t)}{\partial z} = h(T(x, y, 0, t) - T_m(t)) \quad (Eq. 1.24)$$

$$T(x, y, z \rightarrow \infty) = T_i \quad (Eq. 1.25)$$

$$-k \frac{\partial T(0, y, z, t)}{\partial x} = 0 \quad (Eq. 1.26)$$

$$-k \frac{\partial T(x, 0, z, t)}{\partial y} = 0 \quad (Eq. 1.27)$$

$$-k \frac{\partial T(x_{max}, y, z, t)}{\partial x} = 0 \quad (Eq. 1.28)$$

$$-k \frac{\partial T(x, y_{max}, z, t)}{\partial y} = 0 \quad (Eq. 1.29)$$

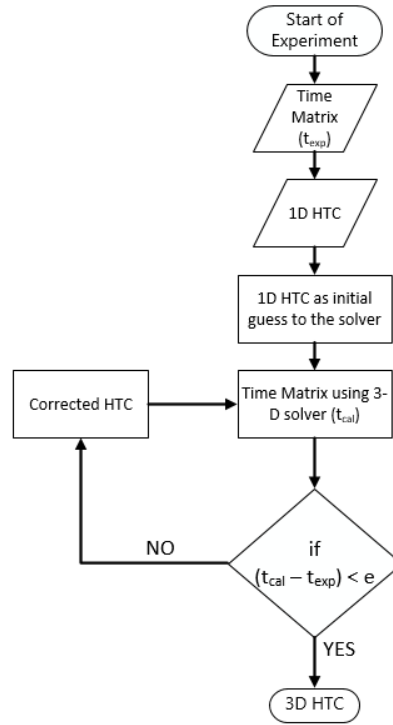


Figure 1.5 Flowchart of heat transfer calculation methodology in 3D conduction modeling

For IRT experiment

For the IRT experiment the entire solid was modeled as the ROI. Ignoring the natural convection on the side faces (four of them) of the quartz plate, the sides $x = 0, x = x_{max}, y = 0$, and $y = y_{max}$, were assumed to be adiabatic.

For LCT experiment

The boundaries along $x = 0$ and $x = x_{max}$ were assumed to be adiabatic as they represent the end of the solid domain and the natural convection heat transfer occurring across these planes were considered to be very small compared to the conduction within the solid. Also,

since the region of interest is symmetric along x-z planes at $y = 0$ and $y = y_{max}$, there will be negligible net conduction across these planes. Hence, adiabatic boundary condition is used on these planes.

1.6.4. Heat transfer coefficient determination methodology: 3D conduction modeling

For the present problem, the time taken for each point to reach a specific temperature was known, by tracking a certain reference Hue value. This was logged as the time matrix for the experiment in the region of interest (t_{exp}). Note that till this point, the methodology is same as the 1D semi-infinite procedure discussed above.

The procedure to calculate the heat transfer coefficient considering 3D heat conduction was split into two steps. A flow chart of the procedure discussed below is shown in Fig. 1.5. In the first step, the heat transfer coefficient obtained from the 1D heat conduction model was used to solve Eq. 1.6 using the ADI method with boundary conditions provided in Eqns. 1.23-1.29. The temperature at every grid point (x, y, z) was calculated over the entire duration of the experiment. Now the time taken for each grid point on the target surface to reach the reference temperature was obtained as a new time matrix denoted as t_{cal} .

In the second step, the new numerically calculated time matrix (t_{cal}) was compared with the experimental time matrix (t_{exp}) for each pixel. If the difference was greater than the convergence limit for each pixel, the value of heat transfer coefficient was corrected by using the bisection method as shown below,

$$h_n = h_{n_1} - \left(\frac{h_{n_1} - h_{n_2}}{time_{n_1} - time_{n_2}} \right) (time_{n_1} - time_{exp}) \quad (Eq. 1. 30)$$

where, ‘n’ represents the current guess and n1, n2 represents the two limits. The 1D heat transfer coefficient (h_{1D}) was used as the initial guess and the two initial limits were $0.2h_{1D}$ and $1.8h_{1D}$.

This process of comparing the time matrices and accordingly correcting the heat transfer coefficient was iteratively repeated until the difference between the calculated value of time matrix and the experimental time matrix satisfied the convergence criteria. An in-house MATLAB program was written to implement the above scheme.

1.7. RESULTS AND DISCUSSION

This section presents the Nusselt Number calculated using the 1D and 3D conduction models discussed above, for different test configurations.

1.7.1. Demonstration study

For validation of the above methodology, a preliminary numerical study was carried out. This demonstration study was divided in two main steps. In the first step, a known heat transfer coefficient map was imposed on the target surface of a solid. Using a known time-varying mainstream temperature, the temperature evolution of each finite-volume in the solid domain was computed. In the second step, this temperature variation of the target surface was used as an input for the 1D and 3D conduction models and the heat transfer coefficient were back-calculated and

compared with the initial heat transfer coefficient map. This part of the study was carried out as a form of validation of the 3D conduction model used in this study.

Table 1.1 Parameters used in initial study

Nusselt Number Correlation	$Nu = \frac{Re^{0.6}}{4.577 + 0.4357(x/d)^{1.14}}$
Initial Temperature of solid	300K
Reference Temperature	307K
Mainstream Temperature	$300 + 40(1 - e^{-(0.1t)})$
Thermal Diffusivity of solid	$1.1e^{-7} m^2/s$
Thermal Conductivity of solid	0.19 W/mK
Time step size	0.05 sec
Total time duration	20 sec

Table 1.2 Grid Independence study

Coarse	$50 \times 50 \times 25$
Medium	$180 \times 180 \times 51$
Fine	$300 \times 300 \times 101$

For the first step, a radially varying Nusselt number correlation corresponding to a single jet impingement of $z/d = 12$, for $Re=10,000$ and $d_j=0.019m$ was used from [1.38]. From the radially varying Nusselt number, a two-dimensional distribution of Nusselt number was generated by a 360-degree sweep in a square region of interest. A cuboidal solid body with dimensions of

0.152m×0.152m×0.0127m was used for this study. An exponentially varying mainstream temperature was assumed and the temperature variation of this solid was computed by running a transient simulation on ANSYS Fluent 16.1 (academic license). A hexahedral mesh consisting of 181×181×51 cells with uniform spacing was used for this study. More details about the case setup is provided in Table 1.1.

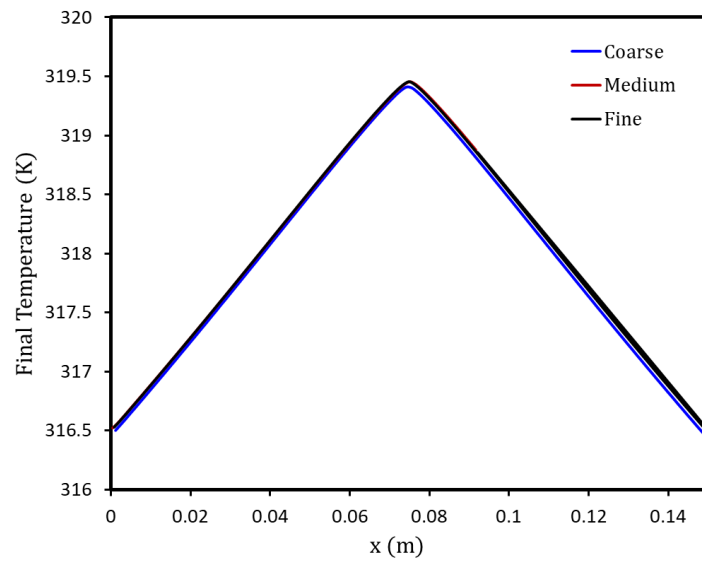


Figure 1.6 Comparison of final temperature for grid independence study

To ensure the results were not sensitive to grid size, a mesh independence study was also carried out and the details of the three grids investigated are provided in Table 1.1. The mesh independence study was carried out by comparing the final temperature obtained at the end of the first step as shown in Fig. 1.6. The medium mesh was found to be a conservative scheme and was used in subsequent calculations. The boundary treatment as discussed in section 1.5(c) was used here, with the 0.152m×0.152m face as the target surface. The time step size used for this simulation

was set to 0.05 sec and the simulation was run for a total physical time of 20 seconds. Time matrix was calculated for each pixel for a set reference surface temperature of 307K.

Now the calculated time matrix was used as an input for the 1D and 3D conduction models, and the Nusselt numbers were back-calculated through the procedure mentioned above. The radial variation of Nusselt number calculated from the two models were plotted against the initial Nusselt Number correlation used (Fig. 1.7).

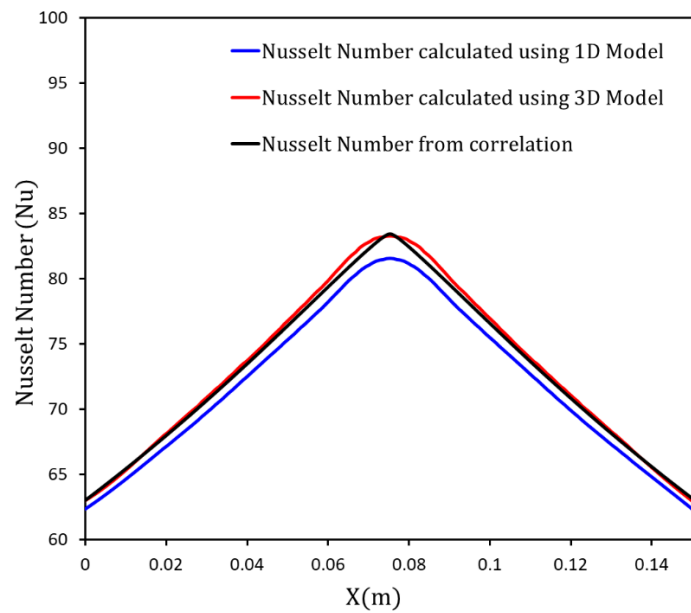


Figure 1.7 Comparison of radially varying Nusselt Number

From Fig. 1.7, it can be seen that the 3D heat conduction model better captures the local Nusselt numbers, particularly near the stagnation region, when compared to 1D conduction model. The 1D heat conduction model under-predicted the Nusselt number. This is attributed to the fact that 1D heat transfer model, does not take into account the lateral heat flow. This decrease in heat

flux leads to decrease in the Nusselt Number calculated using the 1D heat conduction model. The Nusselt number obtained using the 1D model was found to be 2-4% lower than the Nusselt number used from correlation.

1.7.2. Heat transfer coefficient calculations through different models (1D and 3D conduction) for IRT experiment

Heat transfer coefficient for 1D and 3D conduction models for the single jet impingement configuration where temperatures were measured by infrared camera is discussed below. A grid independence study was carried out in this configuration as well (Table 1.3 and Fig. 1.8). The medium grid scheme was used for subsequent calculations.

Table 1.3 Grid Independence study

Coarse	$200 \times 200 \times 8$
Medium	$400 \times 400 \times 20$
Fine	$750 \times 750 \times 40$

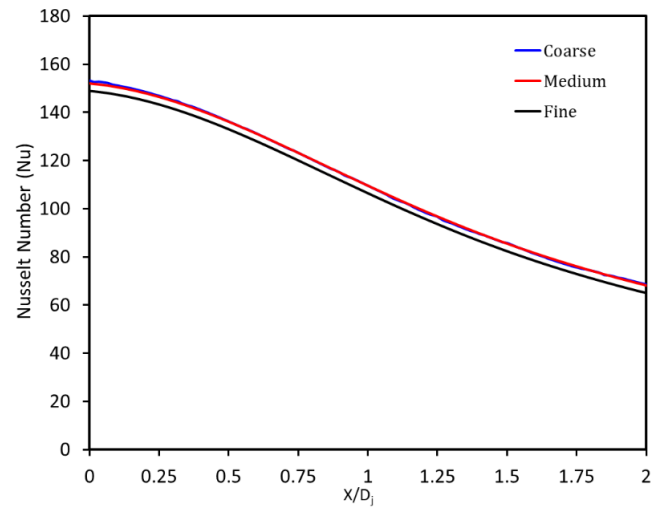


Figure 1.8 Grid Independence study

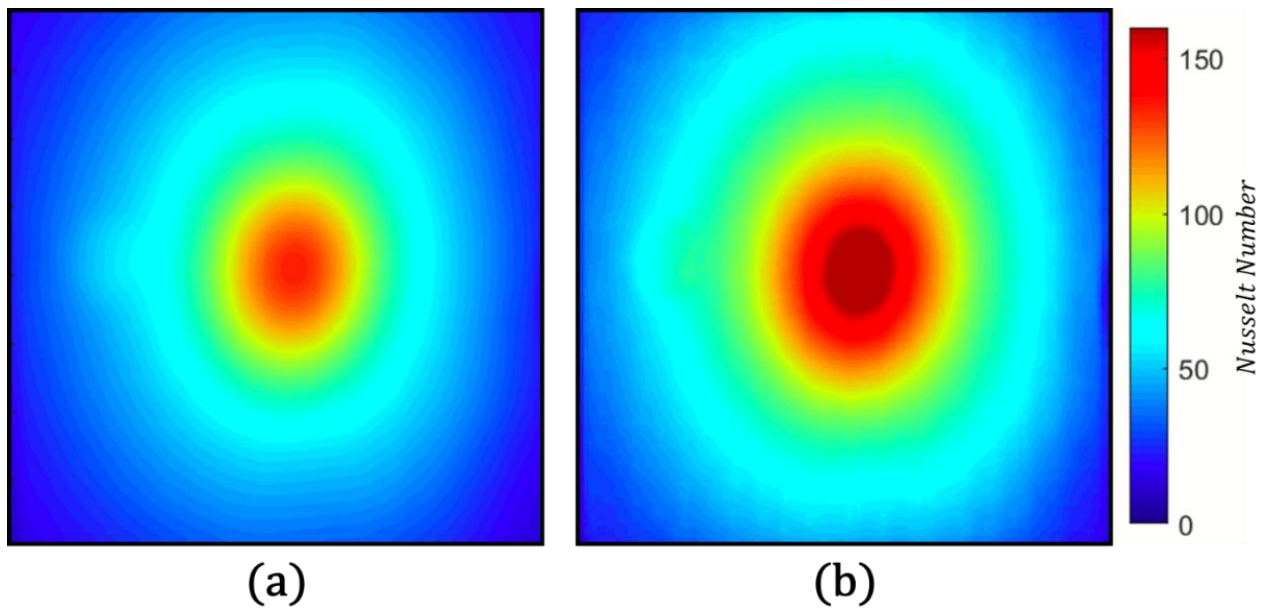


Figure 1.9 Detailed Nusselt Number Comparison for (a) 1D Model (b) 3D Model

Figure 1.9 show the detailed Nusselt Number distribution for Reynolds number ($Re = 20760$) calculated using the one-dimensional and three-dimensional heat conduction models. The Nusselt number obtained using the 3D model was found to be consistently higher than the Nusselt number obtained using the 1D model. The difference between the 1D and the 3D models was most pronounced at the stagnation region, where $\sim 20\%$ difference was observed between the two.

The radial variation of Nusselt number obtained using both the models had a good agreement with Hollworth and Gero [1.39] ($Re = 20,000$), where the Nusselt number predicted by 3D model closely mimicked the radial variation trends as in [1.39].

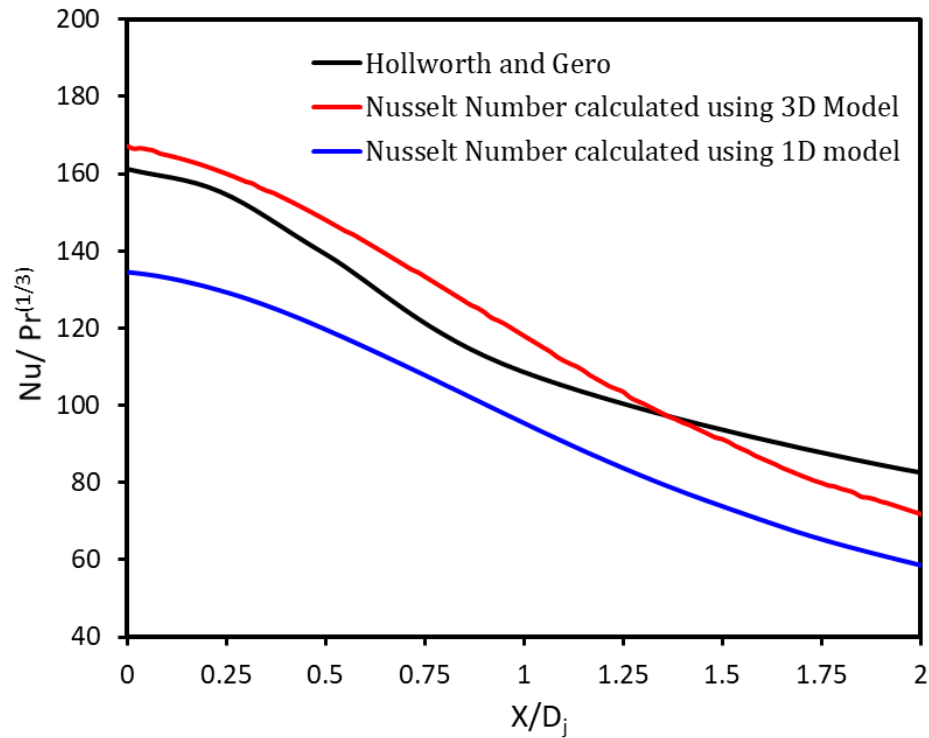


Figure 1.10 Comparison of radial variation of Nusselt Number with Hollworth and Gero

[1.32]

1.7.3. Heat transfer coefficient calculations through different models (1D and 3D conduction) for LCT experiment

For the array jet impingement case, the wall temperatures were measured by liquid crystal thermography and the detailed procedure is mentioned in above sections. In this configuration as well, a separate grid independence study was carried out by comparing the row-wise averaged Nusselt number (Table 1.4 and Fig. 1.11). The medium size grid scheme was used in the subsequent calculations.

Table 1.4 Grid Independence study

Coarse	$500 \times 50 \times 25$
Medium	$1005 \times 110 \times 51$
Fine	$1300 \times 125 \times 75$

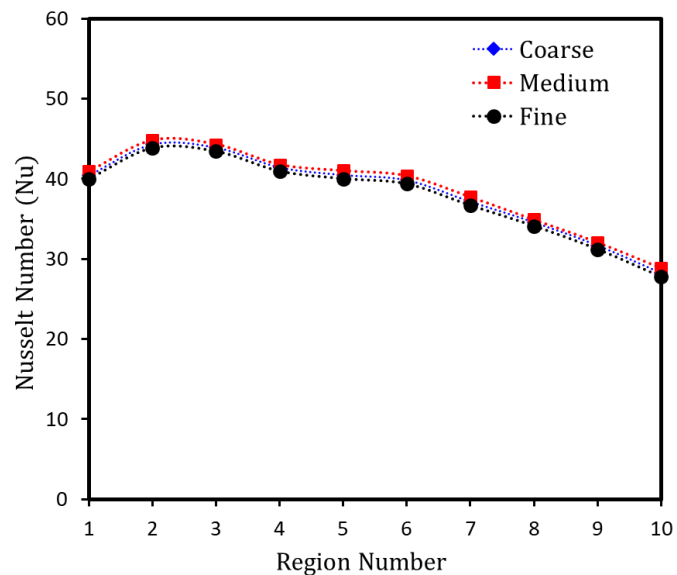


Figure 1.11 Grid Independence study

Figure 1.12 show the detailed Nusselt Number distribution for four different Reynolds numbers calculated using the one-dimensional and three-dimensional heat conduction models. The four Reynolds numbers (Re_d) investigated in this study were 3480, 5163, 7321 and 10865. Since maximum crossflow condition was investigated, a significant degradation in local heat transfer levels was observed for downstream jets due to increased strength of crossflow mass flux compared to the jet mass flux. Such a case was undertaken for the demonstration purpose since wide range of local Nusselt numbers were present in a single solid domain. While solving the 3D conduction equations with the boundary conditions mentioned, every pixel in the solid domain had a role to play in determination of local heat transfer coefficients. Hence, in order to bring out substantial differences between the Nusselt numbers computed by considering 1D and 3D conduction models, above configuration was chosen.

The Nusselt Numbers calculated by the 3D model were overall greater than that calculated using the 1D conduction model. A consistent increase in the Nusselt number calculated using the 3D model was observed across all the Reynolds numbers used in this study.

A consistent increase in Nusselt number calculated by the 3D model is also observed in the streamwise averaged Nusselt number plotted in Fig. 1.13. The highest difference in the heat transfer coefficient calculated by the 1D and 3D model was found to be near the stagnation regions. The spanwise averaged Nusselt number calculated in the stagnation region of the jets by both the models differed about 8-20%. This is due to the stagnation region being dominated by strong lateral conduction effects, due to which, the net heat flux transferred by the fluid to the solid as calculated from the 1D model was lower than the 3D model. Hence the 1D heat conduction model under predicts the heat transfer, especially at the stagnation regions.

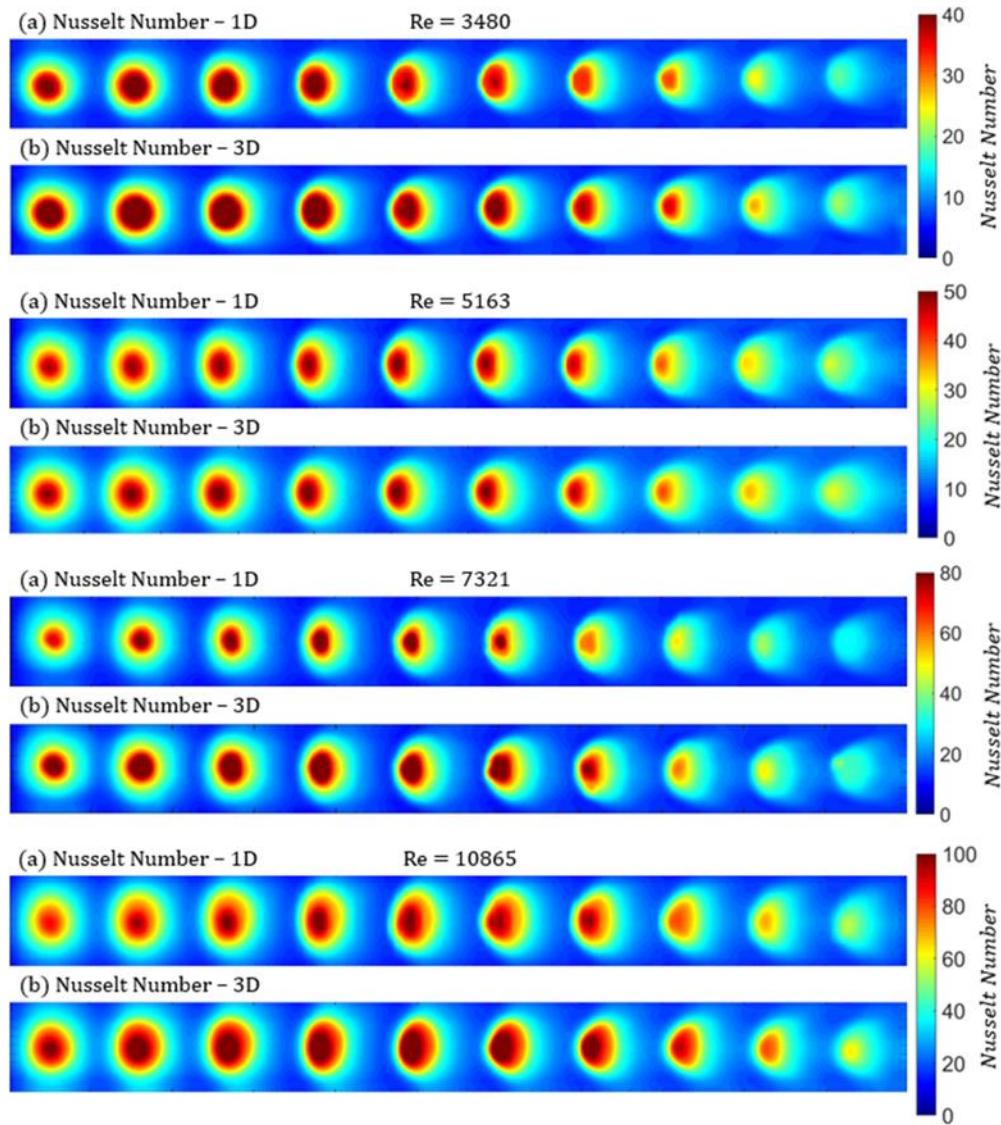


Figure 1.12 Detailed Nusselt Number distribution

Similar study was carried out by Nirmalan et al. [1.23] on array jet impingement onto metallic target, where the authors provided local comparison of heat transfer coefficient predicted by 1D (lumped capacitance) and 3D conduction models. The authors showed that the HTC's predicted by 3D conduction were consistently higher by about 30% when compared to 1D conduction model. The differences observed by [1.23] were significantly larger compared to the

present study because of two reasons, firstly, the comparisons were made between lumped capacitance and 3D conduction models and second, the target surface was metal. Due to high thermal diffusivity of metal, the lateral conduction effects in the transient experiment will be even more pronounced when compared to a solid such as clear acrylic. Hence, the 3D conduction model heat transfer coefficient will differ significantly.

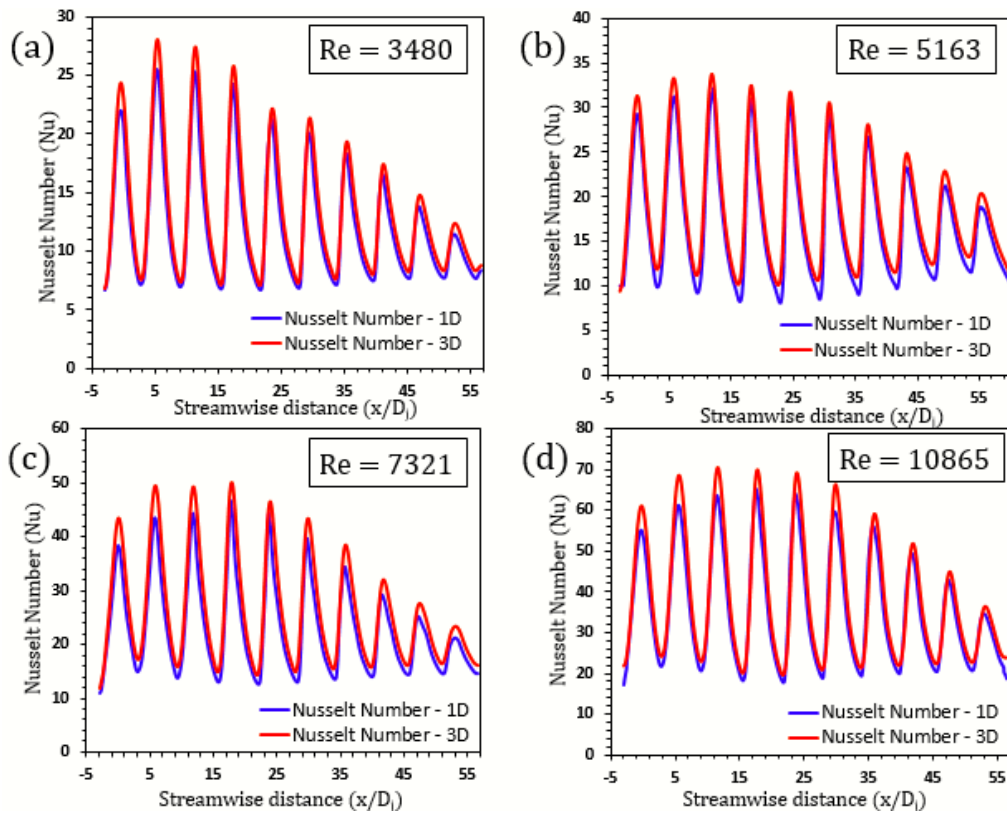


Figure 1.13 Spanwise-averaged Nusselt Number

From the row-wise averaged Nusselt number plot for all Reynolds Numbers (Fig. 1.14) it is observed that, the Nusselt number calculated using the 3D model was consistently 3-16% higher than the 1D Nusselt Number. The difference between the models was found to be more pronounced

in the initial regions than in the regions closest to the exit. This is attributed to the fact that the stagnation region and the associated thermal gradients were washed out by the crossflow of spent jets.

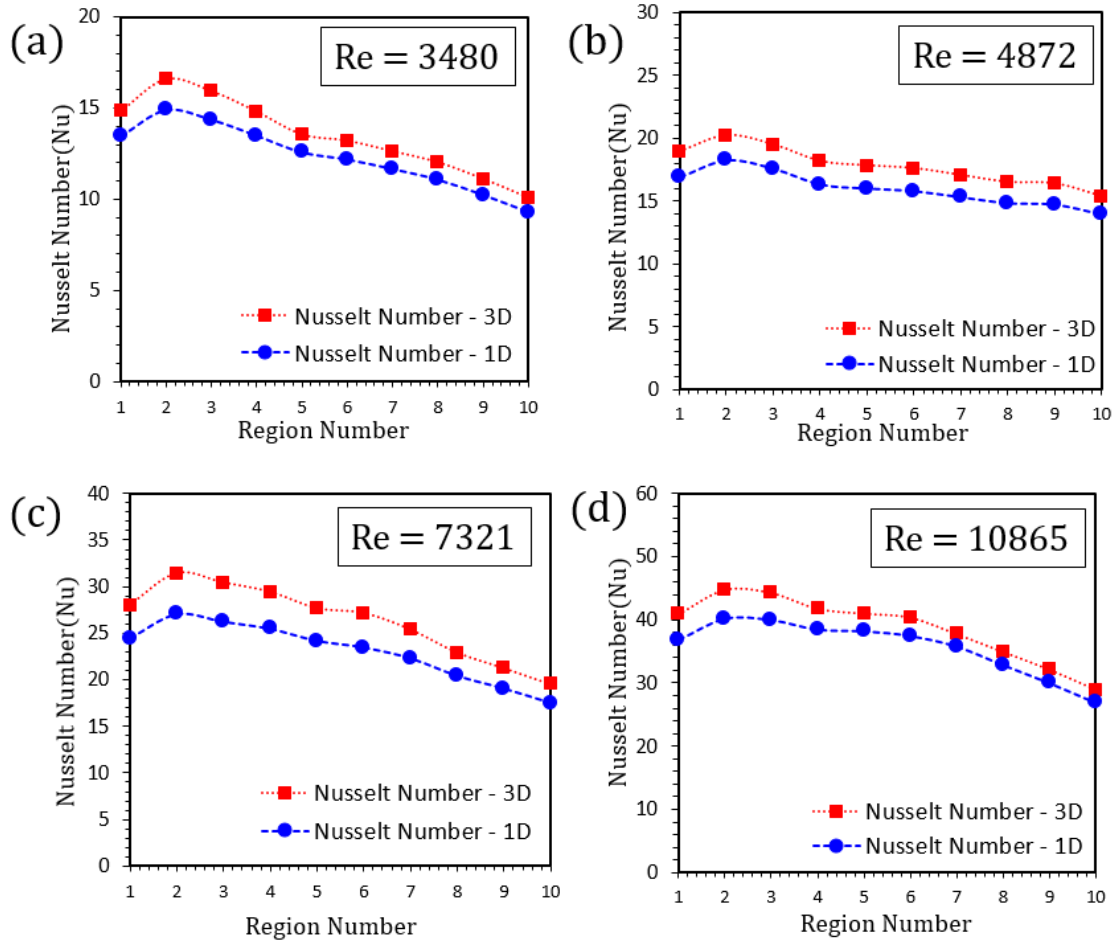


Figure 1.14 Row-wise Averaged Nusselt Number

The globally averaged Nusselt numbers calculated using both the models was found to have a reasonable agreement with Florschuetz et al. [1.40]. A 7-14% increase was observed in the

average Nusselt number calculated by the 1D and the 3D heat conduction models. The area averaged Nusselt number obtained using the 3D model was found to be in closer agreement with correlation obtained from Florschuetz et al. [1.40]. Similar comparison was provided by Nirmalan et al. [23] where 3D conduction model was in close agreement with Florschuetz et al. [1.40].

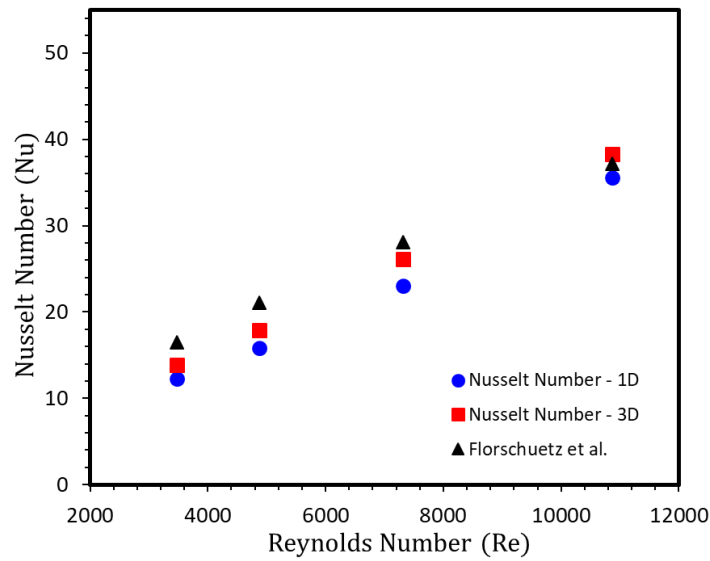


Figure 1.15 Comparison of Area Averaged Nusselt number for 1D and 3D Model with Florschuetz et al. [1.40]

1.8. CONCLUSIONS

A technique to account for three-dimensional heat conduction in transient liquid crystal (LCT) and Infrared thermography (IRT) experiments using the alternating direction implicit method was demonstrated in this study. Representative cases of a single jet (IRT) and an array of jets (LCT) were considered for to demonstrate the applicability of the proposed methodology and heat transfer coefficients were calculated using the 1D semi-infinite conduction model (h_{1D}) and

3D heat conduction model (h_{3D}). The results obtained using both the models were compared and it was found that the HTC calculated using the 3D model was consistently higher than the conventional 1D model by 7-14%, where deviations between h_{1D} and h_{3D} were as high as 8-20% near the stagnation regions. It is concluded that lateral heat diffusion, when not accounted, may lead to significant errors in HTC calculations, even in the case of solids with low thermal conductivity and thermal diffusivity. ADI method for solving the three-dimensional heat diffusion equation proved to be computationally efficient and is recommended for experimental studies employing advanced thermal diagnostic techniques based on detailed surface temperature measurements.

NOMENCLATURE

c specific heat capacity of target surface

h heat transfer coefficient

t time

T Temperature

Nu local Nusselt number

Re Reynolds number

Greek symbols

α Thermal diffusivity

ρ density

Subscripts

i initial

j jet

<i>s</i>	solid
<i>f</i>	fluid
<i>m</i>	mainstream
<i>w</i>	wall

Abbreviations

<i>1D</i>	One-Dimensional
<i>3D</i>	Three Dimensional
<i>HTC</i>	Heat Transfer Coefficient
<i>IRT</i>	Infrared Thermography
<i>LCT</i>	Liquid Crystal Thermography
<i>RGB</i>	Red, Green and Blue
<i>ABS</i>	Acrylonitrile Butadiene Styrene

REFERENCES

- [1.1] Singh, P., Ravi, B.V. and Ekkad, S.V., 2016. Experimental and numerical study of heat transfer due to developing flow in a two-pass rib roughened square duct. *International Journal of Heat and Mass Transfer*, 102, pp.1245-1256.
- [1.2] Ravi, B.V., Singh, P. and Ekkad, S.V., 2017. Numerical investigation of turbulent flow and heat transfer in two-pass ribbed channels. *International Journal of Thermal Sciences*, 112, pp.31-43.
- [1.3] Singh, P., Ji, Y. and Ekkad, S.V., 2018. Experimental and numerical investigation of heat and fluid flow in a square duct featuring criss-cross rib patterns. *Applied Thermal Engineering*, 128, pp.415-425.
- [1.4] Zhang, M., Singh, P. and Ekkad, S.V., 2019. Rib Turbulator Heat Transfer Enhancements at Very High Reynolds Numbers. *Journal of Thermal Science and Engineering Applications*, 11(6), p.061014.
- [1.5] Singh, P., Ji, Y. and Ekkad, S.V., 2019. Multi-Pass Serpentine Cooling Designs for Negating Coriolis Force Effect on Heat Transfer: 45-Degree Angled Rib Turbulated Channels. *ASME. J. Turbomach.*
- [1.6] Yang, L., Singh, P., Tyagi, K., Pandit, J., Ekkad, S.V. and Ren, J., 2018. Experimental Investigation of Rotational Effects on Heat Transfer Enhancement Due to Crossflow-Induced Swirl Using Transient Liquid Crystal Thermography. *Journal of Thermal Science and Engineering Applications*, 10(3), p.031001.
- [1.7] Kaur, I., Singh, P. and Ekkad, S.V., 2019. Thermal-hydraulic performance enhancement by combination of rectangular winglet pair and V-shaped dimples. *Journal of Thermal Science and Engineering Applications*, pp.1-17.

- [1.8] Han, J.C., Dutta, S. and Ekkad, S., 2012. Gas turbine heat transfer and cooling technology. CRC press.
- [1.9] Singh, P., Zhang, M., Ahmed, S., Ramakrishnan, K.R. and Ekkad, S., 2019. Effect of micro-roughness shapes on jet impingement heat transfer and fin-effectiveness. *International Journal of Heat and Mass Transfer*, 132, pp.80-95.
- [1.10] Goldstein, R.J. and Timmers, J.F., 1982. Visualization of heat transfer from arrays of impinging jets. *International Journal of Heat and Mass Transfer*, 25(12), pp.1857-1868.
- [1.11] Ireland, P. T., and T. V. Jones. "The measurement of local heat transfer coefficients in blade cooling geometries." In *AGARD Heat Transfer and Cooling in Gas Turbines* 8 p (SEE N86-29823 21-07). 1985,
- [1.12] Vedula, R.P., Metzger, D.E. and Bickford, W.B., 1988, November. Effects of lateral and anisotropic conduction on determination of local convection heat transfer characteristics with transient tests and surface coatings. In *Winter Annual Meeting of ASME, HTD-I* (pp. 21-27).
- [1.13] Camci, C., Kim, K. and Hippensteele, S.A., 1991, June. A new hue capturing technique for the quantitative interpretation of liquid crystal images used in convective heat transfer studies. In *ASME 1991 International Gas Turbine and Aeroengine Congress and Exposition* (pp. V004T09A009-V004T09A009). American Society of Mechanical Engineers.
- [1.14] Ekkad, S.V. and Han, J.C., 1997. Detailed heat transfer distributions in two-pass square channels with rib turbulators. *International Journal of Heat and Mass Transfer*, 40(11), pp.2525-2537.

- [1.15] Ekkad, S.V., Zapata, D. and Han, J.C., 1995, June. Film effectiveness over a flat surface with air and CO₂ injection through compound angle holes using a transient liquid crystal image method. In ASME 1995 International Gas Turbine and Aeroengine Congress and Exposition (pp. V004T09A011-V004T09A011). American Society of Mechanical Engineers.
- [1.16] Carlomagno, G.M. and Cardone, G., 2010. Infrared thermography for convective heat transfer measurements. *Experiments in fluids*, 49(6), pp.1187-1218.
- [1.17] Ekkad, S.V., Ou, S. and Rivir, R.B., 2004. A transient infrared thermography method for simultaneous film cooling effectiveness and heat transfer coefficient measurements from a single test. *Journal of Turbomachinery*, 126(4), pp.597-603.
- [1.18] Ramesh, S., Ramirez, D.G., Ekkad, S.V. and Alvin, M.A., 2016. Analysis of film cooling performance of advanced tripod hole geometries with and without manufacturing features. *International Journal of Heat and Mass Transfer*, 94, pp.9-19.
- [1.19] Xue, S., Roy, A., Ng, W.F. and Ekkad, S.V., 2015. A novel transient technique to determine recovery temperature, heat transfer coefficient, and film cooling effectiveness simultaneously in a transonic turbine cascade. *Journal of Thermal Science and Engineering Applications*, 7(1), p.011016.
- [1.20] Ling, J.C., Ireland, P.T. and Turner, L., 2003, January. A technique for processing transient heat transfer, liquid crystal experiments in the presence of lateral conduction. In ASME Turbo Expo 2003, collocated with the 2003 International Joint Power Generation Conference (pp. 297-310). American Society of Mechanical Engineers.
- [1.21] Lin, M. and Wang, T., 2002. A transient liquid crystal method using a 3-D inverse transient conduction scheme. *International journal of heat and mass transfer*, 45(17), pp.3491-3501.

- [1.22] Ryley, J.C., McGilvray, M. and Gillespie, D.R.H., 2014, June. Calculation of heat transfer coefficient distribution on 3D geometries from transient liquid crystal experiments. In ASME Turbo Expo 2014: Turbine Technical Conference and Exposition (pp. V05BT14A019-V05BT14A019). American Society of Mechanical Engineers.
- [1.23] Nirmalan, N.V., Bunker, R.S. and Hedlung, C.R., 2002, January. The measurement of full-surface internal heat transfer coefficients for turbine airfoils using a non-destructive thermal inertia technique. In ASME Turbo Expo 2002: Power for Land, Sea, and Air (pp. 365-372). American Society of Mechanical Engineers.
- [1.24] Brack, S., Poser, R. and von Wolfersdorf, J., 2016. An approach to consider lateral heat conduction effects in the evaluation process of transient heat transfer measurements using TLC. *International Journal of Thermal Sciences*, 107, pp.289-302
- [1.25] Zuckerman, N. and Lior, N., 2006. Jet impingement heat transfer: physics, correlations, and numerical modeling. *Advances in heat transfer*, 39, pp.565-631.
- [1.26] Kercher, D.M. and Tabakoff, W., 1970. Heat transfer by a square array of round air jets impinging perpendicular to a flat surface including the effect of spent air. *Journal of Engineering for power*, 92(1), pp.73-82.
- [1.27] Kim, K. and Feng, S.S., 2016. Thermal Mapping Using Infrared Thermography. In *Application of Thermo-Fluidic Measurement Techniques* (pp. 215-250). Butterworth-Heinemann
- [1.28] Yan, Y. and Owen, J.M., 2002. Uncertainties in transient heat transfer measurements with liquid crystal. *International Journal of Heat and Fluid Flow*, 23(1), pp.29-35.

- [1.29] Singh, P. and Ekkad, S.V., 2017. Effects of spent air removal scheme on internal-side heat transfer in an impingement-effusion system at low jet-to-target plate spacing. *International Journal of Heat and Mass Transfer*, 108, pp.998-1010.
- [1.30] Ekkad, S.V. and Han, J.C., 2000. A transient liquid crystal thermography technique for gas turbine heat transfer measurements. *Measurement Science and Technology*, 11(7), p.957.
- [1.31] Singh, P. and Ekkad, S., 2017. Experimental study of heat transfer augmentation in a two-pass channel featuring V-shaped ribs and cylindrical dimples. *Applied Thermal Engineering*, 116, pp.205-216.
- [1.32] Singh, P., Pandit, J. and Ekkad, S.V., 2017. Characterization of heat transfer enhancement and frictional losses in a two-pass square duct featuring unique combinations of rib turbulators and cylindrical dimples. *International Journal of Heat and Mass Transfer*, 106, pp.629-647.
- [1.33] Singh, P., Ravi, B.V. and Ekkad, S.V., 2016. Experimental and numerical study of heat transfer due to developing flow in a two-pass rib roughened square duct. *International Journal of Heat and Mass Transfer*, 102, pp.1245-1256.
- [1.34] Singh, P., Li, W., Ekkad, S.V. and Ren, J., 2017. A new cooling design for rib roughened two-pass channel having positive effects of rotation on heat transfer enhancement on both pressure and suction side internal walls of a gas turbine blade. *International Journal of Heat and Mass Transfer*, 115, pp.6-20.
- [1.35] Singh, P., Li, W., Ekkad, S.V. and Ren, J., 2017. Experimental and numerical investigation of heat transfer inside two-pass rib roughened duct ($AR=1:2$) under rotating and stationary conditions. *International Journal of Heat and Mass Transfer*, 113, pp.384-398.

- [1.36] D. W. Peaceman and H. H. Rachford, Jr., "The numerical solution of parabolic and elliptic differential equations," *J. Soc. Ind. Appl. Math.*, vol. 3, pp. 28–41, 1955
- [1.37] J. Douglas, Jr. and J. E. Gunn, "A general formulation of alternating direction methods—Part I: Parabolic and hyperbolic problems," *Numer. Math.*, vol. 6, pp. 428–453, 1964.
- [1.38] Goldstein, R.J. and Behbahani, A.I., 1982. Impingement of a circular jet with and without cross flow. *International Journal of Heat and Mass Transfer*, 25(9), pp.1377-1382.
- [1.39] Hollworth, B.R. and Gero, L.R., 1985. Entrainment effects on impingement heat transfer: part II—local heat transfer measurements. *Journal of Heat Transfer*, 107(4), pp.910-915.
- [1.40] Florschuetz, L.W., Berry, R.A. and Metzger, D.E., 1980. Periodic streamwise variations of heat transfer coefficients for inline and staggered arrays of circular jets with crossflow of spent air. *Journal of Heat Transfer*, 102(1), pp.132-137.

CHAPTER 2

HEAT TRANSFER IN AN INDUSTRIAL LOW NOX SWIRL STABILIZED CAN COMBUSTOR: ASSESSMENT OF HYBRID RANS-LES METHODS

2.1. ABSTRACT

While the gas turbine research community is pursuing higher efficiency by increasing the combustor temperatures, a simultaneous effort to reduce the NO_x emission level also needs to be considered. There has been a significant push towards developing lean premixed combustion technologies to address this objective in recent times. In this study, the unsteady isothermal fluid dynamics and related heat transfer on liner walls generated by a low emission, low-NO_x lean premixed, industrial fuel swirl nozzle designed by Solar Turbines Incorporated have been numerically investigated. This study compares the performance of the Reynolds Averaged Navier Stokes (RANS) approach and Hybrid Reynolds Averaged Navier Stokes – Large Eddy Simulation (RANS-LES) in computing the flow field and heat transfer generated by an industrial swirler within a can combustor. The RANS Model and three different hybrid RANS-LES models, Scale Adaptive Simulation (SAS), Detached Eddy Simulation (DES), and Wall Modeled Large Eddy Simulation (WMLES) models, were compared in this study. Numerical data obtained were compared to data obtained using an in-house experimental combustor rig. The numerical simulation was carried out in a two-step process with synthetic inlet turbulence to reduce computational cost in resolving the flow through the swirler. The results showed essential flow features in swirl-based combustors such as corner recirculation zones, inner recirculation zone (IRZ), shear layers, and the precessing vortex core (PVC), and its associated effect on the heat transfer has been identified. All the hybrid RANS-LES models provided good agreement with the Particle Image Velocimetry (PIV) experimental measurements regarding the opening angle,

impingement location, and internal recirculation zone size compared to the RANS Model. The assessment in terms of liner wall heat transfer confirms the Hybrid RANS-LES models' overall accuracy, which showed good agreement with the experimental PIV and heat transfer results. The WMLES model performed the best compared to the other hybrid RANS-LES models and represents a starting point for further investigations that consider the presence of effusion cooling.

2.2. INTRODUCTION

Combustor designs for both land-based and propulsion-based gas turbine engines are advancing and pushing their operating limits. Higher efficiency and improved durability are the main factors affecting the design of combustors. In addition to improving durability, there is also a requirement to reduce pollutant formation in gas turbine combustors. The Environmental Protection Agency (EPA) in the United States limits NO_x emissions of new stationary gas turbines firing natural gas to 15 ppm at 15% O_2 for installations over 250 MW [2.1], making pollutant management a crucial part of combustor chamber design. One of the widely used techniques to reduce pollutant formation is to use Lean Premixed Combustion (LPM).

In the lean premixed combustion technique, a significant amount of air is premixed with the incoming fuel entering through an industry-specific fuel nozzle (with swirl imparting vanes) and burn under lean conditions to improve power. With the increase in air and fuel premixing, there is a significant reduction in the air available for combustor chamber cooling. Hence for LPM combustors, it becomes crucial to characterize the flow field and heat transfer characteristics on the liner to identify localized high heat load regions and, accordingly, design optimized cooling strategies to improve combustor life.

Lean premixed combustor flow involves coupled interactions between several physical phenomena such as degree of swirl, premixing of the fuel and the air, interaction of swirling flow with combustion driven heat release, flame extinction, etc. A typical lean premixed low NOX gas turbine combustor consists of an upstream axial or radial swirler followed by a combustor section and a transition piece connecting to the turbine inlet. The swirler is the most critical aspect of a gas turbine combustor as the swirling flow plays a vital role in stabilizing the flame and in lean combustion. A detailed description of swirling flow on combustion is given by Gupta et al. [2.2], Syred and Beer [2.3], and Lilley [2.4]. All swirling flows have three essential features: a central recirculation zone (CRZ), the precessing vortex core (PVC), and expansion-induced shear layers [3]. These features have been shown in Fig. 2.1. The CRZ recycles the hot combustion products back to the swirling jet from the nozzle. The CRZ is dominated by critical coherent structures that enhance the mixing between the fresh mixture and recirculated gases. Understanding these features is very crucial for flame location, mixing within the burner, and flame stability.

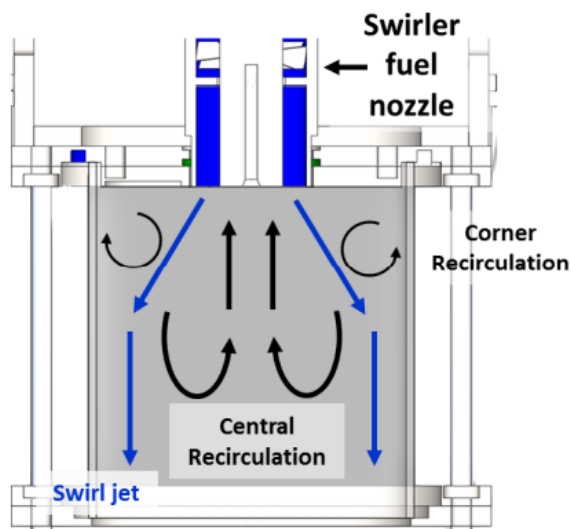


Figure 2.1 Swirl flow in a can combustor

In the past, several researchers have used techniques like LDV, PIV, hot wire anemometry, etc. to characterize the combustor flow and observe the flow features [2.5-2.9]. Several researchers have numerically investigated isothermal flow studies in the combustor based on the RANS model in the past. Wurm et al. [2.10] used RANS calculation to estimate the flow field in a modern lean combustor chamber. Farhad et al. [2.11] carried out studies to validate computed flow profiles at various sections inside the combustor domain and found reasonable agreement with experiments. Bailey et al. [2.12] found good agreement with experimental heat transfer when using a RANS-based model with enhanced wall functions.

Due to the RANS models' inherent limitations to overcome globally unsteady flows, LES and Hybrid RANS-LES models are becoming more popular in predicting flow field and heat transfer in a combustion chamber. One of the first studies to incorporate hybrid RANS-LES models to simulate non-reacting flow in a gas turbine combustor was by Widenhorn et al. [2.13]. The authors compared SST-SAS and SST-DES models' performance for predicting the non-reactive flow through a combustion chamber. The authors reported that for a more refined mesh SST-DES, showed an excellent agreement with experimental data, whereas, for a coarse mesh, SST-SAS provided more accurate results. Patil and Tafti [2.14] conducted wall modeled large-eddy simulations to investigate the flow and associated heat transfer in a gas turbine can combustor under cold flow conditions. They showed that WMLES predictions could simulate the flow field and capture the heat transfer trends closely with the experimental data. Grinstein and Fureby [2.15] compared LES results for non-reacting and reacting flow through a low NO_x combustor and obtained good agreement with experimental measurements. Mazzei et al. [2.16] investigated the impact of swirl flow on liner heat transfer using RANS, and hybrid RANS-LES approaches. The authors concluded that the SAS model provided the best trade-off between experimental accuracy

and computational cost while suggesting more advanced formulations such as DDES and IDDES. Andreini et al. [2.17-2.18] have conducted several investigations to model the flow field and heat transfer in realistic combustor geometries using hybrid RANS – LES models. Some other investigations on the application of RANS and hybrid RANS-LES models to predict flow and heat transfer in gas turbine combustors can be found in Liu et al. [2.19], Xia et al. [2.20], West et al. [2.21], and Frezzotti et al. [2.22].

In the present numerical study, the combustor flow profiles (downstream of swirler) were compared for various RANS and Hybrid RANS-LES models to study their impact on predicting flow profiles and crucially heat transfer on the combustor walls. To the authors' knowledge, this is the first attempt to compare the performance of different hybrid RANS-LES methods in predicting the velocity profiles and heat transfer generated by industrial swirler. The study also hopes to validate the synthetic inlet turbulence methodology from hybrid RANS-LES models to predict the swirl-driven flow and heat transfer. This process has been shown to have good agreement with experimental data [2.23]. The RANS data of Gomez-Ramirez et al. [2.24 - 2.26] and Kedukodi et al. [2.27-2.28], validated against experimental data, provide inflow conditions for simulations in the study. This paper is a precursor study to future computational studies involving full-coverage film cooling or effusion cooling for the can combustor. Effusion cooling consists of several film cooling holes distributed throughout the combustor surface area. In these cases, the study of effusion cooling becomes computationally expensive due to the stringent mesh requirements in the cooling holes and the swirler region. In such cases, the synthetic inlet methodology will decrease the mesh count and will make the optimization studies on combustor liners feasible. The data obtained in this study aims to aid designers of gas turbine components and

the development and validation of numerical codes for accurate prediction of heat transfer performance of such features.

2.3. DESCRIPTION OF EXPERIMENTAL SETUP

A brief overview of the rig setup and the experimental procedure has been presented in this study. For more information, the reader is referred to Gomez-Ramirez et al. [2.25]. A portion of the testing facility is shown in Fig. 2.2. The flow metering into the test section was carried out upstream of the main control valve using a turbine flow meter, coupled with downstream pressure and temperature measurements. A pressure-reducing regulator was used to lower the pressure to the required operating conditions, and the main control valve was used to control the flow into the test section. An inline 192 kW heater was also installed in the experimental rig but was not used for the current experiment.

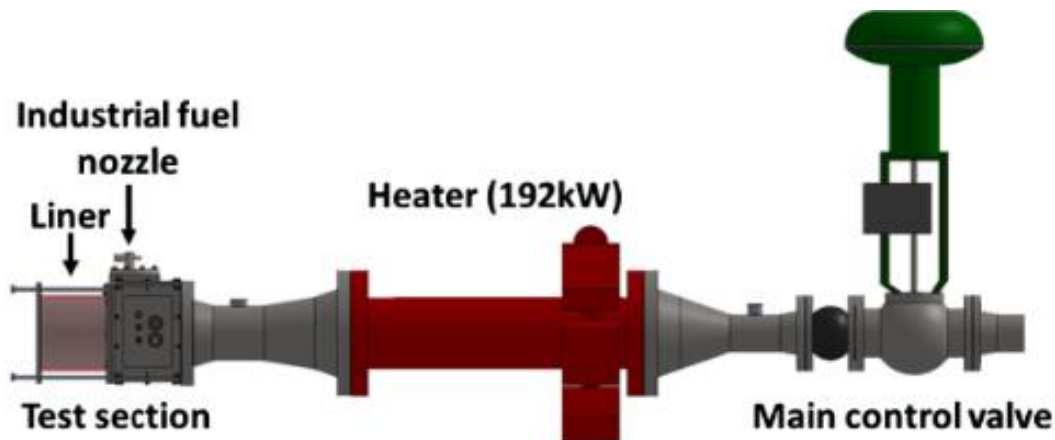


Figure 2.2 Experimental facility

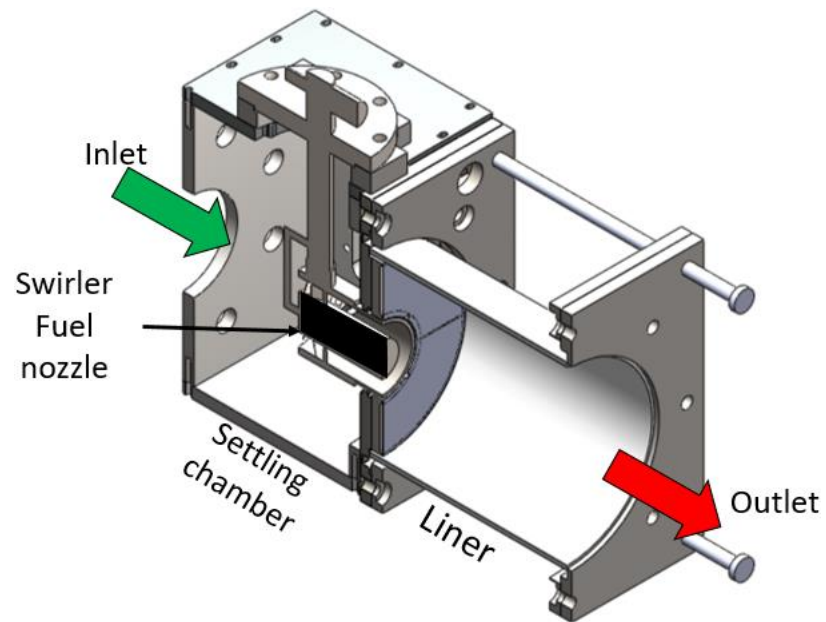


Figure 2.3 Schematic of the test section

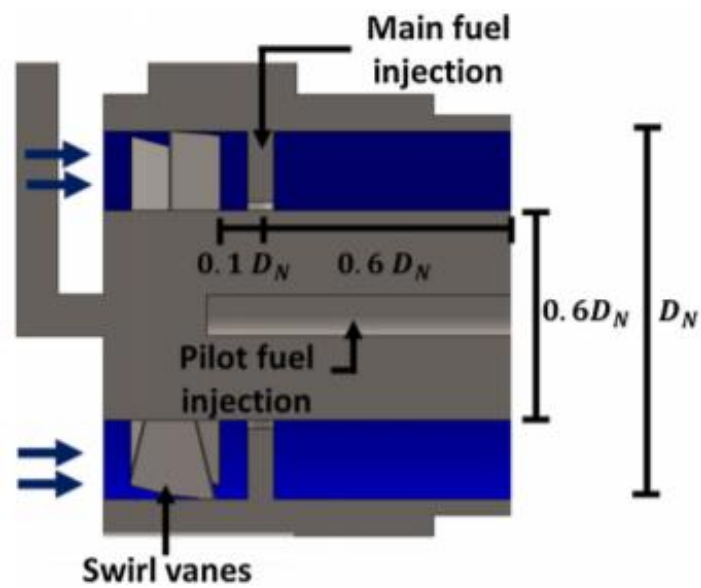


Figure 2.4 Schematic of the swirler used

As shown in Fig. 2.2 the test section houses an industrial low emissions swirl fuel nozzle. The nozzle consists of axial swirl vanes followed by fuel injectors downstream of the flow that introduces fuel into the premixing channel. The liner consists of a quartz tube 4mm thick, with an internal diameter of 203mm and a length of 216mm. The combustor's primary zone was designed to be as simple as possible to aid in the validation of numerical models. As the experiments described in this paper were run at non-reacting conditions, no fuel was injected through the primary or pilot fuel lines.

2.3.1. Experimental Setup for PIV Experiments

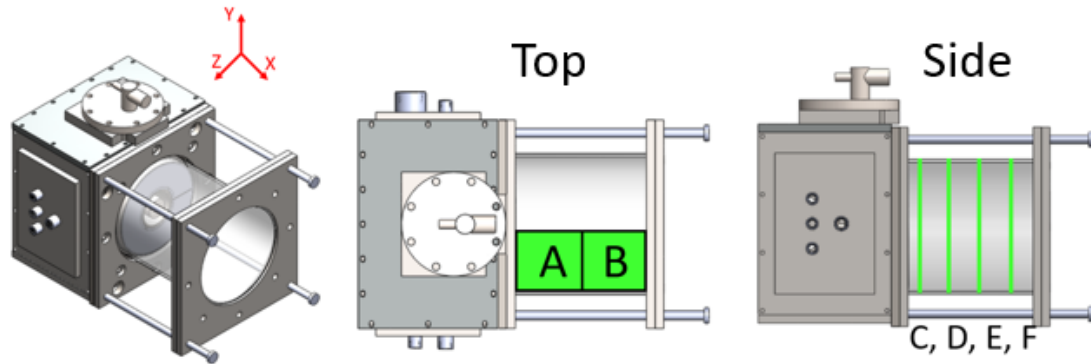


Figure 2.5 PIV Planes

Two-dimensional planar Particle Image Velocimetry (PIV) measurements were taken at the planes indicated in Fig. 2.5. Planes A-B is referred to as axial planes (XZ planes) and planes C-G are referred to as cross-sectional, radial-tangential, or azimuthal planes (ZY planes). Planes C-F was located at $X/D_N = 0.16, 0.91, 1.54,$ and 2.4 respectively. The measurements were performed using a Nano-L 135-15 dual Nd: YAG laser system (5 mm laser sheet thickness), with

a Flowsense 4 M MkII camera (2048 X 2048 pixel resolution), and Dantec Dynamics acquisition software. Glycol droplets were seeded into the settling chamber upstream of the swirl nozzle to act as tracers for the PIV measurement

2.3.2. Experimental Setup for Heat Transfer Experiments

To measure the heat transfer along the quartz liner, A thin surface heater (0.3 mm thick Polyimide Thermofoil™) was attached to the inner wall of the providing a constant and uniform wall heat input(Q_w). The heater provided a constant and uniform wall heat input, and the wall heat input was determined from the heater's electrical resistance and the voltage supplied. The steady-state(60 min) inner wall temperatures (T_w) were derived from IR measurements using a FLIR SC6700 camera. A schematic of the heater placement on the liner is shown in Fig. 2.3. During the experiment, air at ambient conditions was supplied to the test setup, and the heater power was adjusted to achieve the maximum allowable temperature at the given airflow.

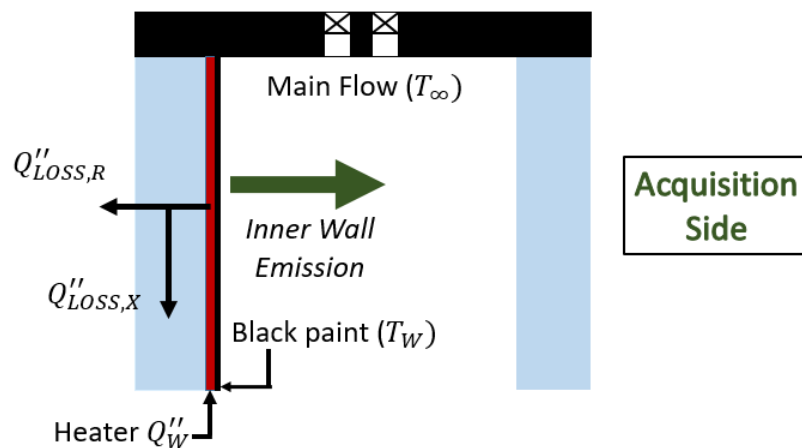


Figure 2.6 Infrared Thermography (IR) Setup

The heat transfer coefficient (HTC), h , along the combustor liner wall was determined from Eq.(3)

$$h = \frac{Q''_W - Q''_{LOSS}}{T_W - T_\infty} \text{ (Eq. 2.1)}$$

where the wall temperature, T_W , was calculated from the IR acquisitions, Q''_W , was the heat flux applied to the surface, T_∞ was the airflow temperature, Q''_{LOSS} was the heat flux lost to conduction. T_W was estimated from the average of two thermocouples, one immediately at the fuel nozzle outlet and another at the outlet of the combustor.

2.4. NUMERICAL METHODOLOGY AND SETUP

2.4.1. Numerical Setup

Three-dimensional steady-state incompressible Reynolds-averaged Navier–Stokes equation was solved using finite-volume-based solver ANSYS FLUENT 18.2 (academic license). Fluid in this study has been modeled as an incompressible fluid with constant properties. For the spatial discretization, second-order discretization was used for pressure, bounded central differencing for momentum, second-order upwind for energy, and bounded second-order implicit formulation was used for the transient formulation. The convergence criterion for continuity, x-velocity, y-velocity, z-velocity, and turbulence parameters in this study was set to 10^{-5} and the convergence criterion for the energy equation was assigned to a lower value of 10^{-7} . The study's turbulence has been

modeled using RANS and three different hybrid RANS-LES techniques such as SAS, DES, and WMLES. More information about the turbulence has been presented in section 2.4.5.

For all the transient simulations, a time step of $1 * 10^{-5}$ s was used to ensure that the Courant number (Co) was lower than unity. The simulations were run for one non-dimensional time unit, and statistical data sampling was carried out for 0.5 non-dimensional time units. Average velocities and temperature data were monitored at various locations in the domain to verify that a stationary steady state was reached.

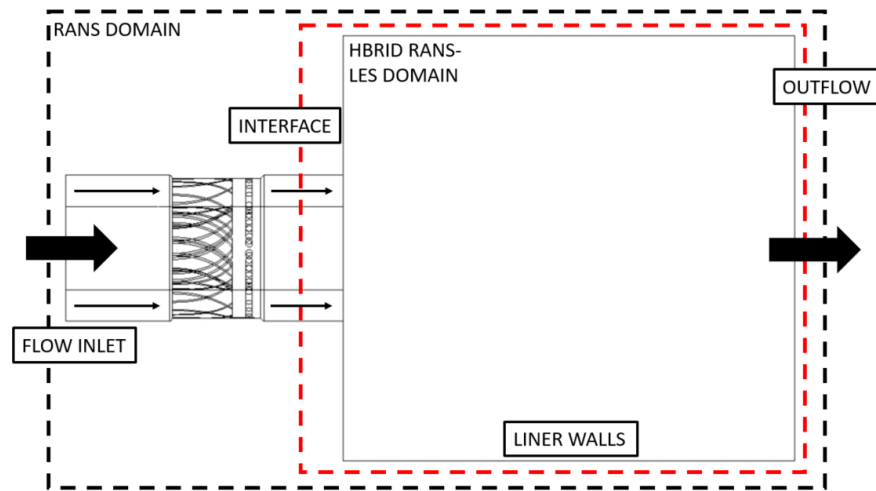


Figure 2.7 Domain Details

2.4.2. Methodology

Figure 6. shows the computational domain used in this study. In this case, there are two different computational domains. First is the computational domain used by Gomez-Ramirez et al. [2.24 - 2.26] and Kedukodi et al. [2.27-2.28] for the RANS calculation, which incorporates both the swirler and the downstream geometry, and the second computational domain which is used in

the current study. This method used in this study to simulate inlet turbulence in this study is known as the synthetic inlet turbulence method and is based on the work by Jarrin et al. The method generates synthetic eddies on the inlet plane, and a specific shape function represents each eddy. The synthetic eddy method uses randomly distributed eddies in an eddy container around the inlet plane with a velocity-shaped function associated with each eddy. Inlet turbulence is generated by taking the collective effect of all of the eddies on the velocity nodes in the inlet plane, conditioned by the available turbulent statistics, which, in this case, are obtained from the precursor RANS simulation. The net result is the generation of instantaneous turbulence, which is spatially and temporally correlated based on the integral length scales and the mean velocity profile from the RANS calculation. Jarrin et al. [2.23] has shown that the synthetic turbulence at the interface of a hybrid RANS-LES flow solver. The computational domain in this study consists of the can combustor and an inlet section that is $0.45D_N$ upstream of it.

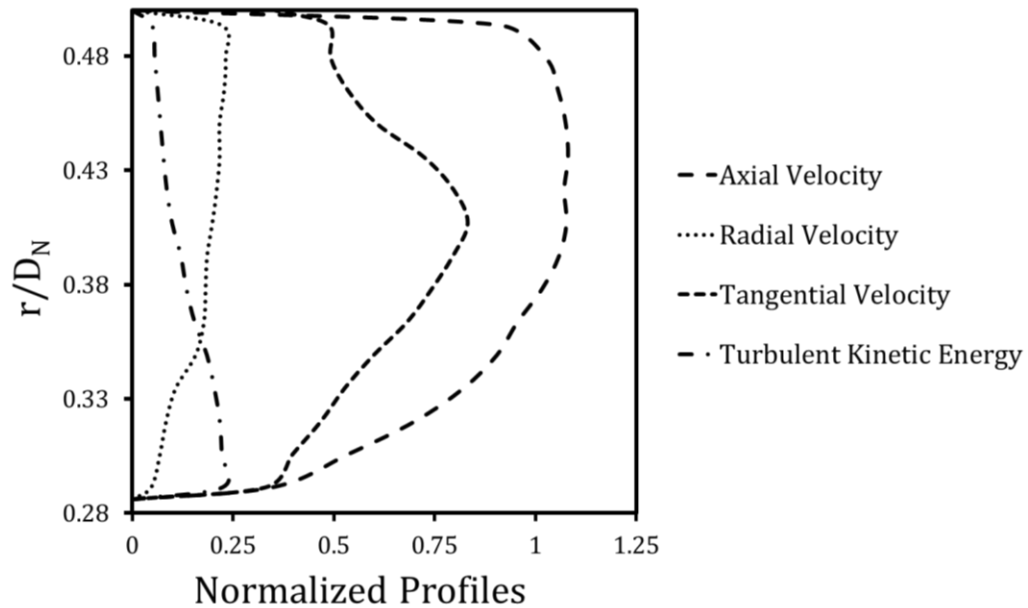


Figure 2.8 Normalized velocity profiles and turbulent kinetic energy

2.4.3. Inlet Flow Profiles

Three components of the mean velocity and turbulent kinetic energy are extracted from the RANS study Gomez-Ramirez et al. [2.24 - 2.26] and Kedukodi et al. [2.27-2.28]. Fig. 2.8 shows the three mean velocity components' profiles normalized by the bulk mean combustor velocity, and the turbulent kinetic energy is normalized by the square of the bulk mean combustor velocity.

2.4.4. Boundary Conditions

Figure 2.7 shows the boundary conditions that have been used in this study. For the study, the interface location was assigned as inlet velocity boundary conditions at $300^{\circ}K$. All the walls were treated as smooth, no-slip, adiabatic walls except for the liner wall, to which a constant heat flux of 5000 W/m^2K was applied. Outflow condition was used at the outlet of the combustor.

2.4.5. Turbulence Modelling

i. The Scale Adaptive Simulation.

The Scale-Adaptive Simulation (SAS) is an improved URANS formulation, which allows the resolution of the turbulent spectrum in unstable flow conditions. The SAS model provides RANS-like simulation in low instability areas and provides LES quality results in unsteady regions of the domain. The SAS concept is based on the introduction of the von Karman length-scale into the turbulence scale equation.

The information provided by the von Karman length-scale allows SAS models to dynamically adjust to resolved structures in a URANS simulation, which results in an LES-like behavior in unsteady turbulent regions of the flow field [2.29]. At the same time, the model provides standard RANS capabilities in stable flow regions. One of the significant difficulties

associated with the hybrid RANS-LES models is switching between the RANS model and LES mode. In the near-wall area, the model should select the RANS model. However, when the mesh is too fine in the near-wall region, the LES approach may lead to flow separation. This phenomenon is known as Grid Induced Separation (GIS) and is a significant drawback in Hybrid RANS-LES methods. The SAS method overcomes this issue by not incorporating an explicit dependence on the grid to the turbulence model. In this study, the SAS-SST model as available in Fluent 18.2 was used.

ii. Detached Eddy Simulations (DES):

In the Detached Eddy Simulation (DES) approach, the unsteady RANS models are employed in the boundary layer, while the LES treatment is applied to the separated regions. In this study, the Improved Delayed Detached Eddy Simulation model in Fluent 18.2 was used. The IDDES model is a hybrid RANS-LES model that provides a convenient scale-resolving simulation model for high Reynolds number flows. The IDDES model incorporates a shielding against grid-induced shielding. More information about the IDDES model can be found in Shur et al. [2.30]

iii. Wall Modelled LES (WMLES):

While the LES model is commonly used in the academic community, its use in industrial applications is limited due to the high grid resolution requirement for wall boundary regions. One common approach to overcome the high grid resolution requirement is to use the algebraic wall modeled large eddy simulation (WMLES). In WMLES, the RANS mode is activated in the inner part of the boundary layer, and the rest of the domain is modeled using the LES model. In the study, the WMLES proposed by Shur et al. [2.31] as available in Fluent 18.2 has been studied.

In the Shur et al. [2.31] model, the eddy viscosity is calculated with the use of a hybrid length scale as,

$$\nu_t = \min \left[(\kappa d_w)^2, (C_{smag} \Delta)^2 \right] \cdot S \cdot \left\{ 1 - \exp \left(- \left(\frac{y^+}{25} \right)^3 \right) \right\} \quad (Eq. 2.4)$$

Where d_w is the wall distance, S is the strain rate, $\kappa = 0.41$ and $C_{smag} = 0.2$ are constants and y^+ is normal to wall scaling. To overcome issues with grid induced separation, the WMLES model uses a modified grid-scale given by,

$$\Delta = \min (\max(C_w * d_w; C_w * h_{\max}, h_{wn}); h_{\max}) \quad (Eq. 2.5)$$

Here h_{\max} is the maximum edge length of the cell, h_{wn} is the wall-normal grid spacing, and $C_w = 0.15$ is a constant.

2.4.6. Grid Generation

ANSYS ICEM-CFD and ANSYS mesh were used to create hexahedral grids for all the simulations with inflation layers close to the boundaries to capture the near-wall flow physics. The inflation layers ensured that the Y^+ values on the combustor liner wall were below 1 for the computations in this study. The features of the computational domain used for this study have been shown in table 1. The meshing criteria used are based on the recommendations made by the code developers for scale resolved simulations [2.32].

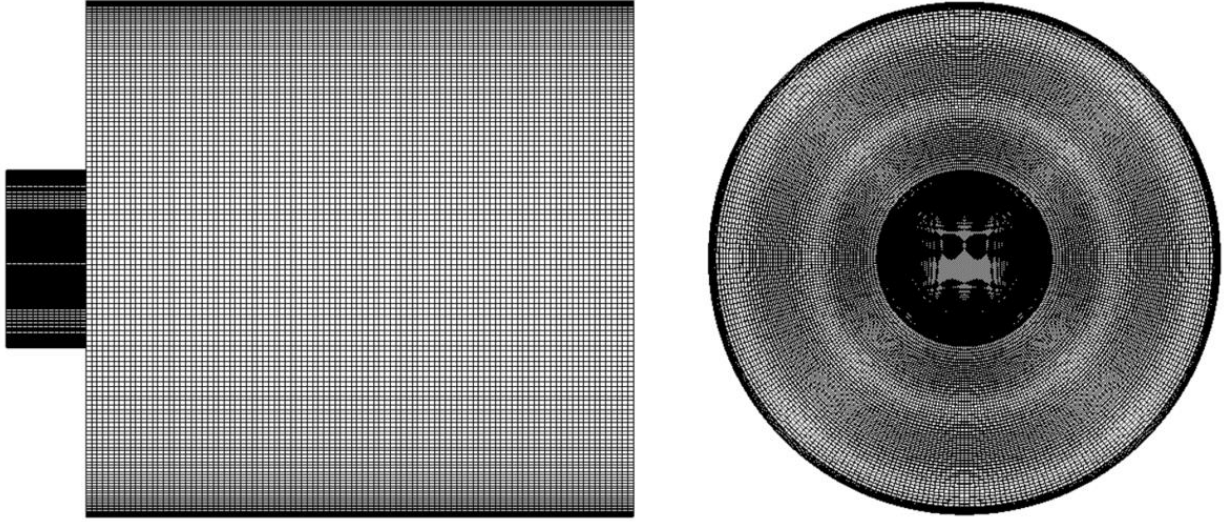


Figure 2.9 Computational mesh used in study

To evaluate the quality of the hybrid RANS-LES calculations in this study, the pope criterion was used. The pope criterion is defined as,

$$M = \frac{K^{res}}{K + K^{res}} \text{ (Eq. 2.6)}$$

Where K is the resolved turbulent kinetic energy and K^{res} is the turbulent kinetic energy captured by the turbulence model. $M=0$ corresponds to a fully resolved simulation, whereas $M=1$ corresponds to a simulation in which the turbulence is fully modeled.

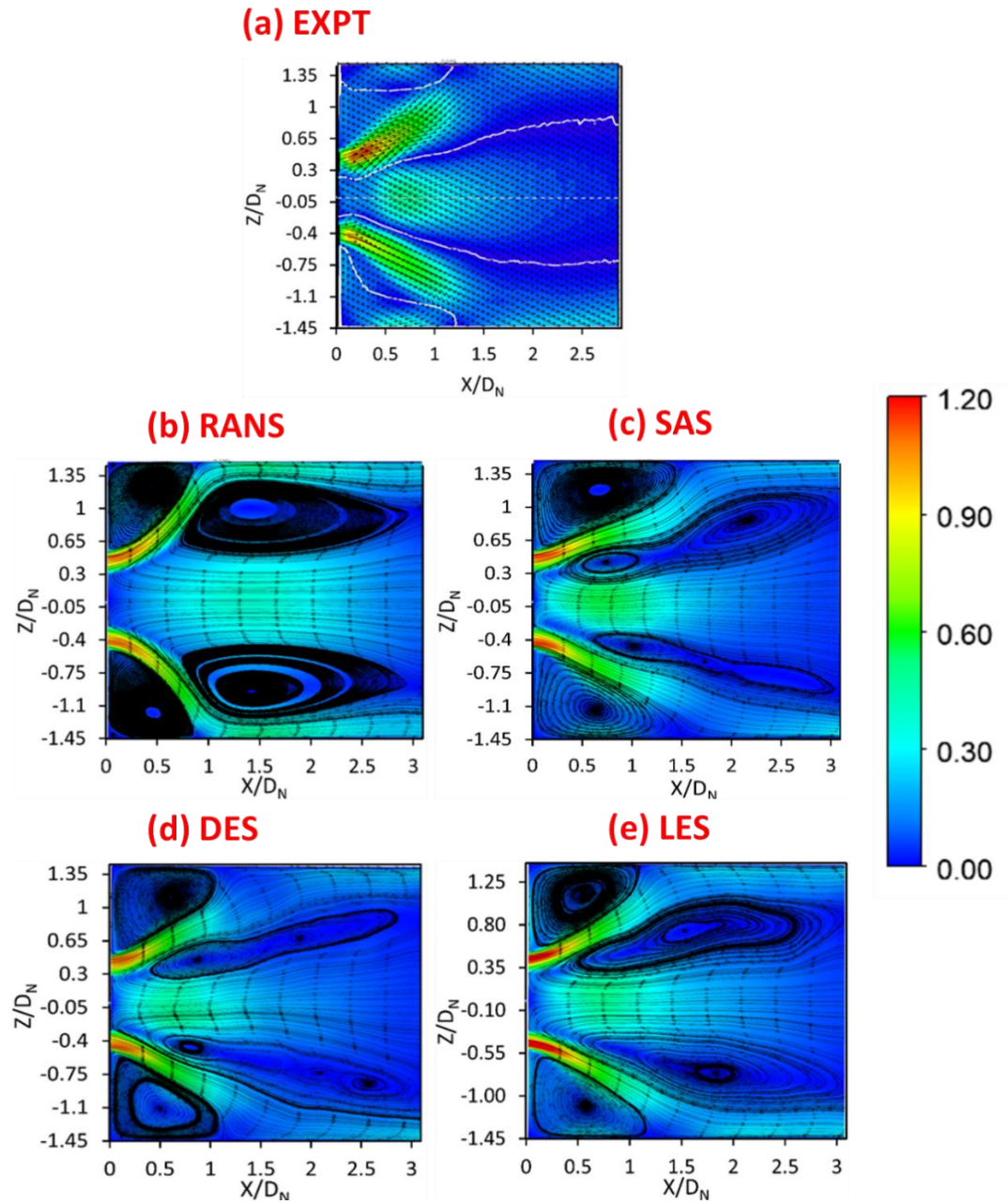


Figure 2.10 Velocity Contours on Plane A superimposed with velocity streamlines

2.5. RESULTS AND DISCUSSION

2.5.1. Time averaged results

Fig. 2.11 represents the comparison of the time-averaged velocity magnitude generated by the swirler on a central plane A corresponding to a Reynolds number of 50,000 based on the swirler outer diameter. The experimental data obtained using the PIV measurements on plane A were compared to those observed using the different turbulence models. The experimental data has been superimposed with velocity vectors, whereas the CFD contours have been superimposed with velocity streamlines. The main features of swirl flow, such as the corner recirculation zone and central recirculation zones, are observed in the figure. The swirler generates swirling flow which expands from the swirler nozzle annulus to the combustor geometry. This swirling flow impinges on the liner wall at X/D_N of 1.3. After impingement, the flow attaches the flow and forms the wall jet region. This expansion and subsequent flow attachment lead to crucial swirl flow features such as the corner recirculation zone (CRZ), shear layers, and the vortex breakdown-induced central recirculation zone(CRZ).

From comparing the CFD simulation with the experimental data, we notice the significant issues with modeling the flow within the combustor using the RANS model. The RANS models underpredict the expansion angle of the swirling jet. Due to the RANS model predicts the impingement region to be around $\frac{X}{D_N} = 1$. Also, due to the RANS model's inability to predict the unsteadiness, the RANS model overestimates the size of the central and corner recirculation zone. The hybrid RANS-LES models predict the combustor flow to a sufficiently accurate degree with some minor discrepancies, with the WMLES providing the best match with experimental data. The WMLES model accurately predicts the point of impingement and the size of the corner

recirculation zones. All the CFD models tend to overpredict the central recirculation zone's size compared to the experimental data.

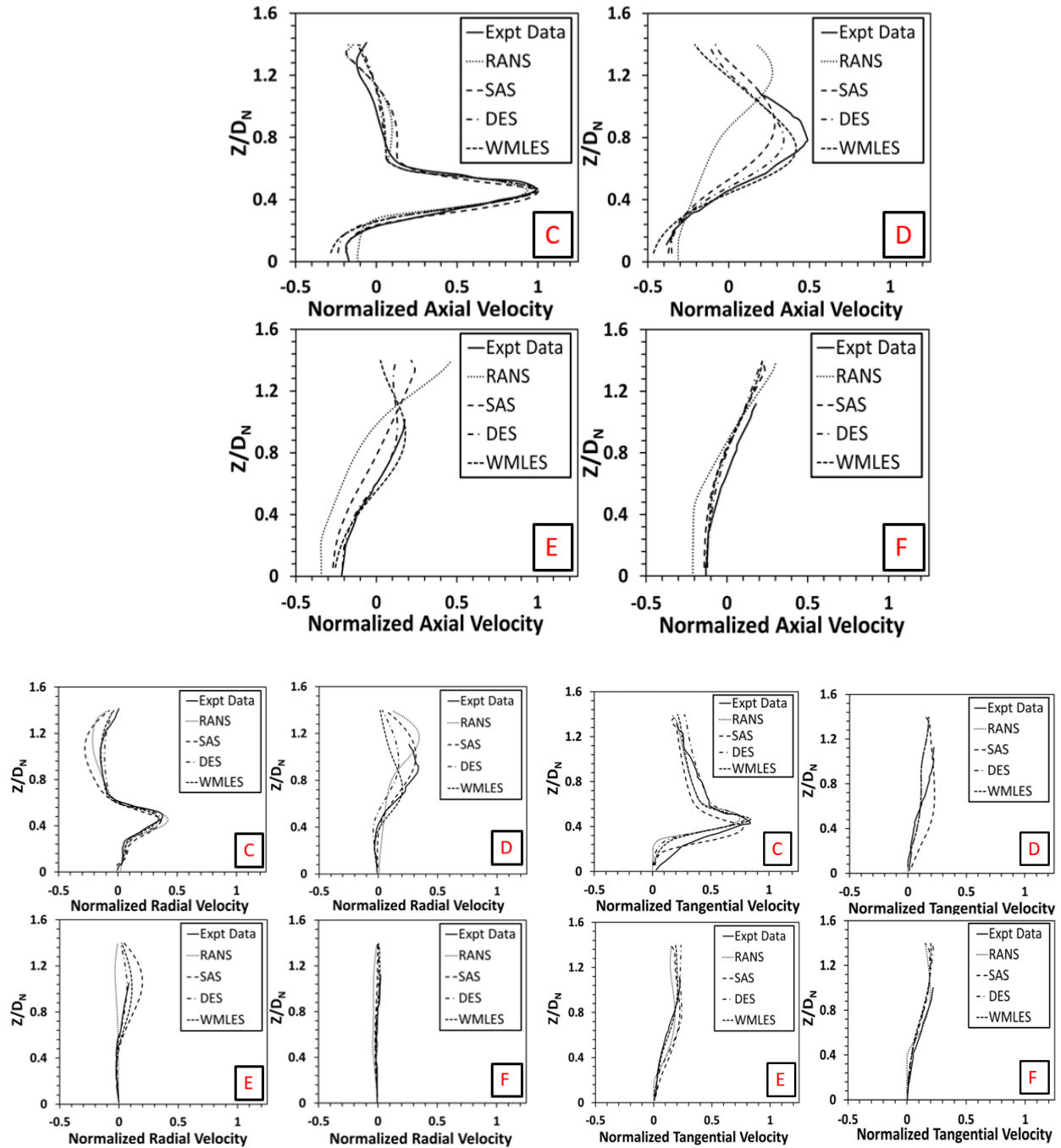


Figure 2.11 Radially averaged non-dimensional (a) Axial Velocity (b) Radial Velocity (c) Tangential Velocity

Experimental data close to the dump plane is affected by the combustor dump plane's reflection, which affects the measurements near the dump plane. The SAS and DES models overpredict the opening angle by a slight degree, leading to slightly lower velocities in the wall jet region than the WMLES and the experimental data. This can be attributed to the fact that both the SAS and DES model use wall blending functions to transition from the LES regions away from the walls to the RANS treatment close to walls that cannot correctly model the flow with this region. The different flow features have been quantified in the velocity magnitude and axial velocity contour plots given in the figure below.

The axial, radial and tangential velocity at four different places were compared to quantify the difference between experimental data and the simulation data. The four planes have been selected such that they represent the other regions of flow within the combustor. Place C is very close to the dump plane, Plane F is very close to the exit of the combustor, and Plane D and Plane E represent planes on either side of the flow impingement. As the flow exits the swirling annulus at Plane C, all the CFD models predict the velocity magnitudes accurately. As the swirling jet impinges on the liner wall, at Plane D, there is a significant deviation between the CFD models. As this region is dominated by the flow instability of the corner and central recirculation zones, the RANS model fails at predicting the velocity profiles at Plane C and Plane D. The hybrid RANS-LES models perform better with the WMLES model predicting normalized velocities close to experimental values at all the four planes.

2.5.2. Time varying results

The PVC, highlighted by a constant pressure isosurface, generates a strong unsteadiness and enhances the mixing in the shear layer between the swirling flow and the low velocity air of the IRZ.

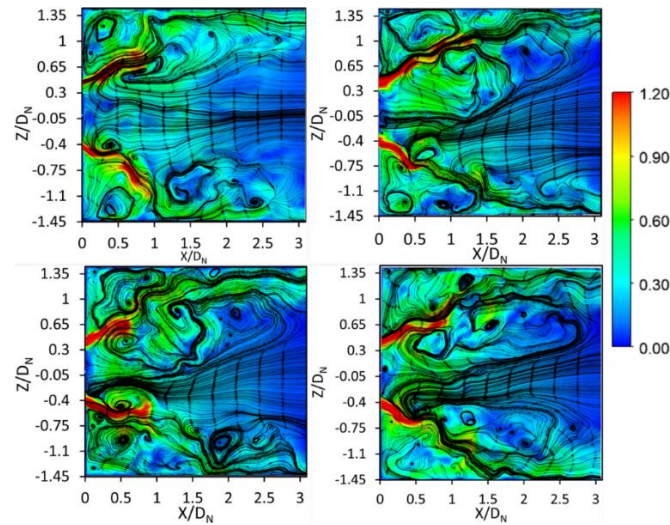


Figure 2.12 Time dependent velocity contour on the center plane

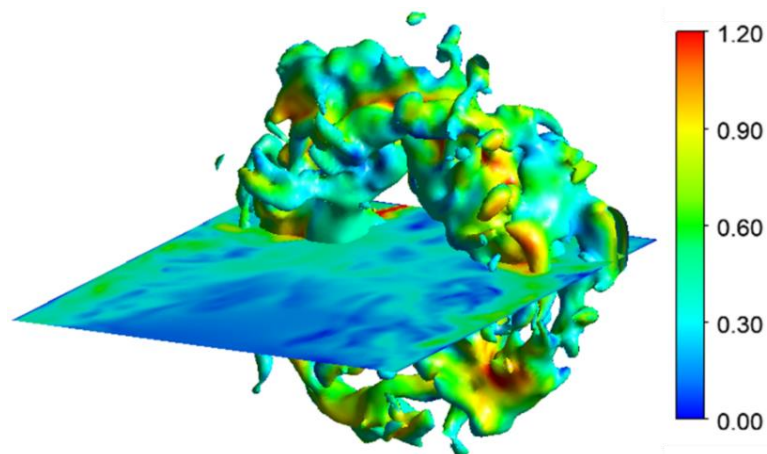


Figure 2.13 Velocity contour on the center plane with PVC visualized by constant pressure isosurface

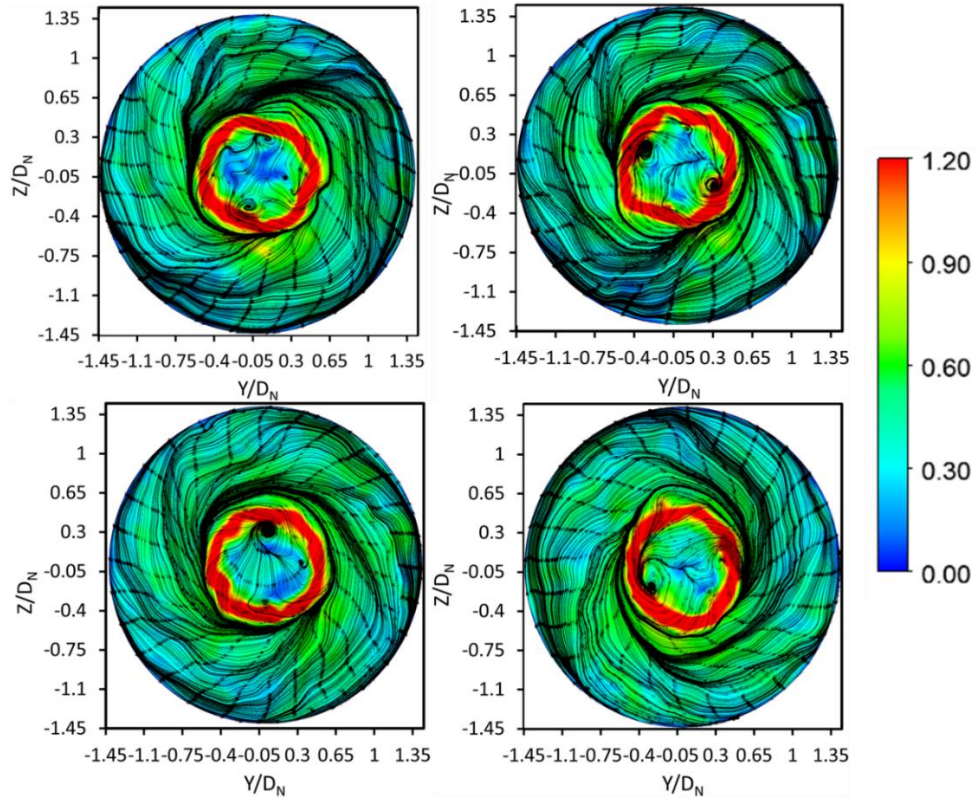


Figure 2.14 Time dependent velocity contour on Plane C

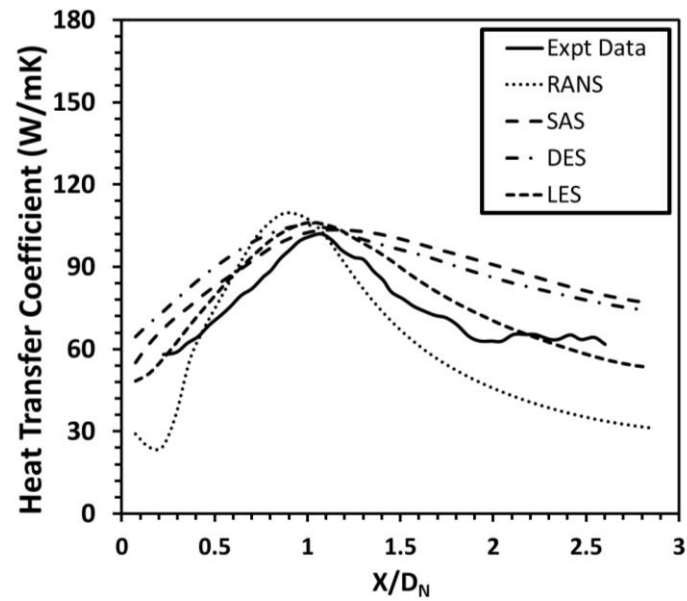


Figure 2.15 Heat Transfer Coefficient

2.5.3. Heat Transfer results

The circumferentially averaged heat transfer coefficients have been shown in Fig. 2.15. The velocity effects have a direct impact on the resulting heat transfer estimation: the HTC distribution obtained with the WMLES agrees very well, especially the location of the peak, where the error lies below the experimental uncertainty, whereas the SAS and DES runs constantly overpredicts the magnitude of the heat transfer.

2.6. CONCLUSIONS

A numerical investigation was carried out in order to evaluate the capability of hybrid RANS-LES models in predicting the flow field and heat transfer in a swirl stabilized can combustor. The flow field analysis has highlighted the potential issues of the RANS approach in simulating swirling flow in combustors. The WMLES model shows the best agreement with PIV data, whereas DES returns a greater acceleration in the near-wall region downstream of the impingement region. These effects directly impact the resulting heat transfer estimation: the HTC distribution obtained with the WMLES agrees very well, especially the location of the peak, where the error lies below the experimental uncertainty, whereas the SAS and DES runs constantly overpredicts the magnitude of the heat transfer. Moreover, the promising results obtained with the WMLES model represent a starting point for further investigations that take into account the presence of effusion cooling.

NOMENCLATURE

<i>RANS</i>	Reynolds Averaged Navier Stokes
<i>LES</i>	Large Eddy Simulations
<i>SAS</i>	Scale Adaptive simulations
<i>DES</i>	Detached Eddy Simulation
<i>WMLES</i>	Wall Modeled Large Eddy Simulation
<i>IRZ</i>	Inner Recirculation Zone
<i>PVC</i>	Precessing Vortex Core
<i>PIV</i>	Particle Image Velocimetry
<i>LPM</i>	Lean Premixed Combustion
<i>CRZ</i>	Central Recirculation Zone
<i>SST</i>	Shear-Stress Transport
<i>Q</i>	Heat Input (W)
<i>IR</i>	Infrared Thermography
<i>T</i>	Temperature (K)
<i>Co</i>	Courant Number
<i>D_N</i>	Nozzle Diameter
<i>K</i>	Turbulent Kinetic Energy
<i>HTC</i>	Heat Transfer Coefficient
Sub scripts	
w	Wall
res	resolved

REFERENCES

- [2.1] Environmental Protection Agency (EPA), 2006, “40 CFR Part 60, Standards of Performance for Stationary Combustion Turbines; Final Rule,” Federal Register, 71:38482-38506. [2] Gupta AK, Lilley DG, Syred N. Swirl flows. London: Abacus Press; 1984.
- [2.2] Syred, N. and Beer, J.M., 1974. Combustion in swirling flows: a review. Combustion and flame, 23(2), pp.143-201.
- [2.3] Lilley, D.G., 1977. Swirl flows in combustion: a review. AIAA journal, 15(8), pp.1063-1078.
- [2.4] Strakey, P. A. and Yim, M. J., 2007, “Experimental and Numerical Investigation of a Swirl Stabilized Premixed Combustor Under Cold-Flow Conditions,” ASME J. Fluids Eng., 129, pp. 942–953.
- [2.5] Patil, S., Abraham, S., Tafti, D., Ekkad, S., Kim, Y., Dutta, P., Moon, H., and Srinivasan, R., 2011, “Experimental and Numerical Investigation of Convective Heat Transfer in Gas Turbine Can Combustor,” ASME J. Turbomach., 133(1), p. 011028.
- [2.6] Gouldin, F.C., Depsky, J.S. and Lee, S.L., 1985. Velocity field characteristics of a swirling flow combustor. AIAA journal, 23(1), pp.95-102.
- [2.7] Vu, B.T. and Gouldin, F.C., 1982. Flow measurements in a model swirl combustor. AIAA Journal, 20(5), pp.642-651.
- [2.8] Boehm, B., Dreizler, A., Gnirss, M., Tropea, C., Findeisen, J. and Schiffer, H.P., 2007, January. Experimental investigation of turbulence structure in a three-nozzle combustor. In Turbo Expo: Power for Land, Sea, and Air (Vol. 47918, pp. 55-64).
- [2.9] Martinelli, F., Olivani, A. and Coghe, A., 2007. Experimental analysis of the precessing vortex core in a free swirling jet. Experiments in Fluids, 42(6), pp.827-839.

- [2.10] Wurm BB, Schulz AA, Bauer HJ, Gerendas MM. Impact of Swirl Flow on the Cooling Performance of an Effusion Cooled Combustor Liner. ASME. Turbo Expo: Power for Land, Sea, and Air, Volume 4: Heat Transfer, Parts A and B ():1027-1039. doi:10.1115/GT2012-68972.
- [2.11] Farhad. D., Liu. N., 2005, Numerical Prediction of Non-reacting and Reacting Flow in a Model Gas Turbine Combustor, NASA Glenn Research Center, Cleveland, Ohio
- [2.12] Bailey, J. C., Intile, J., Fric, T. F., Tolpadi, A. K., Nirmalan, N. V., and Bunker, R. S., 2003, “Experimental and Numerical Study of Heat Transfer in a Gas Turbine Combustor Liner,” ASME J. Eng. Gas Turbines Power, 125, pp. 994–1002.
- [2.13] Widenhorn, A., Noll, B., and Aigner, M., 2009, “Numerical Study of a NonReacting Turbulent Flow in a Gas Turbine Model Combustor,” AIAA Paper No. 2009-647.
- [2.14] S. Patil, and D. Tafti, (2012), “Large Eddy Simulation of Flow and Heat Transfer in a Gas Turbine Can Combustor with Synthetic Inlet Turbulence,” Journal of Engineering for Gas Turbines and Power, 134(7), pp. 071503-071512
- [2.15] Grinstein, F. and Fureby, C., 2005, “LES Studies of the Flow in a Swirl Gas Turbine Combustor,” Proc. Combust. Inst., 30, pp. 1791–1798.
- [2.16] Mazzei L, Andreini A, Facchini B, Turrini F. Impact of Swirl Flow on Combustor Liner Heat Transfer and Cooling: A Numerical Investigation With Hybrid Reynolds-Averaged Navier–Stokes Large Eddy Simulation Models. ASME. J. Eng. Gas Turbines Power. 2015;138(5):051504-051504-10.
- [2.17] Andreini, A., Bacci, T., Insinna, M., Mazzei, L. and Salvadori, S., 2017. Hybrid RANS-LES modeling of the aerothermal field in an annular hot streak generator for the study of

- combustor-turbine interaction. *Journal of Engineering for Gas Turbines and Power*, 139(2).
- [2.18] Andreini, A., Facchini, B., Insinna, M., Mazzei, L. and Salvadori, S., 2015. Hybrid RANS-LES modeling of a hot streak generator oriented to the study of combustor-turbine interaction. In *ASME Turbo Expo 2015: Turbine Technical Conference and Exposition*. American Society of Mechanical Engineers Digital Collection.
- [2.19] Liu, Y., Tang, H., Tian, Z. and Zheng, H., 2015. CFD simulations of turbulent flows in a twin swirl combustor by RANS and hybrid RANS/LES methods. *Energy Procedia*, 66, pp.329-332.
- [2.20] Xia, G., Kalitzin, G., Lee, J., Medic, G. and Sharma, O., 2020, September. Hybrid RANS/LES Simulation of Combustor/Turbine Interactions. In *Turbo Expo: Power for Land, Sea, and Air* (Vol. 84072, p. V02BT33A013). American Society of Mechanical Engineers.
- [2.21] West, J., Groth, C.P. and Hu, J., 2015. Assessment of Hybrid RANS/LES methods for gas-turbine combustor-relevant turbulent flows. In *22nd AIAA Computational Fluid Dynamics Conference* (p. 2921).
- [2.22] Frezzotti, M.L., Nasuti, F., Huang, C., Merkle, C. and Anderson, W.E., 2015. Determination of heat release response function from 2D hybrid RANS-LES data for the CVRC combustor. In *51st AIAA/SAE/ASEE Joint Propulsion Conference* (p. 3841).
- [2.23] Jarrin, N., Benhamadouche, S., Laurence, D. and Prosser, R., 2006. A synthetic-eddy-method for generating inflow conditions for large-eddy simulations. *International Journal of Heat and Fluid Flow*, 27(4), pp.585-593.

- [2.24] Gomez Ramirez, D., 2016. Heat Transfer and Flow Measurements in an Atmospheric Lean Pre-Mixed Combustor (Doctoral dissertation, Virginia Tech).
- [2.25] Ramirez, D.G., Ekkad, S.V., Moon, H.K., Kim, Y., Srinivasan, R., “Isothermal coherent structures and turbulent flow produced by a gas turbine combustor lean pre-mixed swirl fuel nozzle”, *Experimental Thermal and Fluid Science*, Vol 81, (187-201), 2017
- [2.26] Gomez-Ramirez, D., Kedukodi, S., Ekkad, S.V., Moon, H.K.X., Kim, Y. and Srinivasan, R., 2017. Investigation of isothermal convective heat transfer in an optical combustor with a low-emissions swirl fuel nozzle. *Applied Thermal Engineering*, 114, pp.65-76.
- [2.27] Kedukodi, S., Gomez-Ramirez, D., Ekkad, S.V., Moon, H.K., Kim, Y. and Srinivasan, R., 2016, July. Analysis on Impact of Turbulence Parameters and Swirl Angle Variation on Isothermal Gas Turbine Combustor Flows. In *Heat Transfer Summer Conference* (Vol. 50336, p. V002T15A003). American Society of Mechanical Engineers.
- [2.28] Kedukodi, S., Park, S., Gadiraju, S., Ekkad, S., Kim, Y. and Srinivasan, R., 2017, June. Numerical and Experimental Investigations for Flow Fields Under Non-Reacting and Reacting Conditions Through a Lean Premixed Fuel Nozzle. In *Turbo Expo: Power for Land, Sea, and Air* (Vol. 50893, p. V05CT17A011). American Society of Mechanical Engineers.
- [2.29] F. Menter and Y. Egorov. The Scale-Adaptive Simulation Method for Unsteady Turbulent Flow Predictions. Part 1: Theory and Model Description. *Journal Flow Turbulence and Combustion*. 85. 113–138. 2010.
- [2.30] M. L. Shur, P. R. Spalart, M. K. Strelets, and A. K. Travin. "A Hybrid RANS-LES Approach With DelayedDES and Wall-Modelled LES Capabilities". *International Journal of Heat and Fluid Flow*. 29:6. December 2008. 1638-1649

- [2.31] M. L. Shur, M. K. Strelets, A. K. Travin and P. R. Spalart. "Turbulence Modeling in Rotating and Curved Channels: Assessing the Spalart-Shur Correction". AIAA Journal. 38(5). 2000. 2000.
- [2.32] Menter, F. R., 2012, "Best Practice: Scale-Resolving Simulations in ANSYS CFD," ANSYS Germany GmbH, Darmstadt, Germany.

CHAPTER 3

OVERALL COOLING EFFECTIVENESS OF EFFUSION COOLED CAN COMBUSTOR LINER UNDER REACTING AND NON-REACTING CONDITIONS

3.1. ABSTRACT

Emphasis on lean premixed combustion in modern low NOX combustion chambers limits the air available for cooling the combustion liner. Hence, the development of optimized liner cooling designs is imperative for effective usage of available coolant. An effective way to cool a gas turbine combustor liner is through effusion cooling. Effusion cooling (also known as full-coverage film cooling) involves uniformly spaced holes distributed throughout the liner's curved surface area. This paper presents findings from an experimental study on the characterization of the overall cooling effectiveness of an effusion-cooled liner wall, which was representative of a can combustor under heated flow (non-reacting) and lean-combustion (reacting) conditions. The model can-combustor was equipped with an industrial swirler, which subjected the liner walls to engine representative flow and combustion conditions. In this study, two different effusion cooling liners with an inline and staggered arrangement of effusion holes have been studied. Non-dimensionalized streamwise hole-to-hole spacing (z/d) and spanwise hole-to-hole spacing (r/d) of 10 were used for both the effusion liners. These configurations were tested for five different blowing ratios ranging from 0.7 to 4.0 under both reacting and non-reacting conditions. The experiments were carried out at a constant main flow Reynolds number (based on combustor diameter) of 12,500. The non-reacting experiments were carried out by heating the mainstream air, and the reacting experiments were carried out under flame conditions at a total equivalence ratio of 0.65. Infrared Thermography (IRT) was used to measure the liner outer surface temperature, and detailed overall effectiveness values were determined under steady-state conditions. It was

observed that overall cooling effectiveness trends were different under reacting and non-reacting conditions. The cooling effectiveness for the non-reacting experiments exhibited a decreasing trend, and no consistent location of minimum cooling effectiveness was observed for the range of blowing ratios investigated in this study. For the reacting cases, the cooling effectiveness first follows a decreasing trend, reaches a distinct minimum, and then increases till the end of the combustor. Under non-reacting conditions, the staggered configuration was 9-25% more effective than inline configuration, and under-reacting conditions, the staggered configuration was 4-8% more effective than inline configuration. From this study, it is clear that the coolant-flame interaction for the reacting experiments impacted the liner cooling effectiveness and led to different overall cooling effectiveness distribution on the liner as compared to the non-reacting experiments.

3.2. INTRODUCTION

With the rising fuel costs and environmental concerns, there has been a strong push towards increasing fuel efficiency and decreasing harmful emissions in modern gas turbines. The Environmental Protection Agency (EPA) in the United States limits NO_x emissions of new stationary gas turbines firing natural gas to 15 ppm at 15% O₂ for installations over 250 MW, making pollution management a top priority for combustor design. [3.1] The most promising approach to reduce pollutant emission is through swirl stabilized lean premixed combustion. In lean combustion applications, a considerable amount of air is routed into the combustion chamber through the swirler to reduce NO_x emissions, reducing the amount of air available for cooling the combustor liner. Simultaneously, there is a constant requirement to raise the combustor and turbine sections' temperature to increase overall turbine efficiency. As a result, combustor liners in

modern gas turbines are subjected to very high temperatures and high thermal gradients that severely impact their structural integrity. To this end, the development of optimized combustor liner cooling technologies is crucial to increase the life of modern combustor components.

A principal method used to manage the high heat loads on the combustor liners is film cooling. Film cooling refers to the injection of coolant onto a surface through holes to form an insulating layer between hot freestream air and the surface. Discrete film cooling often leads to a free film cooling layer over the liner and excessive coolant flow, which causes the coolant jet to overshoot and weakens its effectiveness. Effusion cooling, also known as full coverage film cooling, overcomes these issues by having successive rows of film cooling holes interacting and forming a continuous protective film along the wall [3.2]. Studies on full coverage film cooling and effusion cooling have been conducted since the early 1950s.

One of the first studies to compare the full coverage film cooling with proper backside convection cooling was by Meyers et al. [3.3]. The authors performed infrared thermography to study the cooling effectiveness of different cold side and effusion cooling configurations for a flat plate. The authors reported that even though the extended surfaces on the combustor liner provided higher cooling effectiveness, the pressure drop was significantly higher than the effusion cooling configurations. A detailed review on gas turbine effusion cooling studies was carried out by Krewinkel [3.4]. Andrews et al. [3.5 - 3.7] investigated the effects of various factors on full-coverage film-cooling such as the total number of holes, inclination angle, and length of holes. Harrington et al. [3.8] studied orthogonal effusion holes and concluded that an asymptotic fully developed adiabatic effectiveness value was established within four or eight rows. Ligrani et al. [3.9] presented effectiveness and heat transfer results for full coverage film cooling arrangements and studied the effect of the blowing ratio and the influence of dense and sparse hole arrays on

effectiveness. Facchini et al. [3.10] investigated a combustor geometry that includes slot-style starter films and dilution ports. Scrittore et al. [3.11] have reported detailed velocity and adiabatic effectiveness measurements for an effusion geometry in a simulated combustor environment. Some other investigations on effusion cooling can be found in Sasaki et al. [3.12], Leger et al. [3.13], Rogers et al. [3.14], and Motheau et al. [3.15].

There has been a shift towards testing effusion cooling configurations under realistic swirl flow conditions in recent times. Behrendt and Hassa [3.16] developed a high-pressure rig to studied the cooling performance of effusion-cooled liners under typical gas turbine conditions such as the temperature ratio and turbulence parameters. Behrendt et al. [3.17] reported cooling effectiveness of effusion and impingement-effusion cooling configurations through steady-state IRT experiments. The authors concluded that the cooling air pressure drop has a minor influence on the cooling effectiveness, and the impact increases with an increase in hot gas pressures. Wurm et al. [3.18] developed an atmospheric planar three-swirler set up to test different effusion cooling liners' performance. Their rig's main advantage was that the effect of the actual combustor flow field and heat load on the cooling effectiveness could be studied in detail. To further mimic realistic conditions, the authors also incorporated slot film cooling. Wurm et al. [3.19] compared the performance of effusion-cooled liner under different operating conditions. They observed that cooling effectiveness increased with the increase in pressure drop. Andrei et al. [3.20] performed experiments to evaluate the cooling performance of flat plate effusion-cooled combustor liners. The authors carried out an effectiveness test using pressure-sensitive paint (PSP) and overall effectiveness using thermocouple-based measurements. They reported that for higher blowing ratios, the orthogonal holes performed better than the inclined holes. It was concluded that the hole density had a significant impact on the performance of the effusion liners. Kakade et al. [3.21]

also conducted experiments to study the dependence of mainstream turbulence parameters on the performance of a staggered flat plate effusion-cooled liner. The authors studied the effect of blowing ratio, free-stream turbulence intensity, and free-stream turbulence length scale on the variation of cooling effectiveness of the cooling plates.

In the recent past, there have been efforts made to study effusion cooling under realistic flame conditions. Ge et al. [3.22] and Ji et al. [3.23] carried out experiments to compare effusion liners' performance for an annular combustor under-reacting and non-reacting conditions. The authors compared the performance of outer and inner liners of a model annular combustor at different blowing ratios and equivalence ratios. Hermann et al. [3.24] developed an experimental rig to investigate combustion characteristics for an effusion-cooled single sector model gas turbine combustor. Greifenstein et al. [3.25] conducted experimental studies using OH-PLIF, PIV, CARS, and TPT to study coolant flame interactions. The authors demonstrated a variation of 10-34% of cooling effectiveness between regions with coolant flame interaction and the post-flame area. Rivera et al. [3.26] investigated the interaction of laminar, premixed flame with cold gas jets.

Although many studies on combustor liner wall cooling have been carried out in the past, including realistic swirl stabilized flow fields and cooling conditions, there is still a lack of investigations under gas turbine combustion conditions with coolant-flame interactions. The present study deals with characterizing effusion cooled liner wall performance under typical gas turbine reacting conditions for a swirl stabilized can combustor.

The present study deals with the investigation of effusion-cooled liner walls under realistic reacting and non-reacting conditions for a swirl stabilized can combustor. This paper aims to evaluate and compare the overall cooling effectiveness of staggered and inline cooling configurations at different blowing ratios between reacting and non-reacting conditions. Steady-

state IRT experiments were performed to measure the liner outer wall temperature, and detailed overall cooling effectiveness results have been presented and discussed. The data obtained in this study aims to aid designers of gas turbine components and the development and validation of numerical codes for accurate prediction of heat transfer performance of such components.

3.3. EXPERIMENTAL SETUP

The experiments were carried out in the Thermal Energy Research and Management Laboratory (ThERMaL) at North Carolina State University. The experimental setup has been shown through a schematic in Fig. 3.1. Compressed air was drawn at 0.82 MPa and was routed through a turbine mass flow meter with pressure and temperature measurements for flow metering. The mass flow measurement uncertainty was $\sim 2.03\%$ for all cases. The air was then routed to a pressure regulator and a PID-controlled flow control valve, which allowed fine control over the desired flow rate. An inline 192 kW heater was also installed in this setup and served as the sole heating source for the non-reacting experiments.

A detailed schematic of the test section has been shown in Fig. 3.1 and Fig. 3.2. The test section consisted of a settling chamber that houses an industrial low emission swirl nozzle. The fuel nozzle includes an axial swirler, followed by fuel injectors downstream that introduce fuel into the nozzle annular channel for effective premixing. Air entered the nozzle as indicated by the arrows and passed through the swirl vane, and imparted tangential velocity to the flow. Fuel was injected through the ports present downstream of the swirler vanes. The fuel and air mixed along the length of the nozzle before entering the combustion chamber. The diameter of the nozzle (DN) was 70 mm. The main non-dimensional parameter to characterize combustor swirling flows is the swirl number. The definition used is given by Eq. 3.1

$$S = \frac{G_{\theta}}{D_N G_x} \text{ (Eq. 3.1)}$$

Where G_{θ} is the axial flux of angular momentum, G_x is the axial flux of axial momentum and D_N is the nozzle diameter. The swirl number for the conditions of flow investigated in this study is 0.74 ± 0.04 [3.27]. A schematic of the fuel nozzle is shown in Fig. 3.3.

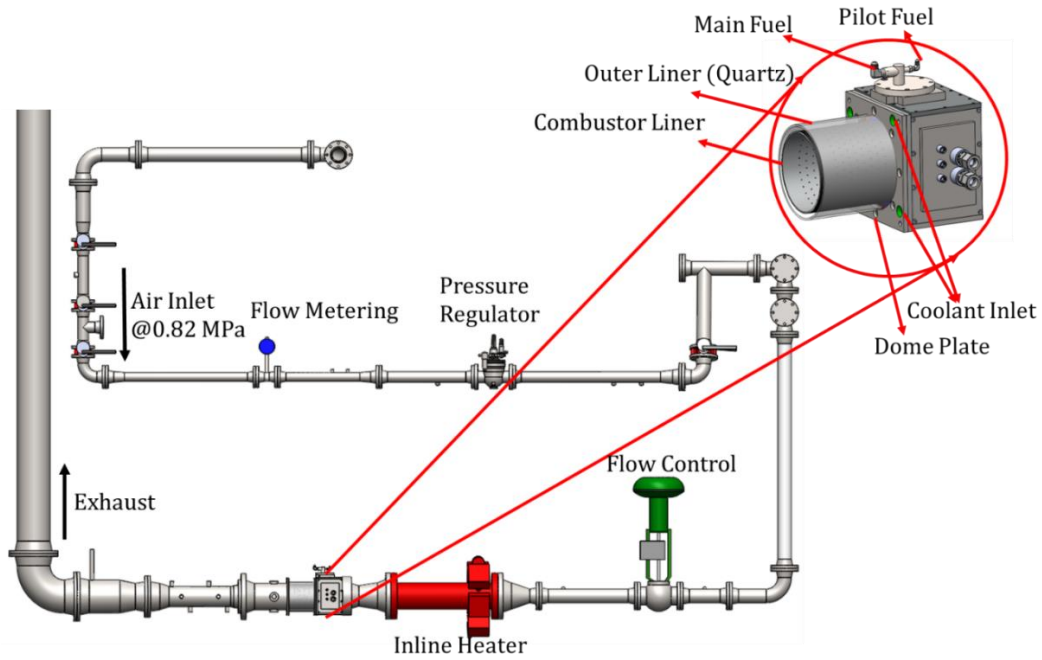


Figure 3.1: Combustor rig test setup

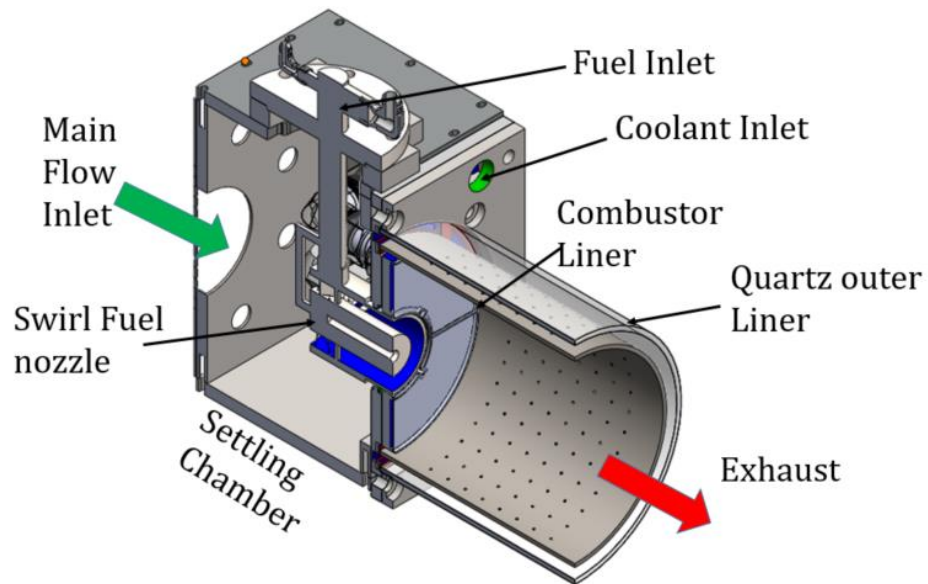


Figure 3.2 Schematic of the Test Section

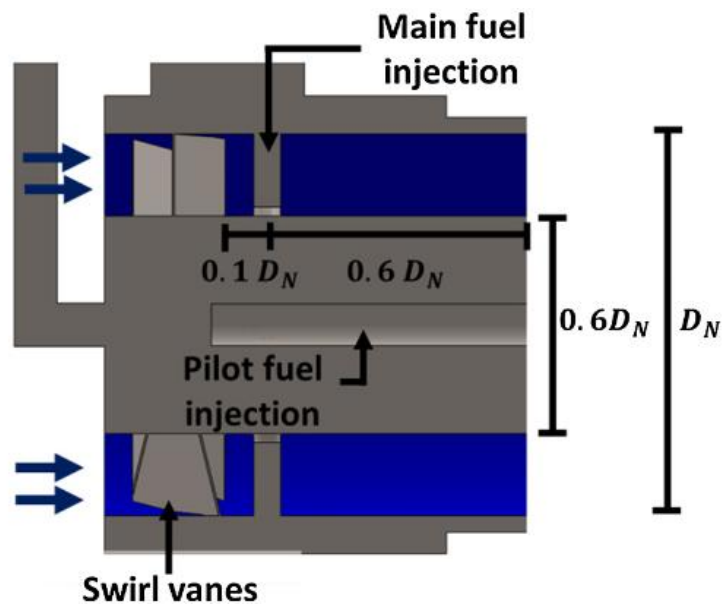


Figure 3.3 Schematic of the fuel nozzle

The combustor liner was a cylindrical chamber made of stainless steel (SS316). The combustion chamber's outer diameter, length, and thickness were 211 mm, 216 mm, and 3 mm, respectively. Effusion cooling holes were machined on the combustion liner using traditional CNC machining. The combustion liner was enclosed by a transparent 4 mm thick quartz cylinder of outer diameter 235 mm. The gap between the outer quartz liner and the inner metal liner was 8 mm.

The fuel was supplied to the nozzle through inlet fuel ports in the settling chamber. The fuel inlet port consisted of separate inlets for the main fuel and pilot fuel. Alicat MCR series mass flow meters were used to meter the main and pilot fuel lines separately before entering the settling chamber.

The settling chamber also included a plenum that fed the coolant air to the test section. The coolant plenum was designed to be isolated from the primary airflow. Four separate coolant feed lines, independent of the main air supply, were used to supply the coolant to the coolant plenum. Omega FMA-A2307 flowmeters were used to meter the coolant supplied to the test section. A pressure transducer was connected to the coolant plenum to measure the pressure drop across the liner configuration. The coolant air from the plenum feed was routed through the annular space between the outer quartz liner and the combustor liner and bled into the combustion chamber via the effusion holes. The exhaust air from the test section was vented into the atmosphere through a vertical duct. The tests were performed at ambient laboratory pressures. Different operations involved in conducting the experiments and subsequent data acquisition were controlled through an in-house developed LabVIEW program.

A schematic of the effusion cooling liner is shown in Fig. 2.5. The diameter of each cooling hole was 2 mm. The normalized streamwise hole-to-hole $\left(\frac{z}{d}\right)$ and spacing and circumferential hole-to-hole $\left(\frac{r}{d}\right)$ spacing were set as 10, representing actual liner applications. The effusion holes were 272 orthogonal (90°) holes distributed throughout the liner in eight streamwise rows. Angled effusion holes will be the subject of a future study. The region of interest (ROI) for the overall effectiveness calculation is shown in Fig. 2.5. Since the temperature distribution for the can combustor at steady-state conditions has been observed to be axisymmetric by previous studies on the same geometry [2.27 – 2.29], it was assumed that the cooling effectiveness evaluated over the ROI is representative of the entire combustor liner.

3.4. EXPERIMENTAL PROCEDURE AND DATA REDUCTION

The following section details the experimental methodology, operating conditions, and data reduction procedure used in this study.

3.4.1. Infrared (IR) Thermography

The measurement methodology has been shown in Fig. 2.6. The combustor liner's outer surface (cold side) temperature was measured and analyzed for the results in this study. Based on the previous studies on this combustor rig, the Biot number range was found to be around 0.007 to 0.03 for the reacting and non-reacting conditions, respectively. [2.27 - 2.29] Due to the low Biot number, the combustor liner's temperature is reasonably assumed constant throughout the thickness.

The combustor liner wall's temperature was measured using a FLIR A6750SC IR camera equipped with a 50 mm 1-5 μm broadband lens. A KG2 Schott glass filter was used with the IR camera lens to remove the outer quartz liner absorption and emission signal. The IR camera had a spectral response range from 1 to 5 μm , and the Schott glass filter absorbed radiation in the range of 2.8 to 5 μm . Quartz glass is transparent (without absorption or emission) in the 1 to 2.8 μm range and hence was suitable for this application [2.28].

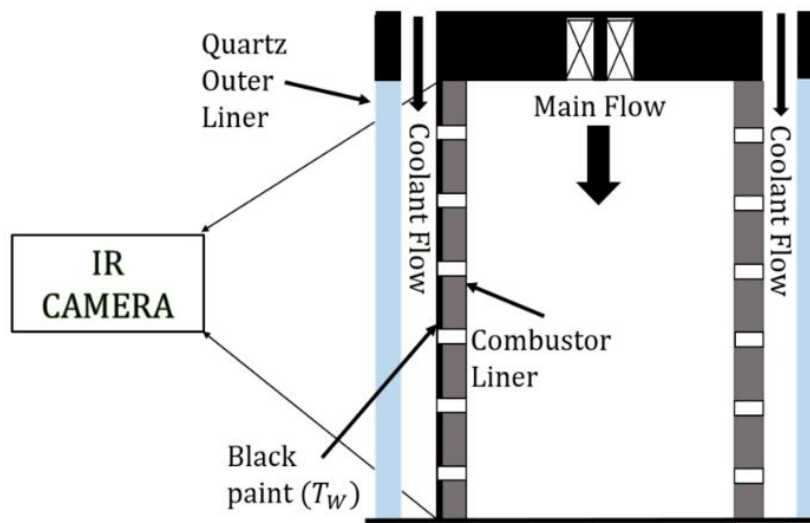


Figure 3.6 IR Methodology

However, as the quartz outer liner surrounded the combustor liner wall, the temperature signal recorded by the IR camera will not be the accurate wall temperature. A calibration process was followed to establish a relationship between the actual liner wall temperature measured by the thermocouple and the IR camera's raw output. This relationship was used to calculate the actual temperature of each pixel of the liner wall as recorded by the IR camera. To reduce the

measurement error induced by reflection of the metal surface, the metal liner was painted with Rust-Oleum® black paint.

The calibration experiment was carried out using four thermocouples placed axially along the length of the metal liner as shown in Fig. 2.7. The data acquired through the thermocouple and IR camera were then synchronized. The calibration experiment was carried out to account for the entire range of encountered temperatures during the actual investigations. Separate calibration experiments were carried out for the inline and staggered combustor liners. A sample calibration curve obtained for the reacting case is presented in Fig. 3.8.

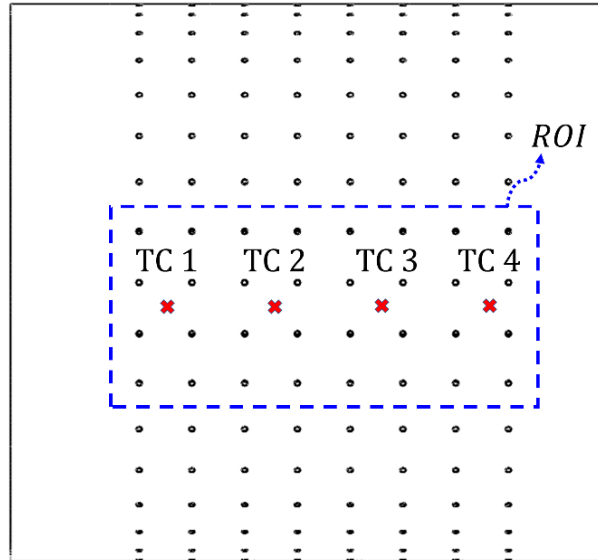


Figure 3.7 Schematic of ROI with the location of calibration thermocouples

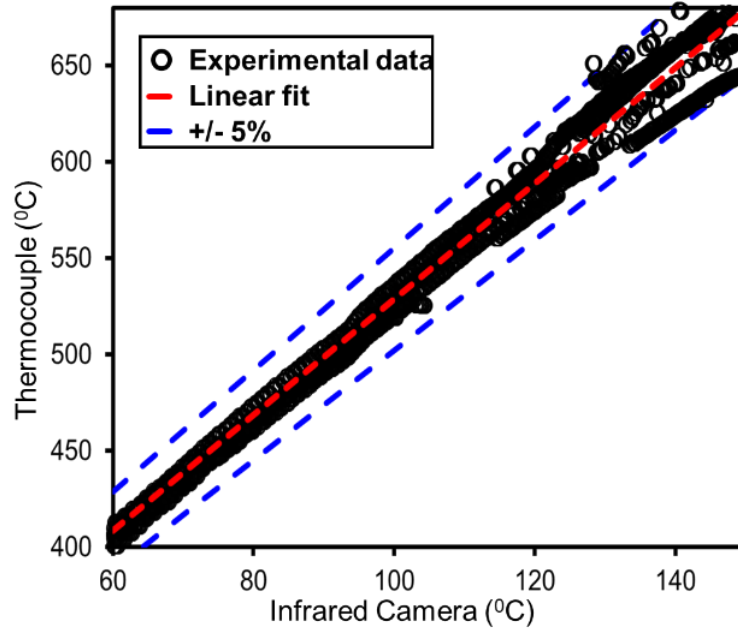


Figure 3.8 Calibration curve for the reacting case

All experiments presented in the study were carried out at steady-state conditions. The test section was considered to be at steady-state when the rise in temperature of the liner wall as recorded by the IR camera for every pixel in ROI was less than 0.2 °K over one minute for all non-reacting experiments and 1°K over one minute for the reacting experiments.

3.4.2. Data reduction

Cooling effectiveness is given as,

$$\eta = \frac{(T_g - T_w)}{(T_g - T_c)} \quad (Eq. 3.2)$$

where, T_g is the gas or air temperature on the hot side of the combustor liner, T_w is the wall temperature measured by the IR camera and T_c is the coolant temperature. Due to the complexities in measuring the flame temperatures and swirling flow temperatures, the gas temperature, T_g , for the reacting and non-reacting cases were approximated as adiabatic flame temperature and inlet temperature to the swirler, respectively. Coolant temperature T_c was measured at the inlet of the test section using a K-type thermocouple, and the wall temperature T_w was measured using the IR camera.

3.4.3. Operating conditions

All the experiments were performed at the main flow Reynolds Number ($Re_{combustor}$) of 12,500, where $Re_{combustor}$ is defined as

$$Re_{combustor} = \frac{\dot{m}_{a_g} D_{combustor}}{A_{combustor} \mu} \quad (Eq. 3.3)$$

To quantify the effect of the amount of coolant on the overall cooling effectiveness of the effusion liners, a commonly used parameter in literature is the Blowing ratio (BR),

$$BR = \frac{(\rho v)_c}{(\rho v)_g} \quad (Eq. 3.4)$$

The blowing ratio defined in this experiment is the average values based on the measured coolant and main flow mass flow rates. Experiments were carried out at different blowing ratios of 0.7, 1.4, 2.0, 3.0, and 4.0. The values of the blowing ratio were achieved by increasing the coolant air flow rate and maintaining the main flow rate constant. The blowing ratio and Reynolds number for the reacting experiments were also defined based on the main airflow rate. This was done to maintain uniformity of the ratio of coolant mass flow rate to main air mass flow rate (λ) over the reacting and non-reacting experiments.

This parameter is defined as λ , and is defined as

$$\lambda = \frac{\dot{m}_{a_c}}{\dot{m}_{a_g}} \text{ (Eq. 3.5)}$$

The λ values corresponding to the above-mentioned blowing ratios are 1.9%, 3.8%, 7.9%, and 10.5%, respectively. All the non-reacting (heated flow) experiments were carried out by heating the mainstream flow to 448°K using the inline heater. All the experiments were performed at a main flow equivalence ratio of 0.65. The equivalence ratio was calculated based on the total air supplied to the test section, i.e., the sum of the coolant and primary air mass flow rates. In all the experiments, the pilot fuel mass flow rate was maintained at 6% of the primary fuel mass flow rate, which was representative of a can combustor, and the pilot flame was maintained throughout the experiment. The equivalence ratio calculation is shown through Eqns. 3.6-3.8.

$$\dot{m}_{air_{total}} = \dot{m}_{a_c} + \dot{m}_{a_g} \text{ (Eq. 3.6)}$$

$$\dot{m}_f = \dot{m}_{f_{pilot}} + \dot{m}_{f_{main}} \quad (Eq. 7)$$

$$\phi_{total} = \frac{AF_{stoic}}{AF} = \frac{\dot{m}_{f(actual)}}{\dot{m}_{f(stoic)}} \quad (Eq. 8)$$

The operating conditions for the combustor rig for non-reacting and reacting conditions have been summarized in Table 3.1 and Table 3.2.

Table 3.1: Operating conditions of combustor rig for non - reacting conditions

Main air flow Reynolds Number	12,500
Main Air Inlet Temperature	448°K
Coolant Temperature	293°K
Ambient laboratory pressure	101897 Pa

Table 3.2 Operating conditions of combustor rig for reacting conditions

Main air flow Reynolds Number	12,500
Main Air Inlet Temperature	448°K
Equivalence ratio	0.65
Pilot percentage	6%
Coolant Temperature	293°K
Ambient laboratory pressure	101897 Pa

3.5. UNCERTAINTY

The experimental uncertainty was calculated using the sequential perturbation method developed by Moffat et al. [3.30]. The thermocouples used in this setup have an inherent error of 1.1°C , the liner wall temperature has an error of $\pm 2.73\text{K}$ for the non-reacting cases and $\pm 6.11\text{K}$ for the reacting cases, accounting for the calibration error. Using the sequential perturbation method, the overall cooling effectiveness error for the non-reacting experiment was ± 0.022 and for the reacting experiment was ± 0.041 . The main mass flow rate was calculated from the readings of a turbine flow meter upstream of the setup with simultaneous temperature and pressure measurements. The uncertainty in the mass flow measurement was $\sim 2.03\%$ for all cases.

3.6. RESULTS AND DISCUSSION

3.6.1. Flow field in the combustor

Fig. 3.8 represents a typical swirling flow in a can combustor. As shown, the incoming flow from the swirler expands, impinges, and attaches to the combustor liner wall. This impingement and flow attachment leads to the formation of the corner recirculation zone and central recirculation zone. The corner recirculation zone region is defined by lower heat transfer rates due to limited mixing and relatively slower flow velocities. Downstream of the impingement region, the swirling jet attached to the wall, and the resulting formation of the boundary layer lead to a decrease in the heat transfer. The corner recirculation zone, central recirculation zone, and associated shear layers play an important role in stabilizing the combustion flame and significantly affect the heat transfer characteristics and the liner wall's temperature distribution. Ramirez et al. [3.27] and Park et al. [3.29] have conducted detailed studies on the heat transfer and flow-field under non-reacting and reacting conditions for the current experimental setup and the discussion

presented is based on the studies mentioned above. Fig. 3.9 shows the mean velocity of non-reacting and reacting flow in a can combustor equipped with the industrial swirler without any effusion holes. The flow measurement was carried out at a Reynolds number of 12500, which was representative of the operating conditions in this study. The measurement was carried out in a $1.45D_N \times 1.5D_N$ plane at the start of the combustor region, including the main flow impingement locations. Since the combustor's mean flow is assumed to be axisymmetric across the centerline, only half of the center plane is shown in Fig. 3.9. The velocity presented in Fig. 3.9 has been non-dimensionalized with the mean nozzle velocity (v_{ref}). The equation to calculate v_{ref} is shown in Eq. 3.8. The mean nozzle velocity was calculated based on the inlet main air mass flow rate and the annular area of the nozzle.

$$v_{ref} = \frac{\dot{m}_{a_g}}{\rho_g A_{nozzle}} \quad (Eq. 3.8)$$

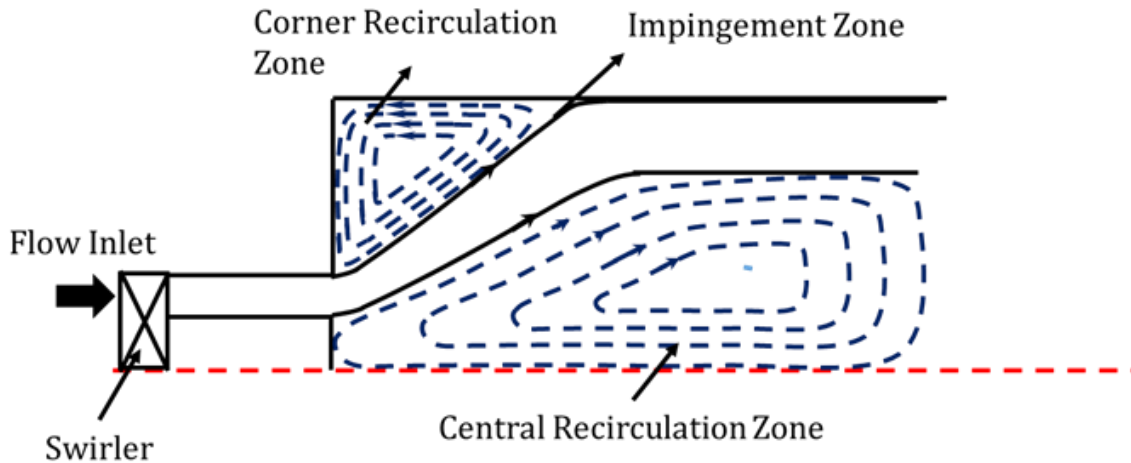


Figure 3.9 Flow features within a can combustor

For the non-reacting and reacting flows, the impingement region was found to be around $\frac{z}{D_N} \sim 1.16$. The authors had noticed self-similarity in reacting flows regardless of the combustor operating conditions and reported an impingement location of $\frac{z}{D_N} \sim 1.16$ with a 7% deviation for a wide range of conditions tested in the study. An interesting observation by authors has been that the location impingement does not correspond to the maximum heat transfer location. For the non-reacting cases, the authors noted that the location of peak heat transfer occurs $\sim 0.2 D_N$ upstream of the impingement region. [2.28] For the reacting cases, the authors found that the peak temperatures occur $\sim 0.3 D_N$ downstream of the flame jet impingement location. [3.29]

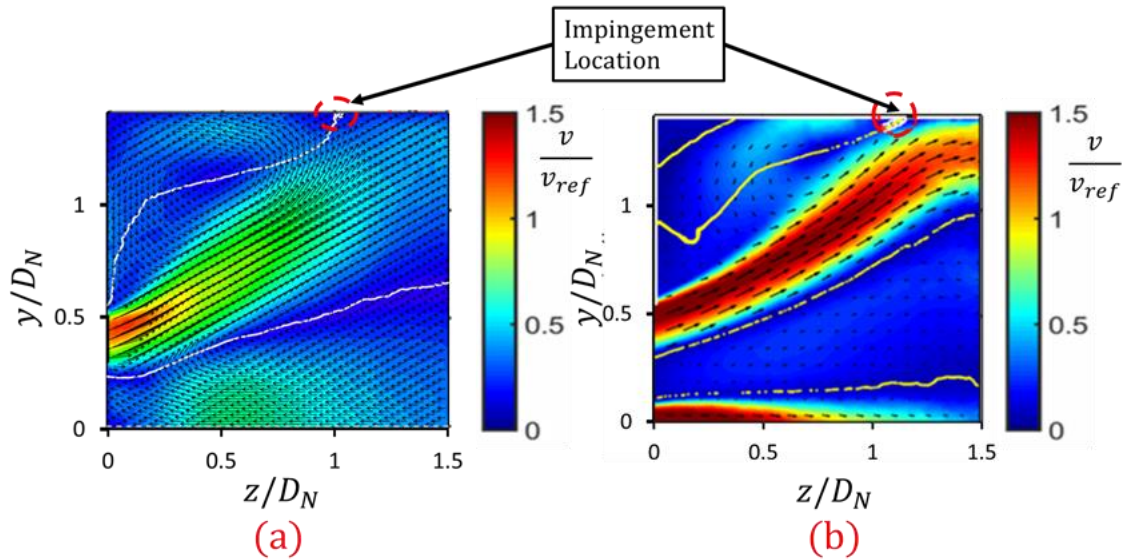


Figure 3.10 Mean velocity of flow at (a) Non-reacting conditions [3.27] and (b) reacting conditions at 0.65 equivalence ratio without cooling holes [3.29]

3.6.2. Experimental Overall Cooling Effectiveness – Non-Reacting Flow

The non-reacting flow experiments were conducted by heating the mainstream flow to 448K through the inline heater. The mainstream temperature T_g was measured by a thin K-type thermocouple placed at the inlet to the swirler. The detailed cooling effectiveness for staggered and inline cooling configurations with the change in blowing ratio has been presented in Fig. 3.11. The axial distance (z) has been normalized with the diameter of the swirler nozzle (D_N). The effectiveness contours were found not to be completely axisymmetric due to a combination of hot gas flow and conduction losses in the rig. However, the effects were found to be relatively minimal, and it is expected that the cooling effectiveness in the ROI is representative of the entire liner.

A similar trend was observed for the inline and staggered arrangement of effusion holes for the range of blowing ratios investigated in this study. For low values of z/D_N , high cooling effectiveness is observed. The low-pressure recirculation zone near the liner wall in this region leads to lower liner wall temperatures and high cooling effectiveness. The corner recirculating flow is in the opposite direction of the main flow, leading to increasing temperatures and decreasing cooling effectiveness upto $\frac{z}{D_N} \sim 1.5$. As discussed earlier, at around $\frac{z}{D_N} \sim 1.16$, the swirl flow impinges on the liner walls for the case without any effusion cooling. The decreasing cooling effectiveness trend till $\frac{z}{D_N} \sim 1.5$ shows that the cooling flow interacts with the main swirling flow and negates the impingement effect on the liner wall temperature distribution to a certain degree. A consistent location of minimum cooling effectiveness was not observed for the range of blowing ratios investigated for the non-reacting studies. A similar trend for cooling effectiveness in non-reacting cases was also noted by Ge et al. [3.22].

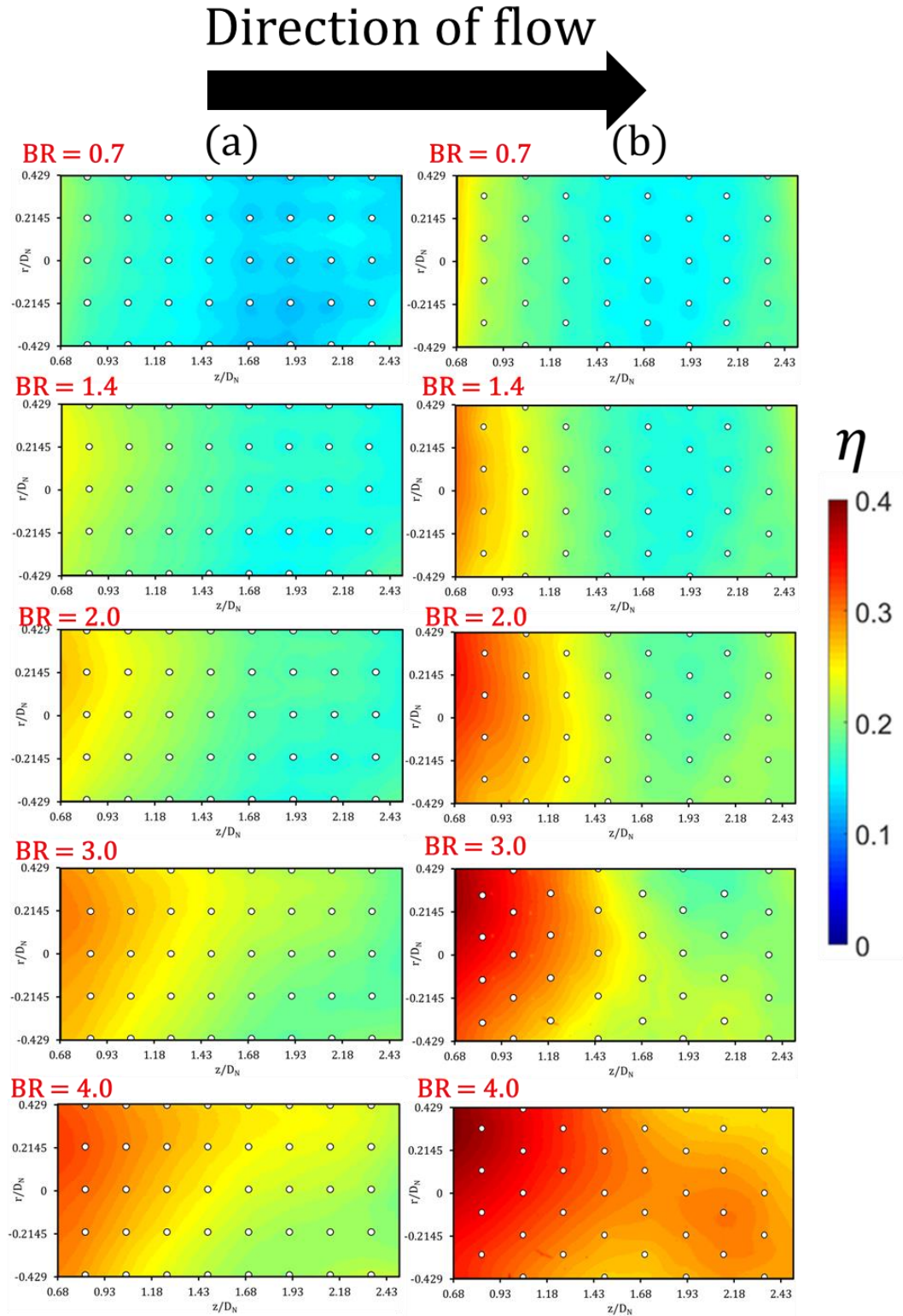


Figure 3.11 Overall Cooling Effectiveness Contour at non-reacting conditions for (a)

Inline Configuration (b) Staggered Configuration

Also, an interesting factor to note is that the main flow impingement and attachment at large values of $\frac{z}{D_N}$ leads to the formation of a relatively high-pressure region that routes a significant amount of coolant to flow into the combustor at low values of $\frac{z}{D_N}$. This phenomenon leads to insufficient coolant flow towards the end of the combustor liner and lower cooling effectiveness in this region. Additional cooling features such as slot cooling will be imperative for a more uniform distribution of cooling effectiveness along the length of the liner.

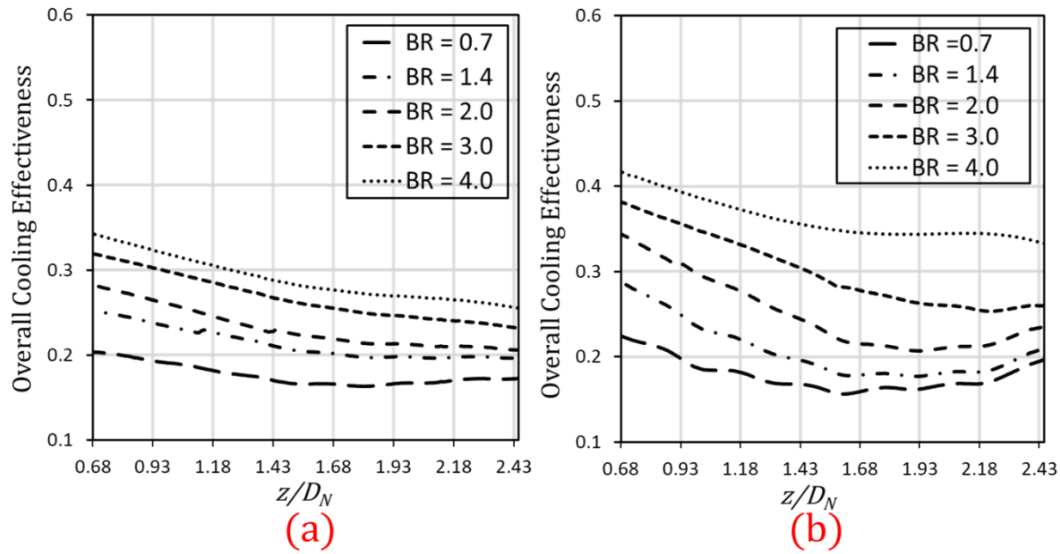


Figure 3.12 Spanwise averaged cooling effectiveness contour at non-reacting conditions for (a) Inline configuration (b) Staggered Configuration

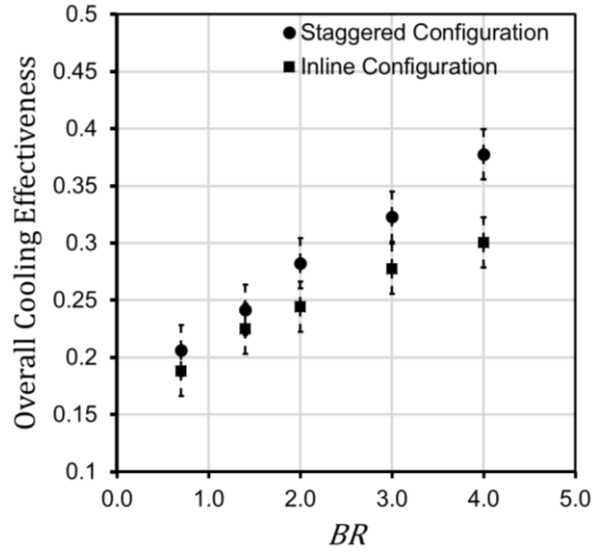


Figure 3.13 Area averaged cooling effectiveness under non-reacting conditions

The spanwise averaged cooling effectiveness for the inline and staggered arrangement of holes for the non-reacting cases is shown in Fig. 2.12. With an increase in the blowing ratio, a consistent increase in cooling effectiveness was observed across the staggered and inline liners investigated in this study. This shows that percentage coolant distribution through each row of effusion holes remains the same for different blowing ratios. An increase of 48% and 53% was observed in overall cooling effectiveness for the inline and staggered configurations, respectively, across the range of blowing ratios investigated in this study. Existing literature has shown conditions where, after a specific increase in coolant flow rate, combustion liners' effectiveness does not increase with an increase in coolant ratio. At these conditions, the liners are said to overcooled [3.9]. This phenomenon was not noticed for the coolant ratios investigated in this study. In this initial region, higher cooling effectiveness was observed for the staggered configuration than the inline configuration. For $\frac{Z}{D_N} < 1.5$, the staggered effusion configurations were found to be

on average 24% more effective than the inline designs. At higher values of $\frac{Z}{D_N}$, the average difference in cooling effectiveness between inline and staggered configurations reduces to 11%, implying that a bulk of the coolant flow was diverted through the initial few cooling holes, as has been discussed earlier.

Fig. 3.13 represents the total area-averaged cooling effectiveness for the inline and staggered configurations. Due to the more uniform distribution of coolant holes on the liner wall, the staggered configuration performed better than the inline configurations. A difference of 9-25% was observed between the inline and staggered configurations across the range of conditions studied.

3.6.3. Overall Cooling Effectiveness - Reacting flow

The reacting flow experiments were carried out for a premixed methane-air flame at a total equivalence ratio of 0.65. For the reacting experiments due to the complex conical flame structure, calculating the driving temperature's local variation was complicated. It was also observed that intrusive temperature measurement probes affect the flow dynamics in the combustor. For the results presented in the section, the mainstream temperature T_g is approximated as the constant adiabatic flame temperature calculated at the main flow rate equivalence ratio. However, this assumption leads to a significantly different range of cooling effectiveness than the non-reacting experiments. Hence, a direct comparison of the cooling effectiveness magnitudes between the reacting and non-reacting experiments will not be appropriate for this study.

The detailed cooling effectiveness contours are presented in Fig. 3.14. It was observed that overall cooling effectiveness trends were different under-reacting and non-reacting conditions.

For low values of $\frac{z}{D_N}$, the overall cooling effectiveness was high. As in the non-reacting cases, the flow in this region is dominated by the corner recirculating flow leading to lower liner temperatures and higher overall effectiveness. A significant difference between the reacting and non-reacting cases is the existence of a distinct minimum in cooling effectiveness. As discussed in the section, at around $\frac{z}{D_N} \sim 1.16$ the flame impinges on the combustor liner wall leading to a sharp increase in liner wall temperature in this region. This leads to continuously decreasing cooling effectiveness and a subsequent minimum in cooling effectiveness. The flame impingement on the liner walls also leads to a high-pressure zone in the combustor. This high-pressure region reduces the coolant flow into the combustor in this region, decreasing the cooling effectiveness. Post the impingement region, the flow attaches to the liner wall and is dominated by combustion products rather than the flame, leading to reduced wall temperatures and higher effectiveness in this region.

This leads to an increasing cooling effectiveness trend till the end of the liner. This distinct minimum observed in the cooling effectiveness region again emphasizes the need for other cooling features such as slot cooling to improve this region's cooling effectiveness and decrease thermal loads.

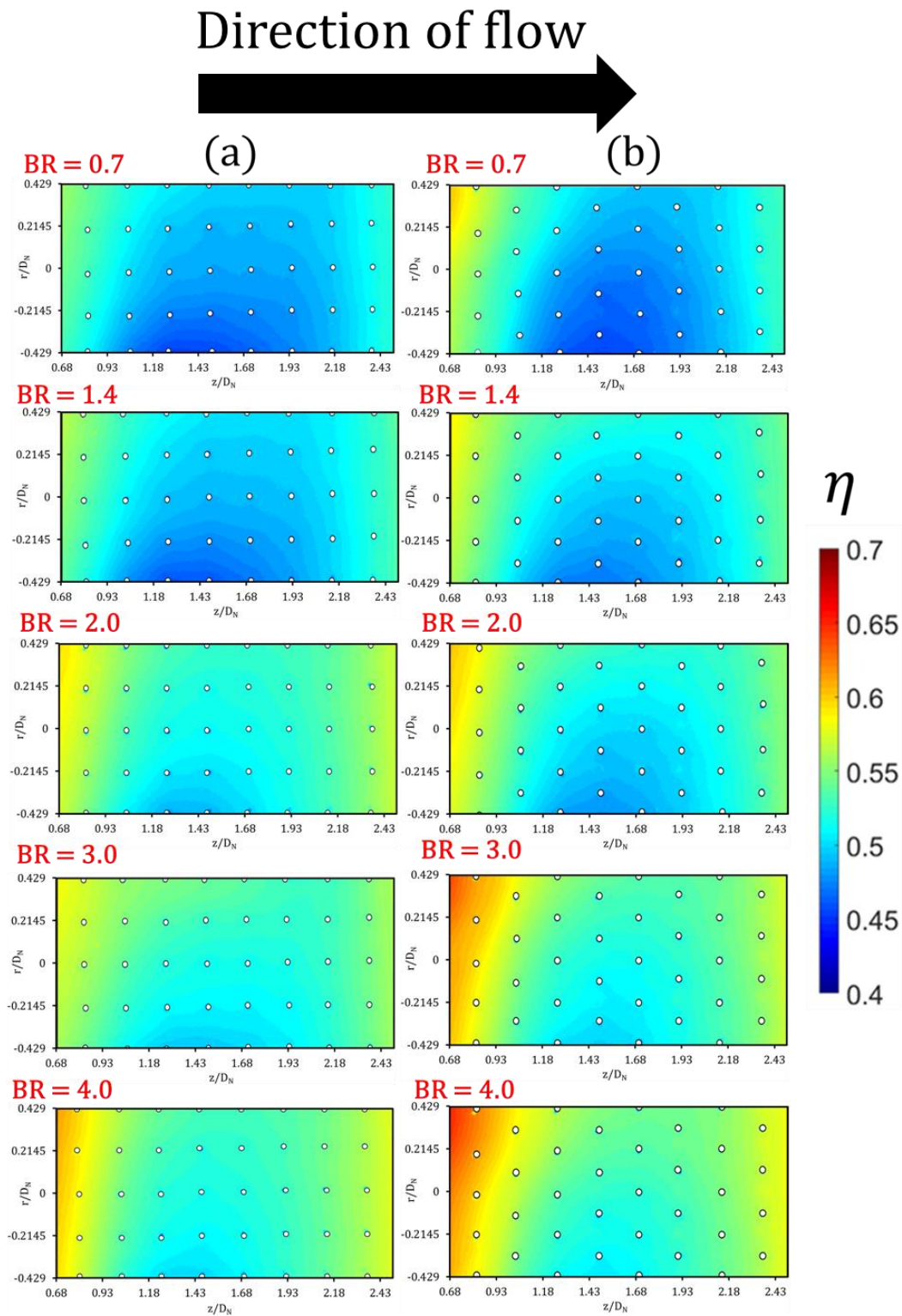


Figure 3.14 Overall Cooling Effectiveness Contour at reacting conditions for (a) Staggered Configuration (b) Inline Configuration

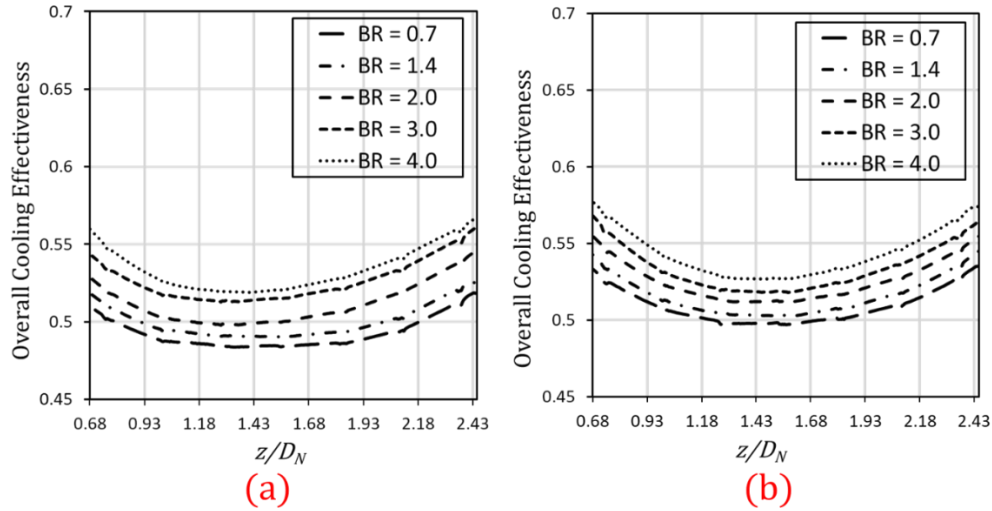


Figure 3.15 Spanwise averaged cooling effectiveness at reacting conditions for (a) Inline configuration (b) Staggered configuration

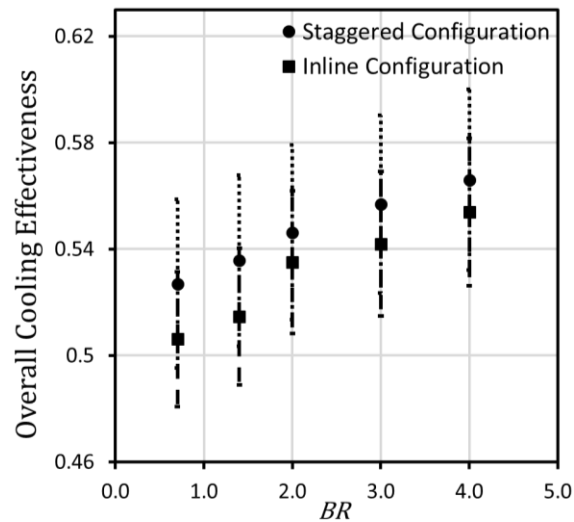


Figure 3.16 Area averaged cooling effectiveness under reacting conditions

The spanwise averaged cooling effectiveness for the inline and staggered arrangement of holes for the reacting cases is shown in Fig. 2.15. An interesting result observed from the

effectiveness contour and the spanwise averaged cooling effectiveness is that the point with the minimum cooling effectiveness $\frac{z}{d} = 1.4 \sim 1.45$ does not correspond to the location of impingement $\frac{z}{d} \sim 1.16$ but is instead downstream of it. This can be attributed to the fact the flame temperature is higher in the downstream region than at the location close to the impingement region [3.29]. This feature is different from experiments in literature done under non-reacting conditions where the maximum heat transfer location and lowest cooling effectiveness corresponds to the area of impingement on the liner wall [3.19].

The location and value of the minimum cooling effectiveness were observed to be consistent over the staggered and inline configurations. As in the non-reacting conditions, with an increase in the blowing ratio, a constant increase in cooling effectiveness was observed. Since there was a considerable difference between mainstream temperatures for the reacting and non-reacting conditions, the increase in cooling effectiveness with blowing ratio was considerably lower for the reacting experiments than the non-reacting experiments.

Fig. 3.16 represents the total area-averaged cooling effectiveness for the inline and staggered configurations under-reacting condition. A difference of 2-5% was observed between the inline and staggered configurations. On account of having a more uniform distribution of coolant holes throughout the liner, the staggered configuration performs better than the inline configuration for both the reacting and non-reacting conditions. The main flow's energization due to reaction reduces the geometrical arrangement effect of the coolant flow between staggered and inline, especially at larger blowing ratios compared to non-reacting conditions.

3.7. CONCLUSIONS

Steady-state Infrared thermography experiments were performed to measure the liner wall temperature and evaluate the performance of effusion-cooled combustor liner under-reacting and non-reacting conditions. Two different configurations of an inline and staggered arrangement of effusion holes were tested for blowing ratios ranging from 0.7 to 4. Detailed cooling effectiveness contours, spanwise averaged cooling effectiveness, and total area-averaged cooling effectiveness values are presented.

It was observed that overall cooling effectiveness trends were very different under-reacting and non-reacting conditions. The spanwise cooling effectiveness for the non-reacting experiments exhibited a decreasing trend and became nearly constant for high values of z/D_N . A distinct location of minimum cooling effectiveness was not observed for the non-reacting cases implying that the coolant flow negates the effect of impingement to a certain degree in the non-reacting cases. A consistent increase in cooling effectiveness was observed with an increase in the blowing ratio.

For the reacting cases, the results showed that the cooling effectiveness first follows a decreasing trend along the combustor's length, reaches a distinct minimum, and then increases till the end of the combustor. The minimum in cooling effectiveness under reacting conditions shows that flame impingement onto the liner wall significantly impacts the overall cooling effectiveness distribution on the combustor liner walls. Another interesting observation has been that the location of minimum cooling effectiveness was found to be different from the swirl flow impingement location that has been found through previous experiments in uncooled combustors. This feature is unique to effusion cooling experiments done under reacting conditions and proves that coolant flame interaction affected the cooling performance of effusion liners. This effect of

reacting flow and effusion flow interaction needs to be investigated further. As observed in the non-reacting cases, a consistent increase in cooling effectiveness was observed with an increase in the blowing ratio.

The variation in cooling effectiveness from the inlet of the liner to the outlet of the liner for the reacting and non-reacting conditions shows the need for additional cooling features such as slot cooling to provide uniform cooling effectiveness along the length of the combustor liner.

The experiments found that the staggered configurations performed better than the inline configurations under both reacting and non-reacting cases. For the non-reacting conditions, the staggered configuration was 9-25% more effective than the inline configuration under reacting conditions, and the staggered configuration was found to be 2-5% more effective than the inline configuration.

Another challenging issue for future studies would be to figure out the suitable hot side temperature variation along the combustor liner to calculate local cooling effectiveness as compared to using an adiabatic flame temperature approach as used in this study.

NOMENCLATURE

z	Streamwise distance (m)
r	Circumferential distance (m)
d	Diameter of effusion hole
IRT	Infrared Thermography
D_N	Nozzle Diameter (m)
S	Swirl Number

G_{θ}	Angular flux of angular momentum
G_x	Axial flux of angular momentum
ROI	Region of interest
T	Temperature (K)
\dot{m}_a	Mass flow rate of air (kg/s)
A	Cross-section area (m ²)
Re	Reynolds number
AF	Air-Fuel Ratio
A	Cross section area (m ²)
ROI	Region of interest
u	Velocity(m/s)

Greek symbols

ϕ	equivalence ratio
ρ	density of air (kg/m ³)
η	Overall Cooling Effectiveness
λ	Coolant ratio

Sub scripts

f	Fuel
g	Main flow
c	Coolant flow
w	Wall
ref	Reference

REFERENCES

- [3.1] Environmental Protection Agency (EPA), 2006, “40 CFR Part 60, Standards of Performance for Stationary Combustion Turbines; Final Rule,” Federal Register, 71:38482-38506.
- [3.2] Lefebvre, A.H., 1998. Gas turbine combustion. CRC press.
- [3.3] Myers, G., Van der Geest, J., Sanborn, J. and Davis, F., 1985, July. “Comparison of advanced cooling concepts using color thermography”. In 21st Joint Propulsion Conference (p. 1289).
- [3.4] Krewinkel, R., 2013. “A review of gas turbine effusion cooling studies.” International Journal of Heat and Mass Transfer, 66, pp.706-722.
- [3.5] Andrews, G.E., Khalifa, I.M., Asere, A.A. and Bazdidi-Tehrani, F., 1995, June. “Full coverage effusion film cooling with inclined holes.” In Turbo Expo: Power for Land, Sea, and Air (Vol. 78811, p. V004T09A045). American Society of Mechanical Engineers.
- [3.6] Andrews, GE, Asere, AA, Gupta, ML, & Mkpadi, MC. "Full Coverage Discrete Hole Film Cooling: The Influence of Hole Size." Proceedings of the ASME 1985 International Gas Turbine Conference and Exhibit. Volume 3: Heat Transfer; Electric Power. Houston, Texas, USA. March 18–21, 1985. V003T09A003.
- [3.7] Andrews, G.E., Asere, A.A., Gupta, M.L. and Mkpadi, M.C., 1985, March. “Full coverage discrete hole film cooling: the influence of hole size.” In Turbo Expo: Power for Land, Sea, and Air (Vol. 79405, p. V003T09A003). American Society of Mechanical Engineers.
- [3.8] Harrington, M.K., McWaters, M.A., Bogard, D.G., Lemmon, C.A. and Thole, K.A., 2001. “Full-coverage film cooling with short normal injection holes.” ASME J. Turbomach., 123(4), pp.798-805.

- [3.9] Ligrani, P., Goodro, M., Fox, M. and Moon, H.K., 2012. "Full-coverage film cooling: film effectiveness and heat transfer coefficients for dense and sparse hole arrays at different blowing ratios." *ASME Journal of turbomachinery*, 134(6).
- [3.10] Facchini, B., Maiuolo, F., Tarchi, L. and Coutandin, D., 2010, October. "Combined effect of slot injection, effusion array and dilution hole on the heat transfer coefficient of a real combustor liner: Part 1—Experimental analysis." In *Turbo Expo: Power for Land, Sea, and Air* (Vol. 43994, pp. 753-762).
- [3.11] Scrittore, J.J., Thole, K.A. and Burd, S.W., 2005, January. "Experimental characterization of film-cooling effectiveness near combustor dilution holes." In *Turbo Expo: Power for Land, Sea, and Air* (Vol. 47268, pp. 1339-1347).
- [3.12] Sasaki, M., Takahara, K., Kumagai, T., and Hamano, M. (January 1, 1979). "Film Cooling Effectiveness for Injection from Multirow Holes." *ASME. J. Eng. Power*. January 1979; 101(1): 101–108
- [3.13] Leger, B., Miron, P. and Emidio, J.M., 2003. "Geometric and aero-thermal influences on multiholed plate temperature: application on combustor wall." *International Journal of Heat and Mass Transfer*, 46(7), pp.1215-1222.
- [3.14] Rogers, N., Ren, Z., Buzzard, W., Sweeney, B., Tinker, N., Ligrani, P., Hollingsworth, K., Liberatore, F., Patel, R. and Moon, H.K., 2016, June. "Effects of Double Wall Cooling Configuration and Conditions on Performance of Full Coverage Effusion Cooling." In *Turbo Expo: Power for Land, Sea, and Air* (Vol. 49781, p. V05AT13A005). American Society of Mechanical Engineers.

- [3.15] Motheau, E., Lederlin, T., Florenciano, J.L. and Bruel, P., 2012. "LES investigation of the flow through an effusion-cooled aeronautical combustor model". *Flow, turbulence and combustion*, 88(1-2), pp.169-189.
- [3.16] Behrendt, T. and Hassa, C., 2008. "A test rig for investigations of gas turbine combustor cooling concepts under realistic operating conditions." *Proceedings of the Institution of Mechanical Engineers, Part G: Journal of Aerospace Engineering*, 222(2), pp.169-177.
- [3.17] Behrendt, T., Lengyel, T., Hassa, C. and Gerenda's, M.S., 2008, January. "Characterization of advanced combustor cooling concepts under realistic operating conditions." In *Turbo Expo: Power for Land, Sea, and Air* (Vol. 43147, pp. 1801-1814).
- [3.18] Wurm, B., Schulz, A. and Bauer, H.J., 2009, January. "A new test facility for investigating the interaction between swirl flow and wall cooling films in combustors." In *Turbo Expo: Power for Land, Sea, and Air* (Vol. 48845, pp. 1397-1408).
- [3.19] Wurm, B., Schulz, A., Bauer, H.J. and Gerendas, M., 2014, June. "Impact of swirl flow on the penetration behaviour and cooling performance of a starter cooling film in modern lean operating combustion chambers." In *ASME Turbo Expo 2014: Turbine Technical Conference and Exposition* (pp. V05CT18A007-V05CT18A007). American Society of Mechanical Engineers.
- [3.20] Andrei, L., Andreini, A., Bianchini, C., Caciolli, G., Facchini, B., Mazzei, L., Picchi, A. and Turrini, F., 2014. "Effusion cooling plates for combustor liners: experimental and numerical investigations on the effect of density ratio." *Energy Procedia*, 45, pp.1402-1411.

- [3.21] Kakade, V.U., Thorpe, S.J. and Gerendás, M., 2012, June. “Effusion-cooling performance at gas turbine combustor representative flow conditions.” In Turbo Expo: Power for Land, Sea, and Air (Vol. 44700, pp. 857-869). American Society of Mechanical Engineers.
- [3.22] Ge, B., Ji, Y., Chi, Z. and Zang, S., 2017. Effusion cooling characteristics of a model combustor liner at non-reacting/reacting flow conditions. *Applied Thermal Engineering*, 113, pp.902-911.
- [3.23] Ji, Y., Ge, B., Chi, Z. and Zang, S., 2018. “Overall cooling effectiveness of effusion cooled annular combustor liner at reacting flow conditions.” *Applied Thermal Engineering*, 130, pp.877-888.
- [3.24] Hermann, J., Greifenstein, M., Boehm, B. and Dreizler, A., 2019. Experimental investigation of global combustion characteristics in an effusion cooled single sector model gas turbine combustor. *Flow, Turbulence and Combustion*, 102(4), pp.1025-1052.
- [3.25] Greifenstein, M., Hermann, J., Boehm, B. and Dreizler, A., 2019. Flame–cooling air interaction in an effusion-cooled model gas turbine combustor at elevated pressure. *Experiments in Fluids*, 60(1), pp.1-13.
- [3.26] Rivera, J.E., Gordon, R.L., Brouzet, D. and Talei, M., 2019. Exhaust CO emissions of a laminar premixed propane–air flame interacting with cold gas jets. *Combustion and Flame*, 210, pp.374-388.
- [3.27] Gomez-Ramirez, D., Ekkad, S.V., Moon, H.K., Kim, Y. and Srinivasan, R., 2017. “Isothermal coherent structures and turbulent flow produced by a gas turbine combustor lean premixed swirl fuel nozzle.” *Experimental Thermal and Fluid Science*, 81, pp.187-201.

- [3.28] Gomez-Ramirez, David, Sandeep Kedukodi, Srinath V. Ekkad, Hee-Koo X. Moon, Yong Kim, and Ram Srinivasan. "Investigation of isothermal convective heat transfer in an optical combustor with a low-emissions swirl fuel nozzle." *Applied Thermal Engineering* 114 (2017): 65-76.
- [3.29] Park, S., Gomez-Ramirez, D., Gadiraju, S., Kedukodi, S., Ekkad, S.V., Moon, H.K., Kim, Y. and Srinivasan, R., 2018. "Flow Field and Wall Temperature Measurements for Reacting Flow in a Lean Premixed Swirl Stabilized Can Combustor". *Journal of Engineering for Gas Turbines and Power*, 140(9), p.091503.
- [3.30] Moffat, R.J., 1988. "Describing the uncertainties in experimental results." *Experimental thermal and fluid science*, 1(1), pp.3-17.

CHAPTER 4

EFFECT OF SPANWISE HOLE TO HOLE SPACING ON OVERALL COOLING EFFECTIVENESS OF EFFUSION COOLED COMBUSTOR LINERS FOR A SWIRL STABILIZED CAN COMBUSTOR

4.1. ABSTRACT

One of the most effective ways to cool the combustor liner is through effusion cooling. Effusion cooling (also known as full coverage effusion cooling) involves uniformly spaced holes distributed throughout the combustor liner wall. Effusion cooling configurations are preferred for their high effectiveness, low-pressure penalty, and ease of manufacturing. In this paper, experimental results are presented for effusion cooling configurations for a realistic swirl driven can combustor under reacting (flame) conditions. The can-combustor was equipped with an industrial engine swirler and gaseous fuel (methane), subjecting the liner walls to engine representative flow and combustion conditions. In this study, three different effusion cooling liners with spanwise spacings of $r/d = 6, 8$, and 10 and streamwise spacing of $z/d = 10$ were tested for four coolant- to-main airflow ratios. The experiments were carried out at a constant main flow Reynolds number (based on combustor diameter) of $12,500$ at a total equivalence ratio of 0.65 . Infrared Thermography (IRT) was used to measure the liner outer surface temperature, and detailed overall effectiveness values were determined under steady-state conditions. The results indicate that decreasing the spanwise hole-to-hole spacing (r/d) from 10 to 8 increased the overall cooling effectiveness by $2\text{-}5\%$. It was found that reducing the spanwise hole-to-hole spacing further to $r/d = 6$ does not affect the cooling effectiveness implying the existence of an optimum spanwise hole-to-hole spacing. Also, the minimum liner cooling effectiveness on the liner wall

was found to be downstream of the impingement location, which is not observed in existing literature for experiments done under non-reacting conditions

4.2.INTRODUCTION

With the rising fuel costs and environmental concerns, there has been a strong push towards increasing fuel efficiency and decreasing harmful emissions. At the same time, there is a constant need to increase the temperature in the combustor and turbine sections of the engines. Combustion temperatures in modern gas turbine combustors are much higher than the metal combustor liners melting temperatures. In conjunction with higher efficiency, stringent regulations governing pollutant emission have led to a shift to lean premixed combustion. In lean combustion applications, a considerable amount of air is routed into the combustion chamber through the swirler to reduce NOX emissions, reducing the amount of air available for cooling the combustor liner. Hence the development of optimized combustor liner cooling technologies is crucial to increase the life of combustor components.

A principal method used to manage the high heat loads on the combustor liners is film cooling. Film cooling refers to the injection of coolant onto a surface through holes to form an insulating layer between hot freestream air and the surface. Effusion cooling, also known as full coverage film cooling, is a standard method used to cool the combustor liner. Discrete film cooling often leads to free film cooling layer over the liner and excessive coolant flow, which causes the coolant jet to overshoot and weakens its effectiveness. Effusion cooling overcomes these issues by having successive rows of cooling holes interacting with each other and forming a continuous protective film along the wall [4.1]. Studies on full coverage film cooling and effusion cooling have been conducted since early 1950's.

One of the earliest studies to compare advanced cooling concepts of combustor liners was that of Meyers et al. [4.2]. The authors used infrared thermography to study the cooling effectiveness of different cold side and effusion cooling configurations for a flat plate. The authors reported that even though the extended surfaces on the combustor liner provided higher cooling effectiveness, the pressure drop was significantly higher as compared to the effusion cooling. A detailed review on gas turbine effusion cooling studies was carried out by Krewinkel [4.3]. Andrews et al. [4.4-4.6] investigated the effects of various factors on full-coverage film-cooling such as total number of holes, inclination angle, and length of holes. Harrington et al. [4.7] studied orthogonal effusion holes and concluded that an asymptotic fully developed adiabatic effectiveness value was established within four or eight rows. Ligrani et al. [4.8] presented effectiveness and heat transfer results for full coverage film cooling arrangements and studied the effect of the blowing ratio and the influence of dense and sparse hole arrays on effectiveness.

In recent times, there has been a shift towards testing of effusion cooling configurations under realistic swirl flow conditions. Behrendt and Hassa [4.9] studied the cooling performance of effusion-cooled liners under typical gas turbine conditions. Behrendt et al. [4.10] reported cooling effectiveness of effusion and impingement-effusion cooling configurations through steady-state IRT experiments. Wurm et al. [4.11] developed an atmospheric planar three-swirler set up to test the performance of effusion cooling liners. The rig was set up to study the effect of the actual combustor flow field and heat load on the cooling effectiveness. Wurm et al. [4.12] compared the performance of effusion-cooled liners under different operating conditions and observed that the cooling effectiveness increased with the increase in pressure drop. Andreini et al. [4.13] performed experiments to evaluate the cooling performance of flat plate effusion-cooled combustor liners. The authors carried out an effectiveness test using pressure sensitive paint (PSP) and overall

effectiveness using thermocouple-based measurements. They reported that for higher blowing ratios, the orthogonal holes performed better than the inclined holes and concluded that the hole density significantly impacted the performance of effusion liners. Kakade et al. [4.14] also conducted experiments to study the dependence of mainstream turbulence parameters on the performance of a staggered flat plate effusion-cooled liner. The authors studied the effect of blowing ratio, freestream turbulence intensity, and freestream turbulence length scale on the variation of cooling effectiveness of the cooling plates. Ge et al. [4.15] and Ji et al. [4.16] carried out experiments to compare the performance of effusion liners for an annular combustor under reacting and non-reacting conditions. The authors compared the performance of outer and inner liners of a model annular combustor at different blowing ratios and equivalence ratios. Facchini et al. [4.17] investigated a combustor geometry that includes slot-style starter films and dilution ports. Scrittore et al. [4.18] have reported detailed velocity and adiabatic effectiveness measurements for an effusion geometry in a simulated combustor environment. Some other investigations on effusion cooling can be found in Sasaki et al. [4.19], Leger et al. [4.20], Rogers et al. [4.21] and Motheau et al. [4.22].

Although many studies on combustor liner wall cooling have been carried out in the past, including realistic swirl stabilized flow fields and cooling conditions, there is still a lack of investigations under realistic reacting flow conditions with coolant-flame interactions. The present study deals with characterizing the performance of effusion cooled liner wall under realistic reacting conditions for a swirl stabilized can combustor. This paper aims to evaluate and compare the overall cooling effectiveness of effusion cooling configurations for three different spanwise hole-to-hole spacings of $r/d=10, 8$ and 6 . Steady-state IRT experiments were performed to measure the liner outer wall temperature, and detailed overall cooling effectiveness results have been

presented and discussed. The data obtained in this study aims to aid designers of gas turbine components and the development and validation of numerical codes for accurate prediction of heat transfer performance of such components.

4.3. EXPERIMENTAL SETUP

The experiments were carried out in the Thermal Energy Research and Management Laboratory (ThERMaL) at North Carolina State University. The experimental setup has been shown through a schematic in Fig. 4.1. Compressed air was drawn at 1.379 MPa and was routed through a turbine mass flow meter with pressure and temperature measurements for flow metering. The mass flow measurement uncertainty was $\sim 2.03\%$ for all cases. The air was then routed to a pressure regulator and a PID controlled flow control valve, which allowed fine control over the desired flow rate. An inline 192 kW heater was also installed in this setup, but not used in the present study.

A detailed schematic of the test section has been shown in Fig. 4.1 and Fig. 4.2. The test section consisted of a settling chamber which houses an industrial low emission swirl nozzle. The fuel nozzle includes an axial swirler, followed by fuel injectors downstream that introduce fuel into the nozzle annular channel for effective premixing. Air entered the nozzle as indicated by the arrows and passed through the swirl vanes, which imparted tangential velocity to the flow. Fuel was injected through the ports present downstream of the swirler vanes. The fuel and air mixed along the nozzle before entering the combustion chamber. The diameter of the nozzle (DN) was 70 mm. A schematic of the fuel nozzle is shown in Fig. 4.3.

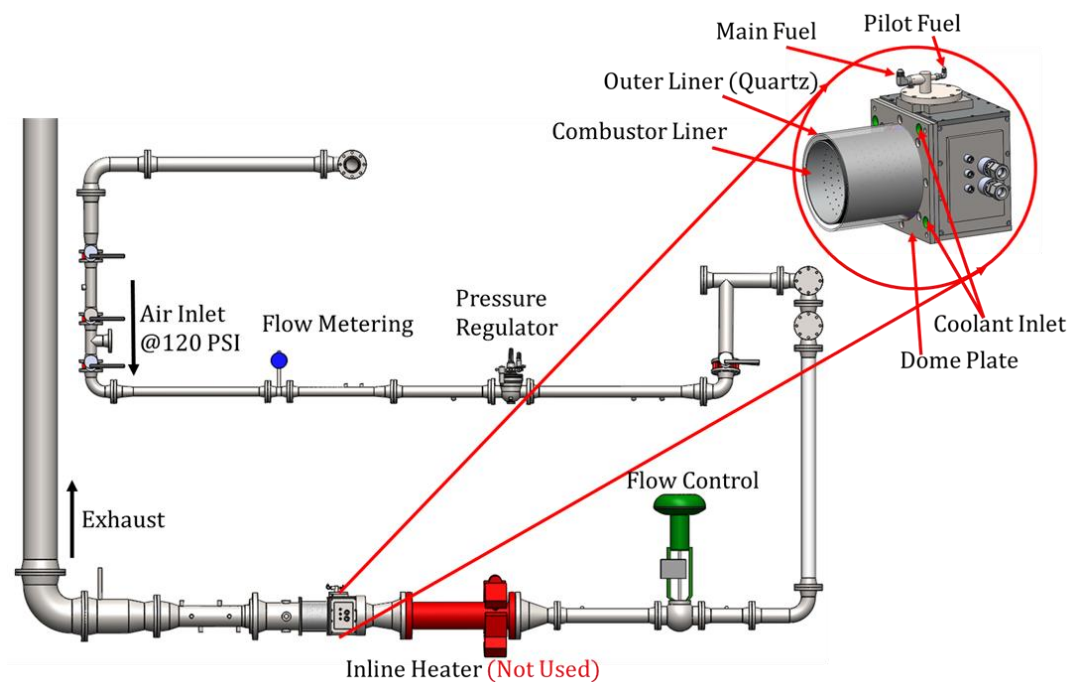


Figure 4.1 Combustor rig test setup

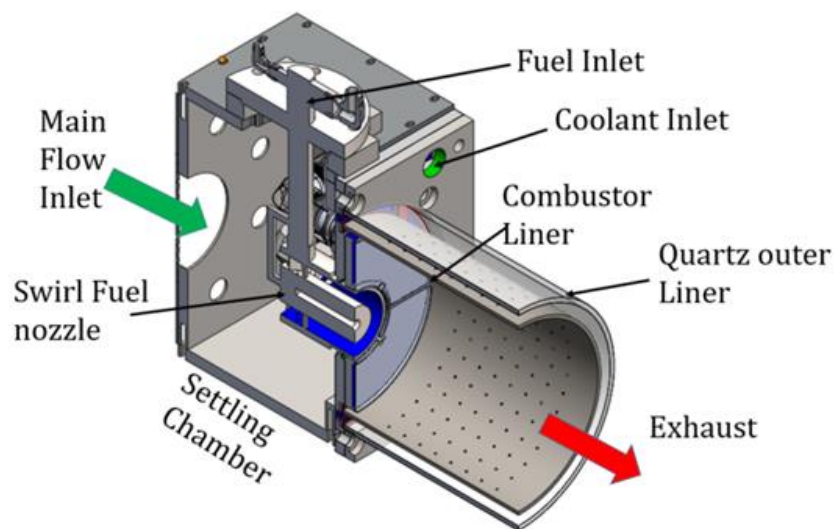


Figure 4.2 Schematic of the test section

The combustor liner was a cylindrical chamber made of stainless steel (SS316). The combustion chamber's outer diameter, length, and thickness were 209 mm, 216 mm, and 3 mm, respectively. Effusion cooling holes were machined on the combustion liner using traditional CNC machining. The combustion liner was enclosed by a transparent 4 mm thick quartz cylinder of outer diameter 235 mm. The gap between the outer quartz liner and the inner metal liner was 22 mm.

The fuel was supplied to the nozzle through inlet fuel ports in the settling chamber. The fuel inlet port consisted of separate inlets for the main fuel and pilot fuel. Alicat MCR series mass flow meters were used to meter the main and pilot fuel lines separately before entering the settling chamber.

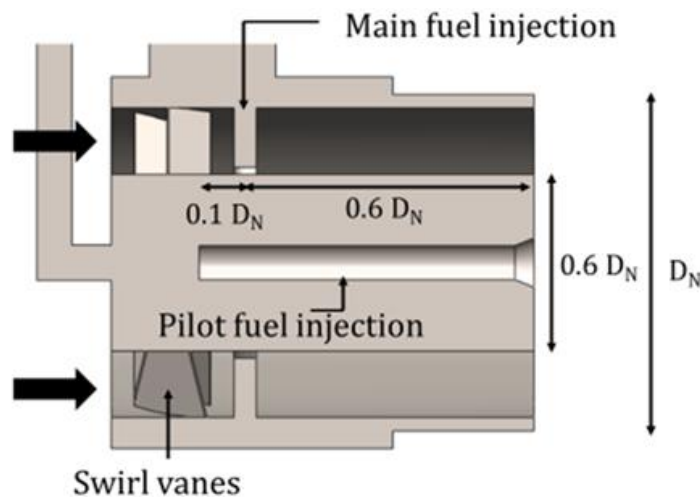


Figure 4.3 Schematic of the fuel nozzle

The settling chamber also included a plenum which fed the coolant air to the test section. The coolant plenum was designed to be isolated from the primary airflow. Four separate coolant feed lines were used to supply the coolant to the coolant plenum. Omega FMA-A2307 flowmeters

were used to meter the coolant supplied to the test section. A pressure transducer was connected to the coolant plenum to measure the pressure drop across the liner configuration. The coolant air from the plenum feed was routed through the annular space between the outer quartz liner and the combustor liner and bled into the combustion chamber via the effusion holes. The exhaust air from the test section was vented into the atmosphere through a vertical duct. The tests were performed at ambient laboratory pressures. Different operations involved in conducting the experiments and subsequent data acquisition was controlled through an in-house developed LabVIEW program.

4.3.1. Effusion Configurations

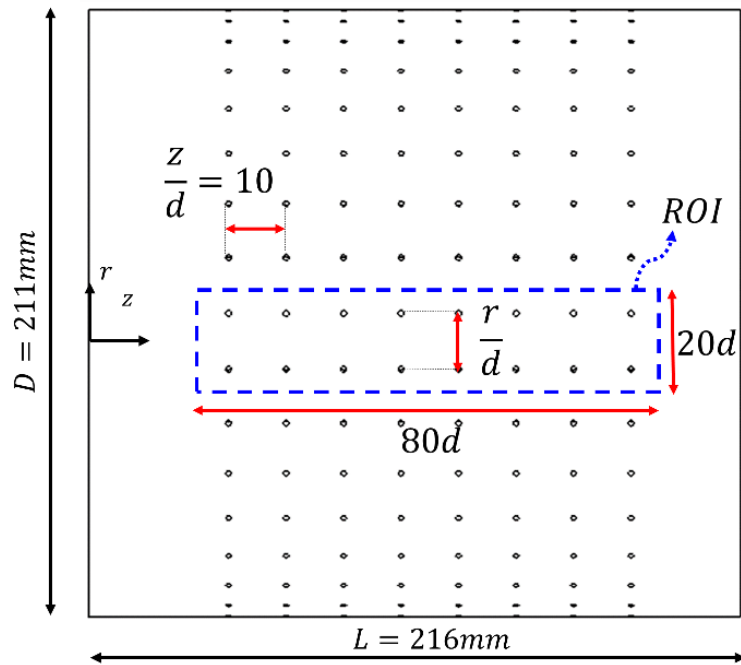


Figure 4.4 Geometric details of test section

A schematic of the effusion cooling liner is shown in Fig. 4. The effusion cooling geometries were chosen so as to investigate the effect of spanwise spacing on the overall cooling effectiveness. In this study, The diameter of each cooling hole was 2 mm. The streamwise hole-to-hole (z/d) spacing was fixed as 10. The spanwise hole-to-hole (r/d) distance was varied as 10, 8, and 6, which were all representative of actual liner configurations. A schematic of the liners investigated in this study is presented in Fig. 5. The effusion holes were orthogonal (90°) holes distributed throughout the liner in 8 streamwise longitudinal rows. Angled effusion holes will be the subject of a future study. The change in the spanwise hole-to-hole spacing changes the number of the holes and subsequently the porosity ratio.

The porosity ratio σ is defined as,

$$\sigma = \frac{4 * n * \pi * d^2}{\pi * D_{combustor} * L_{combustor}} \quad (Eq. 4.1)$$

The overall porosity ratio corresponding to the three liners is 2.3%.2.8% and 3.7%. The region of interest (ROI) for overall effectiveness contours is shown in Fig. 4.4. Since the temperature distribution for the can combustor has been shown to be axisymmetric, it was assumed that the cooling effectiveness evaluated over the ROI is representative of the entire combustor liner.

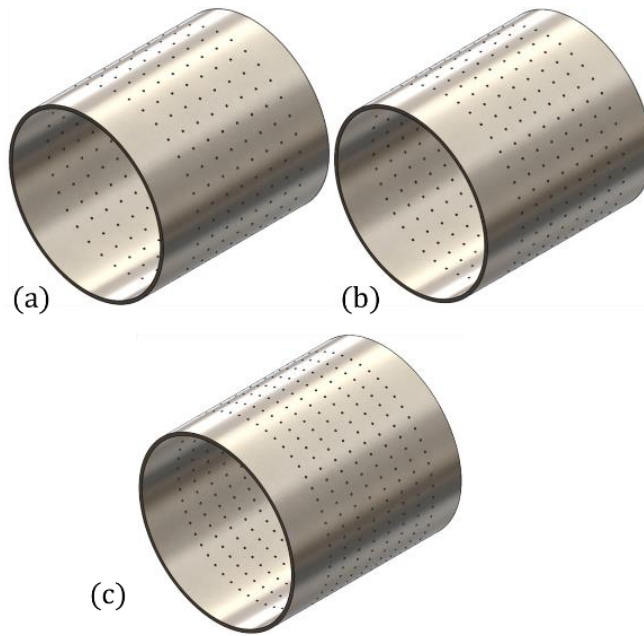


Figure 4.5 Schematic of the liners investigated in this study (a) $\frac{r}{d} = 10$ (b) $\frac{r}{d} = 8$ (c) $\frac{r}{d} =$

10

4.4. EXPERIMENTAL METHODOLOGY

The following section details the experimental methodology, operating conditions and data reduction procedure used in this study.

4.4.1. Infrared (IR) Thermography

The measurement methodology has been shown in Fig. 6. The temperature of the combustor liner's outer surface (cold side) was measured and analyzed for the results in this study. Due to the low Biot number, the temperature of the combustor liner is reasonably assumed constant throughout the thickness. [4.23].

The temperature of the combustor liner wall was measured using a FLIR A6750SC IR camera equipped with a 50 mm 1-5 μm broadband lens. A KG2 Schott glass filter was used with the IR camera lens to remove the outer quartz liner absorption and emission signal. The IR camera had a spectral response range from 1 to 5 μm , and the Schott glass filter absorbed radiation in the range 2.8 to 5 μm . Quartz glass is transparent (without absorption or emission) in the 1 to 2.8 μm range and hence was suitable for this application [4.24].

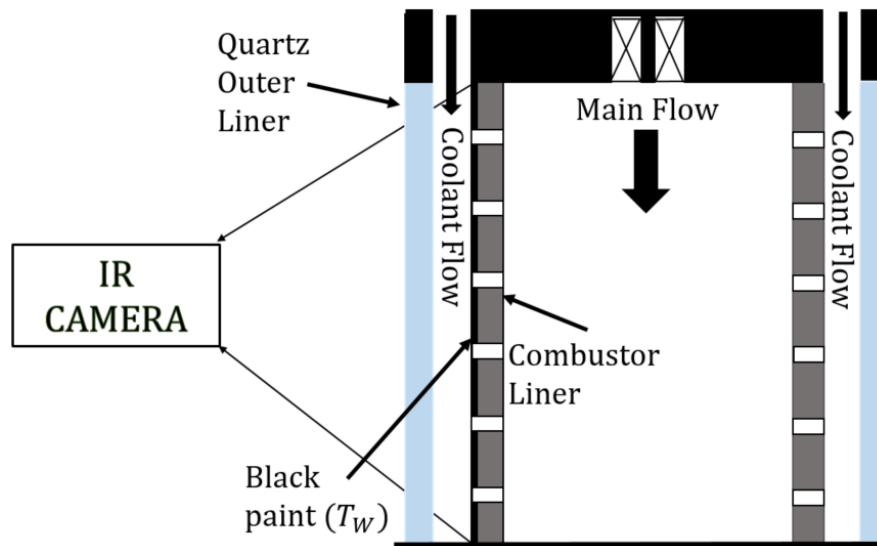


Figure 4.6 IR Methodology

However, as the quartz outer liner surrounded the combustor liner wall, the temperature signal recorded by the IR camera will not be the accurate wall temperature. A calibration process was followed to establish a relationship between the actual temperature measured by the thermocouple and the IR camera's raw output. This relationship was used to calculate the actual temperature of each pixel of the combustor liner wall as recorded by the IR camera. To reduce the

measurement error induced by reflection of the metal surface, the metal liner was painted with Rust-Oleum® black paint.

The calibration experiment was carried out using four thermocouples placed axially along the length of the metal liner. The data acquired through the thermocouple and IR camera were then synchronized. The calibration experiment was carried out to account for the entire range of temperatures that were encountered during the actual investigations. Separate calibration experiments were carried out for each combustor liner. A sample calibration curve obtained for the reacting case is presented in Fig. 7.

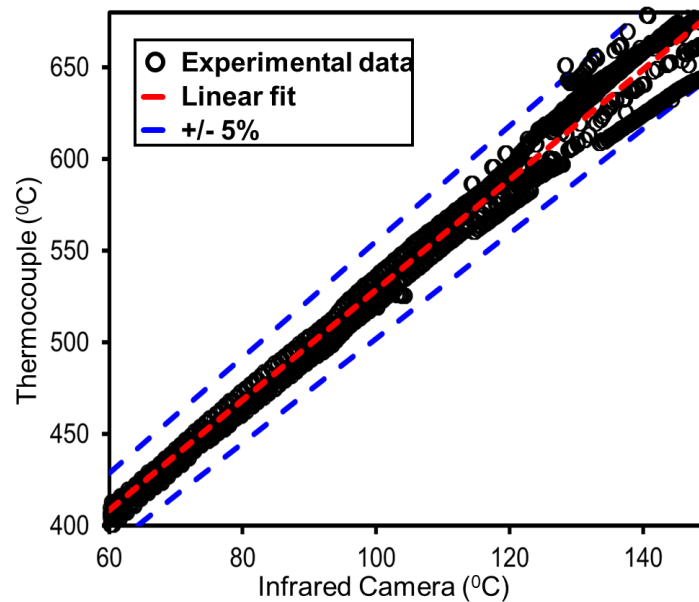


Figure 4.7 Calibration curve

All experiments presented in the study were carried out at steady-state conditions. The test section was considered to be at steady-state when the rise in temperature of the liner wall as

recorded by the IR camera for every pixel in ROI was less than 1°K over one minute for the reacting experiments.

4.4.2. Data reduction

The measured cold side wall temperature is used to calculate the overall cooling effectiveness η . Cooling effectiveness is given as,

$$\eta = \frac{(T_g - T_w)}{(T_g - T_c)} \quad (Eq. 4.2)$$

where, T_g is the gas or air temperature on the hot side of the combustor liner, T_w is the wall temperature measured by the IR camera and T_c is the coolant temperature. Due to the complexities in measuring the flame temperatures (T_g) as adiabatic flame temperature. Coolant temperature T_c was measured at the inlet of the test section using a K-type thermocouple, and the wall temperature T_w was measured using the IR camera.

4.4.3. Operating conditions

All the experiments were performed at a main air Reynolds Number (Re_c) of 12,500, where Re_c is defined as,

$$Re_c = \frac{\dot{m}_{a_{main}} D_{h_{combustor}}}{A_{combustor} \mu} \quad (Eq. 4.3)$$

To quantify the effect of the amount of coolant on the overall cooling effectiveness of the effusion liners, the commonly used parameter in literature is the nominal coolant to the main air volume rate ratio λ . This parameter is defined as

$$\lambda = \frac{\dot{m}_{a_{coolant}}}{\dot{m}_{a_{main}}} \quad (Eq. 4.4)$$

Experiments were carried out at different λ values of 5%, 10%, 15%, and 20%. The different values of λ was achieved by increasing the coolant air flow rate and maintaining the main flow rate constant. All the experiments were performed at an equivalence ratio of 0.65. The equivalence ratio was calculated based on the total air supplied to the test section, i.e., the sum of the coolant and primary air mass flow rates. In all the experiments, the pilot fuel mass flow rate was maintained at 6% of the primary fuel mass flow rate, which was representative of a can combustor, and the pilot flame was maintained throughout the experiment. The equivalence ratio calculation is shown through Eqns. 5-7.

$$\dot{m}_{air} = \dot{m}_a = \dot{m}_{a_{coolant}} + \dot{m}_{a_{main}} \quad (Eq. 4.5)$$

$$\dot{m}_{fuel} = \dot{m}_f = \dot{m}_{f_{pilot}} + \dot{m}_{f_{main}} \quad (Eq. 4.6)$$

$$\phi_{total} = \frac{AF_{stoic}}{AF} = \frac{\dot{m}_{f(actual)}}{\dot{m}_{f(stoic)}} \quad (Eq. 4.7)$$

4.5. UNCERTAINTY

The experimental uncertainty was calculated using the sequential perturbation method developed by Moffat et al. [4.25]. The thermocouples used in this setup have an inherent error of 1.1°K , the liner wall temperature has an error of $\pm 6.11\text{K}$, accounting for the calibration error. Using the sequential perturbation method, the error in overall cooling effectiveness for the experiment was found to be ± 0.041 . The main mass flow rate was calculated from the readings of a turbine flow meter upstream of the setup with simultaneous temperature and pressure measurements. The uncertainty in the mass flow measurement was $\sim 2.03\%$ for all cases.

4.6. RESULTS AND DISCUSSION

In this section, the variation of overall cooling effectiveness with the nominal coolant ratio has been presented. The adiabatic cooling effectiveness in the ROI, spanwise averaged cooling effectiveness, and globally averaged cooling effectiveness have been presented in this section.

4.6.1. Flow within the combustor

Fig. 4.8 represents a typical swirling flow in a can combustor. As shown, the incoming flow from the swirler expands, impinges, and re-attaches to the combustor liner wall.

This impingement and flow attachment leads to formation of the corner recirculation zone and central recirculation zone. The corner recirculation zone region is defined by lower heat transfer rates due to limited mixing and relatively slower flow velocities. Downstream of the impingement region, the swirling jet attached to the wall and the resulting boundary layer leads to a decrease in the heat transfer. The corner recirculation zone, central recirculation zone, and associated shear layers play an important role in stabilizing the combustion flame and significantly

affecting the heat transfer characteristics and the temperature distribution on the liner wall. Ramirez et al. [4.26] and Park et al. [4.24] have conducted detailed studies on the heat transfer and flow-field under non-reacting and reacting conditions for the current experimental setup, and the discussion presented is based on the studies performed by [4.24]. Fig. 9 shows the mean velocity of reacting flow at equivalence ratio of 0.65. The measurement was carried out in a $1.7D_N \times 1.7D_N$ plane including the fuel nozzle and the main flow impingement locations. Since the mean flow in the combustor is assumed to be axisymmetric across the center line only half of the center plane is shown in Fig. 9. The impingement region for the swirling used in this study was found to be $\frac{z}{D_N} \sim 1.16$. The authors had noticed self-similarity in reacting flows regardless of the combustor operating conditions and reported an impingement location of $1.16D_N$ with 7% deviation for a wide range of conditions tested in the study. The authors also noted that the peak temperatures occur $\sim 0.3 D_N$ downstream of the flame jet impingement location.

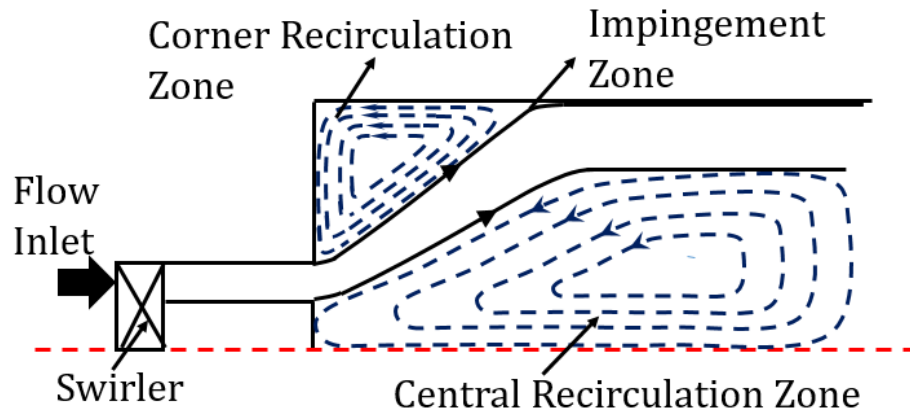


Figure 4.8 Flow features within a can combustor

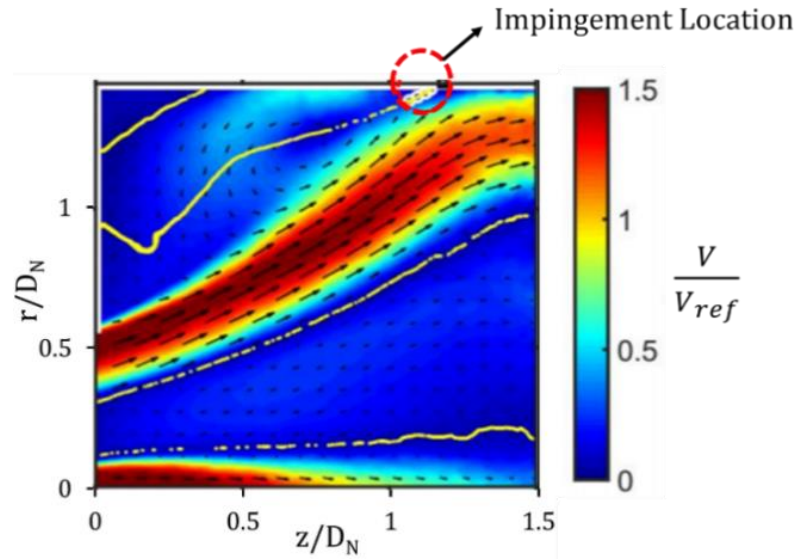


Figure 4.9 Mean velocity of reacting flow at 0.65 equivalence ratio from Park et al.

[4.23]

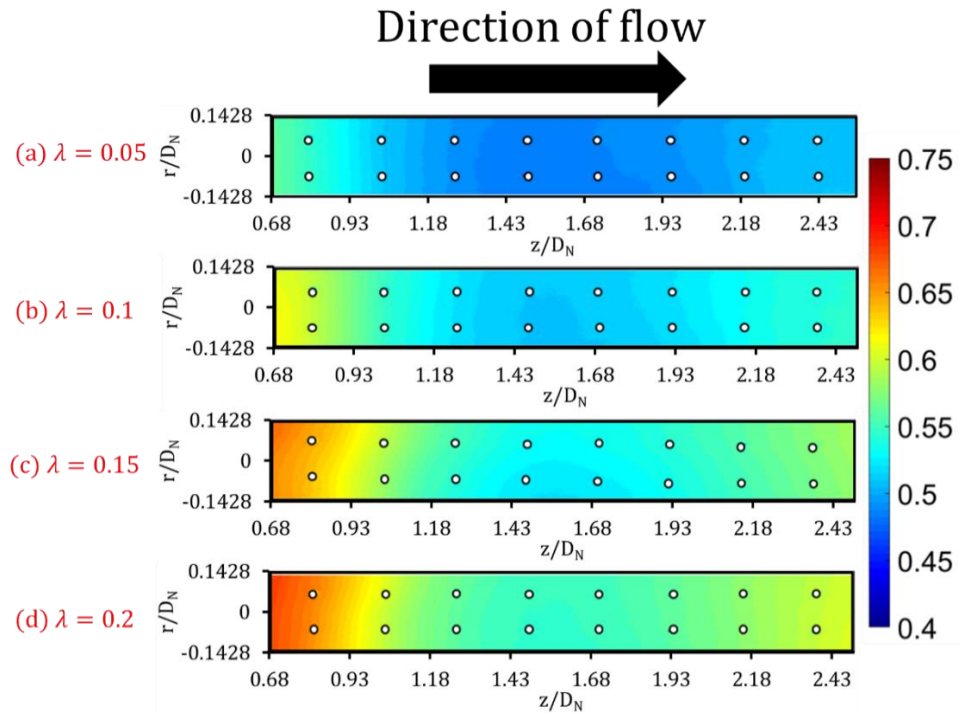


Figure 4.10 Overall Cooling Effectiveness Contour at different nominal coolant flow rates for a spanwise hole-to-hole spacing (r/d) of 10

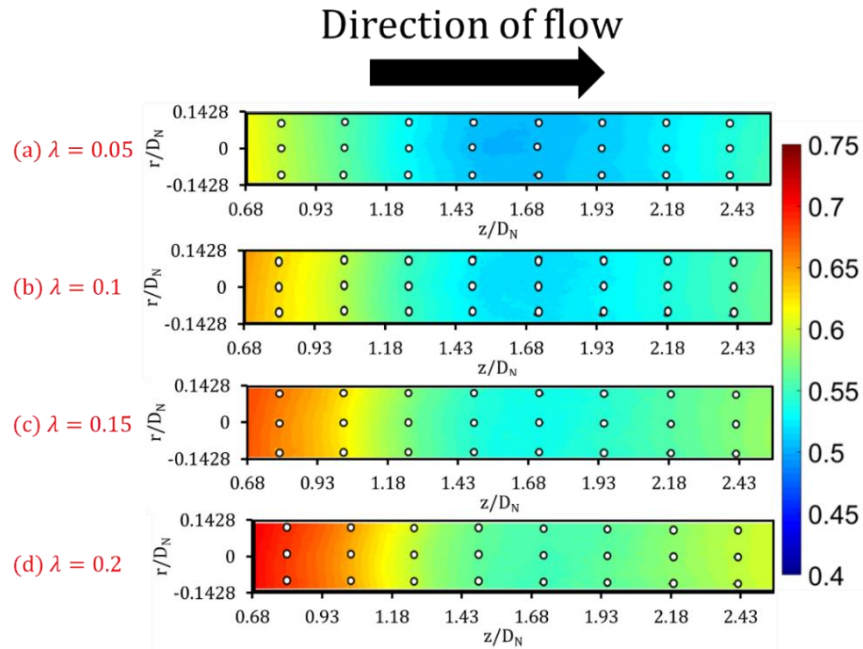


Figure 4.11 Overall Cooling Effectiveness Contour at different nominal coolant flow rates for a spanwise hole-to-hole spacing (r/d) of 8

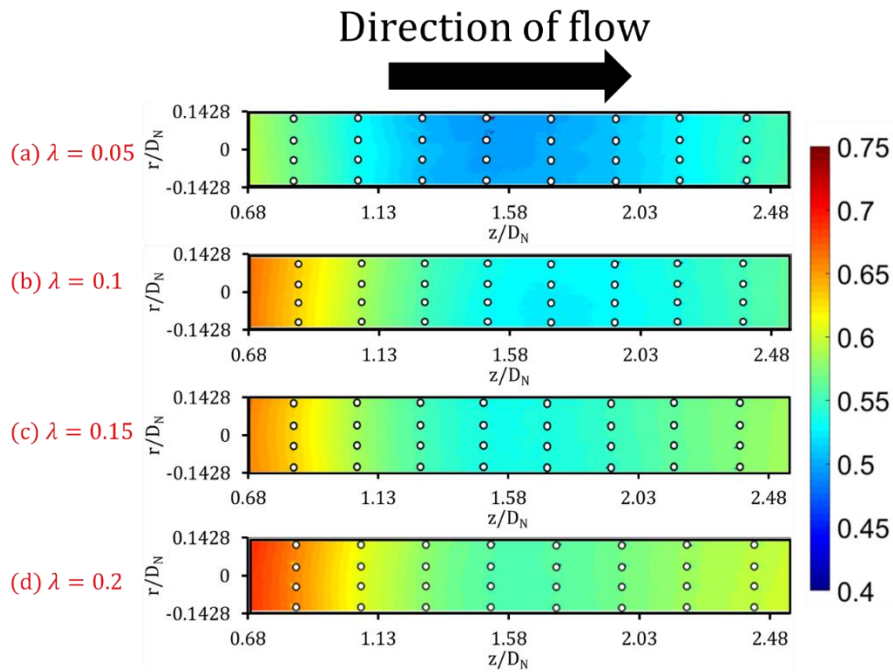


Figure 4.12 Overall Cooling Effectiveness Contour at different nominal coolant flow rates for a spanwise hole-to-hole spacing (r/d) of 6

4.6.2. Overall Cooling Effectiveness

The reacting flow experiments were carried out for a premixed methane-air flame at a total equivalence ratio of 0.65. For the experiments, due to the complex conical flame structure, calculating the local variation of the driving temperature or mainstream temperature was complex. A significant temperature gradient would exist in locations with and without the flame, and representing the combustor flow temperature by an accurate single value or a function of axial distance will not be feasible.

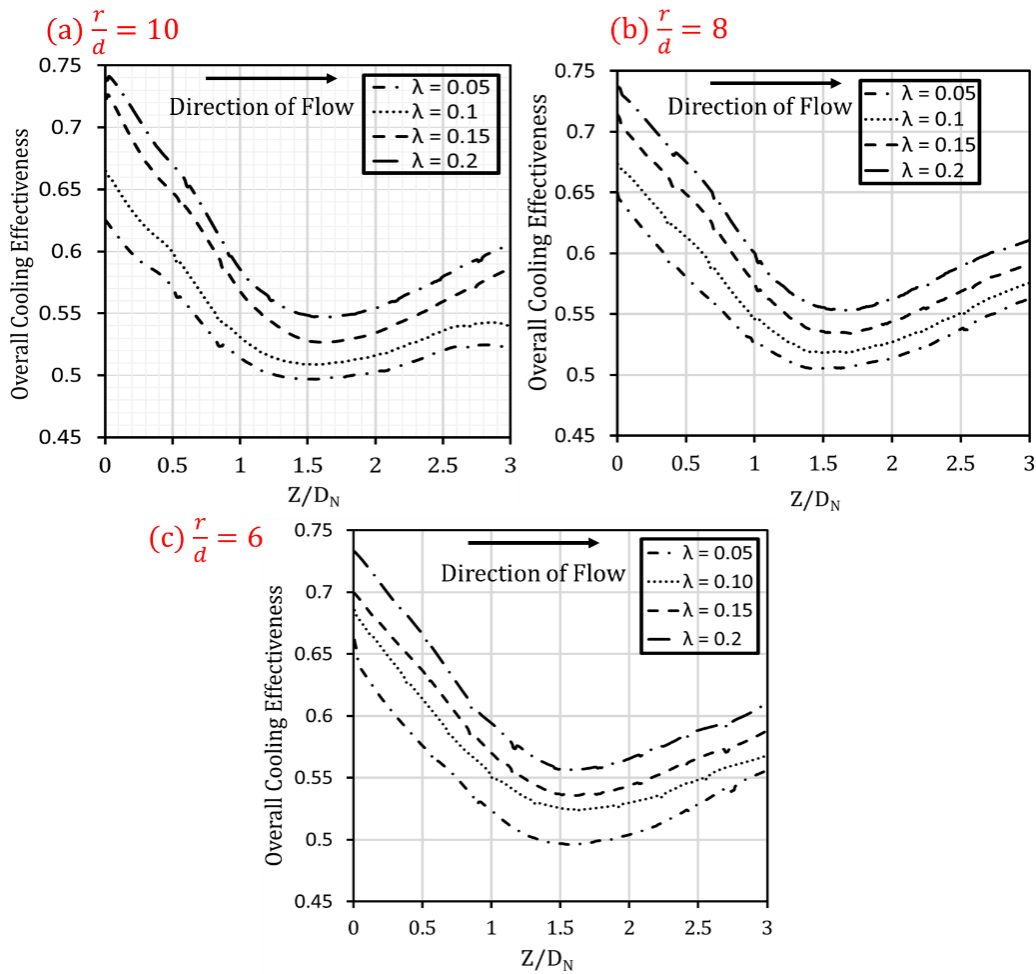


Figure 4.13 Spanwise averaged cooling effectiveness for (a) $r/d=10$ (b) $r/d=8$ (c) $r/d=10$

It was also observed that intrusive temperature measurement probes affect the flow dynamics in the combustor. For the above reasons, the results presented in the section, the mainstream temperature T_g , is approximated as the constant adiabatic flame temperature calculated at the main flow rate equivalence ratio. However, this assumption leads to a range of cooling effectiveness which is higher than in the existing literature that used temperature probes to measure the gas temperature [4.15 – 4.16].

The detailed cooling effectiveness contours for spanwise hole-to-hole spacing distances of $\frac{r}{d} = 10$, $\frac{r}{d} = 8$ and $\frac{r}{d} = 6$ with change in nominal coolant to main flow rate ratio have been presented in Fig. 4.10, 4.11, and 4.12 respectively. A similar trend was observed for the cooling effectiveness contours across the range of hole-to-hole spacings investigated in this study. Higher cooling effectiveness was observed at low values of $\frac{z}{D_N}$. In this region, the flow close to the combustor liner is dominated by the corner recirculation zone, leading to lower wall temperatures and high cooling effectiveness. The corner recirculating flow is in the opposite direction of the main flow and this leads to decreasing cooling effectiveness till $\frac{z}{D_N} \sim 1.5$. As discussed earlier, around $\frac{z}{D_N} \sim 1.16$ the flame impinges on the combustor liner wall leading to an increase in temperature along the liner wall in this region. This leads to continuously decreasing cooling effectiveness and a subsequent minimum in cooling effectiveness. The flame impingement on the liner walls also leads to the formation of a high-pressure zone in the combustor. This high pressure region reduces the amount of coolant air being injected near the impingement region, which further decreases the cooling effectiveness. This low effectiveness region, even with the presence of the effusion cooling flow, emphasizes the need for other cooling features such as slot cooling to improve the cooling effectiveness in this region and to decrease the thermal loads. Downstream

of the impingement region, the flow attaches to the linerwall and is dominated by combustion products leading to a decrease in wall temperatures and effective cooling in this region.

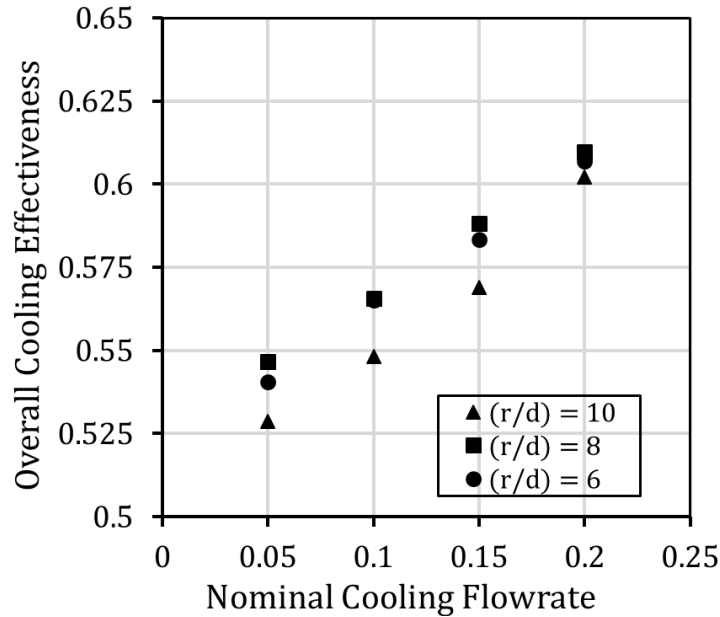


Figure 4.14 Effect of nominal cooling flowrate ratio on area averaged overall cooling effectiveness

An interesting result observed from the effectiveness contour and the spanwise averaged cooling effectiveness is that the point with the minimum cooling effectiveness ($\frac{z}{d} \sim 1.55$) does not correspond to the location of impingement $\frac{z}{d} \sim 1.16$ but is instead downstream of it. This can be attributed to the fact the flame temperature is higher in the downstream region than at the location close to the impingement region. This feature is different from experiments done under non-reacting conditions where the location of maximum heat transfer and lowest cooling effectiveness corresponds to the location of impingement on the liner wall [4.12].

The spanwise averaged cooling effectiveness for spanwise hole-to-hole distances of $\frac{r}{d} = 10$, $\frac{r}{d} = 8$ and $\frac{r}{d} = 6$ is shown in Fig. 4.13. With an increase in the nominal coolant ratio, a consistent increase in cooling effectiveness was observed across the three liners investigated in this study. This consistent increase in cooling effectiveness was observed throughout the length of the combustor liner. Existing literature [8] has shown conditions where, after a certain coolant ratio, the effectiveness of combustion liners do not increase with an increase in coolant ratio. At these conditions, the liners are said to overcooled. For the present study, this phenomenon was not noticed for the coolant ratios investigated in this study. Increasing the nominal coolant to main flow rate ratio from 5% to 20% led to increase of $\sim 9\%$ in cooling effectiveness across the three liners investigated in this study.

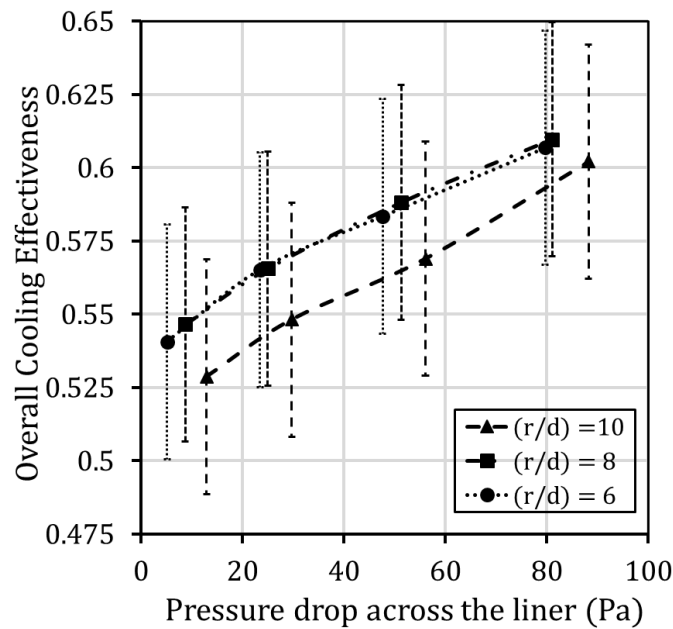


Figure 4.15 Effect of pressure drop across the liner on area averaged overall cooling effectiveness

Fig. 4.14 represents the area-averaged cooling effectiveness plotted for the three different circumferential hole-to-hole spacings at different nominal cooling flow rate ratios. The results indicate that $r/d=10$ configuration had the lowest overall cooling effectiveness. At large circumferential hole-to-hole spacings, the coolant injected through the holes are unable to interact to provide optimum protection against the hot flame driven main flow. With a decrease in the hole-to-hole spacing to $r/d=8$ the interaction between the effusion cooling holes improves and results in higher cooling effectiveness. A difference of 2-5% was observed between the $r/d=10$ and $r/d=8$ for the range of coolant ratios investigated in this study. On further decreasing the circumferential hole-to-hole spacing to $r/d=6$ no further increase in cooling effectiveness was found. This shows that an optimum spanwise hole-to-hole spacing exists for this configuration beyond which the cooling effectiveness does not increase.

To compare the performance of the effusion liners at the same pressure drop, the overall cooling effectiveness was plotted against the pressure drop across the liner at the corresponding values of λ in Fig. 4.15. The spanwise hole-to-hole spacing of $r/d=10$ had the lowest cooling performance for the same pressure drop. For $r/d=6$ and $r/d=8$ cases the curves were found to be nearly coincident with each other, which shows that decreasing the spanwise hole-to-hole spacing below $r/d=8$ does not lead to an improvement in the cooling performance of the liners. Further studies need to be carried out to study this effect in detail.

4.7. CONCLUSIONS

Steady-state infrared thermography experiments were performed to measure the liner wall temperature of a can combustor to evaluate the performance of effusion-cooled combustor liner under reacting conditions. Three different configurations of effusion liners with a varying hole-

to-hole spacing $r/d=10, 8$, and 6 were tested for four different nominal coolant to main flow rate ratios. Detailed cooling effectiveness contours, spanwise averaged cooling effectiveness, and total area-averaged cooling effectiveness values are presented.

The results showed that along the length of the combustor the cooling effectiveness first follows a decreasing trend, reaches a distinct minimum and then increases till the end of the combustor. The presence of this minimum in cooling effectiveness implies the requirement of other cooling features such as slot cooling to achieve a more uniform temperature distribution along the liner wall. A consistent increase in cooling effectiveness was observed with increase in nominal coolant flow rates. An increase of 9% in cooling effectiveness was observed across the range of nominal coolant flow rates investigated in this study.

It was observed that decreasing the spanwise hole-to-hole spacing from $r/d=10$ to $r/d=8$ increases the coolant to coolant interaction and increases the cooling effectiveness by 2-5%. Further decrease in spanwise hole-to-hole spacing was found to have no significant effect on the cooling effectiveness. This shows that the spanwise hole-to-hole spacing has an asymptotic relation with cooling effectiveness, beyond which the spanwise hole-to-hole spacing has no impact on the cooling effectiveness. Hence, it appears that an optimum hole-to-hole spacing exists at around $r/d=8$ for reacting flow conditions.

Another interesting observation has been that the location of minimum cooling effectiveness was found to be different from the swirl flow impingement location that has been found through previous experiments in uncooled combustors. This feature is unique compared to experiments done under non-reacting conditions and proves that coolant flame interaction had an effect on the cooling performance of effusion liners. This effect of reacting flow and effusion flow interaction needs to be investigated further. Another challenging issue is determining a more

accurate hot side temperature for each location to calculate local cooling effectiveness rather than using an adiabatic flame temperature approach.

NOMENCLATURE

D_N	Nozzle Diameter(m)
T	Temperature (K)
\dot{m}	Mass flow rate (kg/s)
Re	Reynolds number
r	Circumferential distance (m)
z	Axial distance (m)
AF	Air-Fuel Ratio
A	Cross section area (m^2)
ROI	Region of interest
d	Diameter of effusion hole(m)
D_h	Hydraulic diameter
n	Total number of holes
D	Diameter
L	Length

Greek symbols

ϕ	Equivalence ratio
η	Overall Cooling Effectiveness
μ	Dynamic viscosity

λ Nominal coolant to main air volume rate ratio

σ Porosity Ratio

Sub scripts

f Fuel

g Main flow

c Coolant flow

REFERENCES

- [4.1] Lefebvre, A.H., 1998. Gas turbine combustion. CRC press.
- [4.2] Myers, G., Van der Geest, J., Sanborn, J. and Davis, F., 1985, July. "Comparison of advanced cooling concepts using color thermography". In 21st Joint Propulsion Conference (p. 1289).
- [4.3] Krewinkel, R., 2013. "A review of gas turbine effusion cooling studies." International Journal of Heat and Mass Transfer, 66, pp.706-722.
- [4.4] Andrews, G.E., Khalifa, I.M., Asere, A.A. and Bazdidi-Tehrani, F., 1995, June. "Full coverage effusion film cooling with inclined holes." In Turbo Expo: Power for Land, Sea, and Air (Vol. 78811, p. V004T09A045). American Society of Mechanical Engineers.
- [4.5] Andrews, GE, Asere, AA, Gupta, ML, & Mkpadi, MC. "Full Coverage Discrete Hole Film Cooling: The Influence of Hole Size." Proceedings of the ASME 1985 International Gas Turbine Conference and Exhibit. Volume 3: Heat Transfer; Electric Power. Houston, Texas, USA. March 18–21, 1985. V003T09A003.
- [4.6] Andrews, G.E., Asere, A.A., Gupta, M.L. and Mkpadi, M.C., 1985, March. "Full coverage discrete hole film cooling: the influence of hole size." In Turbo Expo: Power for Land, Sea, and Air (Vol. 79405, p. V003T09A003). American Society of Mechanical Engineers.
- [4.7] Harrington, M.K., McWaters, M.A., Bogard, D.G., Lemmon, C.A. and Thole, K.A., 2001. "Full-coverage film cooling with short normal injection holes." ASME J. Turbomach., 123(4), pp.798-805.

- [4.8] Ligrani, P., Goodro, M., Fox, M. and Moon, H.K., 2012. "Full-coverage film cooling: film effectiveness and heat transfer coefficients for dense and sparse hole arrays at different blowing ratios." *ASME Journal of turbomachinery*, 134(6).
- [4.9] Behrendt, T. and Hassa, C., 2008. "A test rig for investigations of gas turbine combustor cooling concepts under realistic operating conditions." *Proceedings of the Institution of Mechanical Engineers, Part G: Journal of Aerospace Engineering*, 222(2), pp.169-177.
- [4.10] Behrendt, T., Lengyel, T., Hassa, C. and Gerenda's, M.S., 2008, January. "Characterization of advanced combustor cooling concepts under realistic operating conditions." In *Turbo Expo: Power for Land, Sea, and Air* (Vol. 43147, pp. 1801-1814).
- [4.11] Wurm, B., Schulz, A. and Bauer, H.J., 2009, January. "A new test facility for investigating the interaction between swirl flow and wall cooling films in combustors." In *Turbo Expo: Power for Land, Sea, and Air* (Vol. 48845, pp. 1397-1408).
- [4.12] Wurm, B., Schulz, A., Bauer, H.J. and Gerendas, M., 2014, June. "Impact of swirl flow on the penetration behaviour and cooling performance of a starter cooling film in modern lean operating combustion chambers." In *ASME Turbo Expo 2014: Turbine Technical Conference and Exposition* (pp. V05CT18A007-V05CT18A007). American Society of Mechanical Engineers.
- [4.13] Andrei, L., Andreini, A., Bianchini, C., Caciolli, G., Facchini, B., Mazzei, L., Picchi, A. and Turrini, F., 2014. "Effusion cooling plates for combustor liners: experimental and numerical investigations on the effect of density ratio." *Energy Procedia*, 45, pp.1402-1411.

- [4.14] Kakade, V.U., Thorpe, S.J. and Gerendás, M., 2012, June. "Effusion-cooling performance at gas turbine combustor representative flow conditions." In Turbo Expo: Power for Land, Sea, and Air (Vol. 44700, pp. 857-869). American Society of Mechanical Engineers.
- [4.15] Ge, B., Ji, Y., Chi, Z. and Zang, S., 2017. Effusion cooling characteristics of a model combustor liner at non-reacting/reacting flow conditions. *Applied Thermal Engineering*, 113, pp.902-911.
- [4.16] Ji, Y., Ge, B., Chi, Z. and Zang, S., 2018. "Overall cooling effectiveness of effusion cooled annular combustor liner at reacting flow conditions." *Applied Thermal Engineering*, 130, pp.877-888.
- [4.17] Facchini, B., Maiuolo, F., Tarchi, L. and Coutandin, D., 2010, October. "Combined effect of slot injection, effusion array and dilution hole on the heat transfer coefficient of a real combustor liner: Part 1—Experimental analysis." In Turbo Expo: Power for Land, Sea, and Air (Vol. 43994, pp. 753-762).
- [4.18] Scrittore, J.J., Thole, K.A. and Burd, S.W., 2005, January. "Experimental characterization of film-cooling effectiveness near combustor dilution holes." In Turbo Expo: Power for Land, Sea, and Air (Vol. 47268, pp. 1339-1347).
- [4.19] Sasaki, M., Takahara, K., Kumagai, T., and Hamano, M. (January 1, 1979). "Film Cooling Effectiveness for Injection from Multirow Holes." *ASME. J. Eng. Power*. January 1979; 101(1): 101–108
- [4.20] Leger, B., Miron, P. and Emidio, J.M., 2003. "Geometric and aero-thermal influences on multiholed plate temperature: application on combustor wall." *International Journal of Heat and Mass Transfer*, 46(7), pp.1215-1222.

- [4.21] Rogers, N., Ren, Z., Buzzard, W., Sweeney, B., Tinker, N., Ligrani, P., Hollingsworth, K., Liberatore, F., Patel, R. and Moon, H.K., 2016, June. “Effects of Double Wall Cooling Configuration and Conditions on Performance of Full Coverage Effusion Cooling”. In Turbo Expo: Power for Land, Sea, and Air (Vol. 49781, p. V05AT13A005). American Society of Mechanical Engineers.
- [4.22] Motheau, E., Lederlin, T., Florenciano, J.L. and Bruel, P., 2012. “LES investigation of the flow through an effusion-cooled aeronautical combustor model”. Flow, turbulence and combustion, 88(1-2), pp.169-189.
- [4.23] Gomez-Ramirez, D., Ekkad, S.V., Moon, H.K., Kim, Y. and Srinivasan, R., 2017. Isothermal coherent structures and turbulent flow produced by a gas turbine combustor lean pre-mixed swirl fuel nozzle. Experimental Thermal and Fluid Science, 81, pp.187-201.
- [4.24] Park, S., Gomez-Ramirez, D., Gadiraju, S., Kedukodi, S., Ekkad, S.V., Moon, H.K., Kim, Y. and Srinivasan, R., 2018. “Flow Field and Wall Temperature Measurements for Reacting Flow in a Lean Premixed Swirl Stabilized Can Combustor”. Journal of Engineering for Gas Turbines and Power, 140(9), p.091503.
- [4.25] Moffat, R.J., 1988. “Describing the uncertainties in experimental results”. Experimental thermal and fluid science, 1(1), pp.3-17.
- [4.26] Gomez-Ramirez, D., Ekkad, S.V., Moon, H.K., Kim, Y. and Srinivasan, R., 2017. “Isothermal coherent structures and turbulent flow produced by a gas turbine combustor lean premixed swirl fuel nozzle”. Experimental Thermal and Fluid Science, 81, pp.187-201.

FUTURE RECOMMENDATIONS

The overarching aim of this study was to investigate the flow and heat transfer in a swirl stabilized can combustor with particular emphasis on the development of cooling concepts. A significant motive was to study the performance of cooling configurations under reacting or flame conditions and compare the performance to experiments done under non-reacting conditions. While recognizing the limitations of analysis in this study, this motive was primarily met by studying, comparing, and quantifying the performance of effusion cooled liner under reacting and non-reacting conditions. There are still gaps in the literature that would benefit from further research and are listed below.

1. A challenging issue encountered in this study was the accurate representation of hot side gas temperature variation. Further studies need to be carried out to quantify more accurate hot side temperature for each location along the can combustor to calculate local cooling effectiveness rather than using an adiabatic flame temperature approach.
2. There is a need to study effusion cooling configuration in conjunction with other traditional cooling methods such as slot cooling and impingement cooling to enhance cooling performance and develop more favorable wall cooling effectiveness distribution.
3. Another exciting area of study can be angled effusion cooling holes. Under non-reacting conditions, angled effusion cooling holes have been shown to perform better than orthogonal effusion cooling holes. The cooling performance of angled effusion cooling holes under reacting conditions should be investigated further.
4. A challenging experimental issue encountered in the study was heat conduction effects in the test section. These effects were amplified in cases with low coolant flowrate and in

conditions where the conduction effects dominated the convection effects. A solution to completely negate the conduction effects should be investigated further.

5. Further PIV and CFD investigations should be carried out to characterize how the transient and steady-state flow interactions between the coolant flow and main flow affect the overall cooling effectiveness distributions.